Shape from Scattering:
Shape Estimation Based on Light Transport Analysis in Translucent Objects

January 2015

Chika INOSHITA

Shape from Scattering:
Shape Estimation Based on Light Transport Analysis in Translucent Objects

Submitted to
Graduate School of Information Science and Technology
Osaka University

January 2015

Chika INOSHITA

Abstract

The acquisition of object shapes has various industrial applications, such as the visual inspection of industrial products, reverse engineering of free-form products, and modeling of object shapes in computer graphics. A variety of measurement methods have been proposed to obtain object shapes with high accuracy for any material. However, it remains difficult to measure the shape of translucent objects reliably because scattering and transmitted light in the media degrades the observation. To solve this problem, we propose *shape from scattering* to estimate the shapes of translucent objects from the observed scattering itself.

We aim to model the relationship between the object shape and scattering in a simple model. While the actual scattering effect is a complicated phenomenon, scattering can be approximated by making assumptions of the target material. In this thesis, we first sample and analyze light transport in a real scene to select an appropriate scattering model for shape estimation. Light transport is described by an eight-dimensional BSSRDF that completely represents light transports with the directions and positions of incident and outgoing light. Although it is difficult to sample an eight-dimensional BSSRDF because illuminations and observations are required from every direction, we sample the high-dimensional BSSRDF using a polyhedral mirror system to place multiple virtual cameras and projectors. We also analyze the sampled BSSRDF by the visualization of low-dimensional sliced data and decompose the sampled BSSRDF into basic directional components. From the analysis of the BSSRDF, we summarize empirical characteristics of light scattering inside a real translucent medium.

From the analysis of the BSSRDF, we propose shape estimation methods for optically thin and optically thick translucent objects. Scattering in an optically thin translucent object is characterized by light attenuation along the refracted light. Refracted light is relatively easily modeled because it corresponds to single scattering, which is a one-bounce collision of light with a particle in a medium. Hence, we can determine the shape of an object from the observed intensity of single scattering and its attenuation, and develop a solution method that simultaneously determines scattering parameters and the shape according to energy minimization. Scattering in an optically thick translucent object distributes around the incident point and

loses its directionality. Such distributed scattering can be approximated as convolution with a blurring kernel. We extend this observation in our experimental setting, and obtain the shape of a target object without the effect of scattering using deconvolution. We demonstrate the effectiveness of our proposed approach in extensive experiments using synthetic and real data.

Scattering has been regarded as a nuisance and eliminated employing various approaches in the field of computer vision. In contrast, our *shape from scattering* framework is a novel shape estimation framework that uses the scattering effect as a cue for the object shape.

List of Publications

A. Awards

1. MIRU フロンティア賞, 第 16 回 画像の認識・理解シンポジウム (MIRU2013), 2013 年 8 月 1 日.
2. 卒業論文セッション最優秀賞, 情報処理学会 CVIM 研究会, 2010 年 5 月 28 日.

B. Journal Papers

1. **Chika Inoshita**, Seiichi Tagawa, Md. Abdul Mannan, Yasuhiro Mukaigawa, Yasushi Yagi, “Full-dimensional Sampling and Analysis of BSSRDF”, IPSJ Transactions on Computer Vision and Applications, Vol. 5, pp.119-123, 2013.
2. **井下 智加**, 向川 康博, 松下 康之, 八木 康史, “単一散乱の減衰に基づく半透明物体の形状推定”, 電子情報通信学会論文誌 D, Vol. J95-D, No. 8, pp.1598-1608, 2012.
3. **Chika Inoshita**, Yasuhiro Mukaigawa, Yasushi Yagi, “Ringing Detector for Deblurring based on Frequency Analysis of PSF”, IPSJ Transactions on Computer Vision and Applications, Vol. 3, pp.236-247, 2011.

C. International Conference (Full paper reviewed)

1. **Chika Inoshita**, Yasuhiro Mukaigawa, Yasuyuki Matsushita, Yasushi Yagi, “Surface Normal Deconvolution: Photometric Stereo for Optically Thick Translucent Objects”, The 13th European Conference on Computer Vision (ECCV2014), Proceedings Part II, pp 346-359, Sep. 2014.

2. **Chika Inoshita**, Yasuhiro Mukaigawa, Yasuyuki Matsushita, Yasushi Yagi, “Shape from Single Scattering for Translucent Objects”, 12th European Conference on Computer Vision (ECCV2012), Proceedings Part II, pp 371-384, Oct. 2012.

D. International workshop

1. **Chika Inoshita**, Yasuhiro Mukaigawa, Yasuyuki Matsushita, Yasushi Yagi, “Photometric Stereo for Translucent Objects using Surface Normal Deconvolution ”, The 18th SANKEN International Symposium, Total： 1 page, Dec. 2014.
2. **Chika Inoshita**, Yasuhiro Mukaigawa, Yasuyuki Matsushita, Yasushi Yagi, “Photometric Stereo for Translucent Objects by Surface Normal Deconvolution”, The 9th International Workshop on Robust Computer Vision, Total：1 page, Dec. 2014.
3. **Chika Inoshita**, Seiichi Tagawa, Md. Abdul Mannan, Yasuhiro Mukaigawa, Yasushi Yagi, “Measurement and analysis of full-dimensional BSSRDF”, The 8th International Workshop on Robust Computer Vision (IWRCV2014), Total： 1 page, Jan. 2014.
4. **Chika Inoshita**, Yasuhiro Mukaigawa, Yasuyuki Matsushita, Yasushi Yagi, “Shape Estimation Based on Attenuation of Single Scattering for Translucent Objects”, The 7th International Workshop on Robust Computer Vision (IWRCV2013), Total: 1 page, Jan., 2013.

E. Domestic Conference (Full paper reviewed)

1. **Chika Inoshita**, Seiichi Tagawa, Md. Abdul Mannan, Yasuhiro Mukaigawa, Yasushi Yagi, “Full-dimensional Sampling and Analysis of BSSRDF”，第 16 回 画像の認識・理解シンポジウム (MIRU2013)，2013 年 7 月.【MIRU フロンティア賞】
2. **井下 智加**，向川 康博，八木 康史，“単一散乱強度に基づく半透明物体の形状と散乱特性の同時推定”，第 15 回 画像の認識・理解シンポジウム (MIRU2012)，OS10-1，ページ数: 7 ページ， 2012 年 8 月.
3. **井下 智加**，向川 康博，松下 康之，八木 康史， “単一散乱からの半透明物体の形状推定”，第 14 回 画像の認識・理解シンポジウム (MIRU2011)，OS4-4，pp. 472-479，2011 年 7 月.

4. **井下 智加**，向川 康博，八木 康史，“ぶれ画像復元のためのリンギング検出器”，第 13 回 画像の認識・理解シンポジウム (MIRU2010), OS11-3, pp. 1491-1498, 2010 年 7 月.

F. Domestic Workshop

1. **井下 智加**，向川 康博，松下 康之，八木 康史，“ぼけ画像復元による半透明物体の照度差ステレオ法”，第 17 回 画像の認識・理解シンポジウム (MIRU2014), ページ数: 2 ページ，2014 年 7 月.
2. **井下 智加**，向川 康博，八木 康史，“単一散乱強度に基づく半透明物体の表面形状推定”，附置研究所間アライアンスによるナノとマクロをつなぐ物質・デバイス・システム創製戦略プロジェクト成果報告会，ページ数: 1 ページ，2012 年 4 月.
3. **井下 智加**，向川 康博，八木康史，“ぶれ画像復元のためのリンギング検出器の提案”，情処研報 CVIM, 2010-CVIM-172(7)，pp. 1-8, 2010 年. 【卒業論文セッション最優秀賞】

G. Commercial magazine

1. **井下 智加**，向川 康博，松下 康之，八木 康史，“単一散乱強度に基づく半透明物体の形状推定”，日本工業出版 画像ラボ，2013 年 5 月号.

Acknowledgements

I feel happy with spending recent six years with excellent research members. I wish to express my appreciation all experience in this laboratory. First of all, I express my heartfelt thanks to Professor Yasushi Yagi for his support and fruitful advice in my research life. He always considers the goal and applications of ongoing research in real social scenes, so that I also think the use of our research to solve social issues. Additionally, thanks to his network in computer vision committee, I can meet and collaborate with awesome researchers all over the world. I will keep developing my research activity from experiences in his laboratory.

Professor Yasuhiro Mukaigawa is the greatest supporter for me. I am always inspired his curious attitude to research and helped by his heartwarming advice. Even though he leaves the laboratory because of the long-term (about nine months) overseas business trip and promotion to Professor in Nara institute of science and technology, he always supports my research remotely. I learned basic skills on research from him such as how to use experimental instruments, how to confirm a hypothesis on problem setting by experiments, how to make a story of technical papers, and how to present our research to other people. I am indebted to his instruction in a graduate school life.

I also express my appreciation to my respectable collaborator Dr. Yasuyuki Matsushita. His technical advice always broadens my knowledgement and updates approach of my research. Without his technical support, our research paper would not be accepted to the top-level international conference. He also supported me to visit his institute for the abroad internship program. Research activity in Microsoft Research Asia is the valuable experience for me.

I wish to thank other prominent researchers Associate Professor Yasushi Makihara and Assistant Professor Ikuhisa Mitsugami for their fruitful suggestions to my research activity.

I wish to express my appreciation to Professor Toshimitu Masuzawa and Professor Haruo Takemura for being on my dissertation committee. Their instruction and critical comments help me to improve the quality of my dissertation.

Secretaries, Ms. Noriko Yasui, Ms. Masako Kamura, Ms. Makiko Fujimoto, Ms. Masako Sugimoto, and Ms. Kumiko Nakagawa greatly support me in accounting tasks such as the

procedures for a business trip and purchasing experimental instruments. I can concentrate on my research activity with their work. Here, I show appreciation for their help.

With the members of the research group on photometric analysis, Dr. Seiichi Tagawa, Yoko Baba, Tsuyoshi Takatani, Ken'ichiro Tanaka, Dr. Md. Abdul Mannan, Ryo Matsumoto, Takahiro Matsumura and Sho Ikemoto, I have spent valuable time to advance my research. I have had the support and encouragement from them.

I also thank all my co-workers and colleagues, especially, Dr. Haruyuki Iwama, Mayu Okumura, Kazuhiro Sakashita, Naoki Akae, Shosei Moriguchi, Kohei Shiraga, Ryo Kawai, Hozuma Nakajima, Takuya Ogawa, Tsukasa Okada, and the other members who I met in the Yagi laboratory. I have enjoyed laboratory life with their friendly daily conversation and technical discussion.

Finally, this research was supported by Grant-in-Aid for JSPS Fellows under the contract of 25·6215.

Contents

Chapter 1

Introduction

1.1 Background

Recent advances in sensing technologies let us measure an object shape easily [1]. Shape measurement techniques are used in various situations such as visual inspection for controlling the surface quality of industrial products, reverse engineering of free-form products, digital archiving of world heritage, obtaining object models for computer graphics, and scanning human bodies for the virtual fitting of clothes [2, 3]. As the acquisition of object shapes broadens the application of computer vision techniques, shape measurement methods have been advanced to record the shape of any type of material with a high degree of accuracy.

Shape measurement methods are classified into two types: active and passive methods. An active method uses the reflections of projected light, electromagnetic waves or other energy to infer the shape of the target object in triangulation; *e.g.*, sensing using a laser scanner, time-of-flight camera, and structured light. A passive method estimates the shape of objects from observed images without any energy projection; *e.g.*, methods that use multi-view stereo and silhouette volume intersection. For industrial application, active methods are often used because they can accurately measure a target shape with geometric calibration. Meanwhile, it is difficult to apply an active method to translucent objects within which propagating light scatters. As pointed out by Godin *et al*. [4], the brightest observation of light incident on a translucent object is shifted by scattering. Therefore, we often fail to obtain the shape of translucent objects because scattering degrades a direct projection on the target surface. Figure 1.1 shows an example of failure in measuring translucent objects that generate scattering using a commercial three-dimensional laser scanner, the Konica-Minolta Vivid 9i. While the scanner works well for observing human skin, it cannot accurately estimate the shape of translucent objects owing to strong scattering. Besides the object in Fig. 1.1, there are many translucent objects around

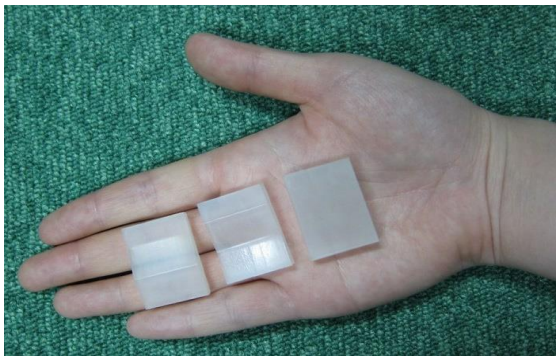

(a) Translucent blocks on the hand

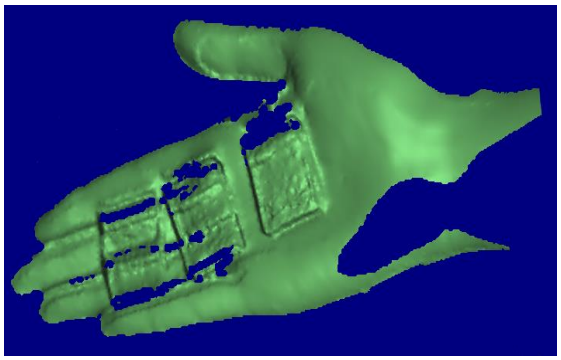

(b) Shape measurement result by a laser range finder

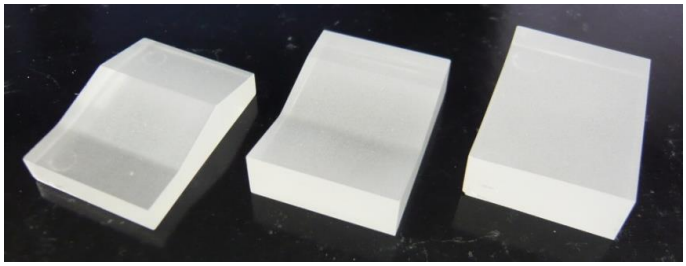

(c) Close up of translucent blocks

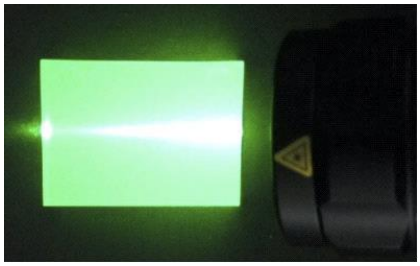

(d) Strong scattering in translucent object

Figure 1.1: Failure of the shape measurement of translucent objects using a laser scanner.

us such as most fruits, wax, marble, plastic products, and precious stones. Shape estimation of translucent objects remains an open problem.

While scattering is well studied in the computer graphics field to render realistic images, it is less discussed in the field of computer vision because complicated light interactions on the object surface generated by scattering render inverse problems unsolvable. Scattering has thus been regarded as a nuisance and eliminated by various approaches in applications of computer vision. Polarization [5, 6, 7, 8] and coating with diffuse powder [9] reduce the subsurface scattering effect. High-frequency illumination [10, 11] separates directly illuminated light (*e.g.*, surface reflection, specularity and transmittance) and globally propagated light (*e.g.*, scattering and interreflection). Analysis of the light field [12, 13] extracts scattering components according to their spatial and angular characteristics. The phase-shift method [14, 15, 16] robustly measures the object shape with the existence of scattering. However, these methods need an additional preprocessing stage and it remains difficult to completely ignore the effect of strong scattering [17]; *e.g.*, the phase-shift method requires modulation of the projection pattern depending on the translucency of the target material [18]. Consequently, shape estimation without

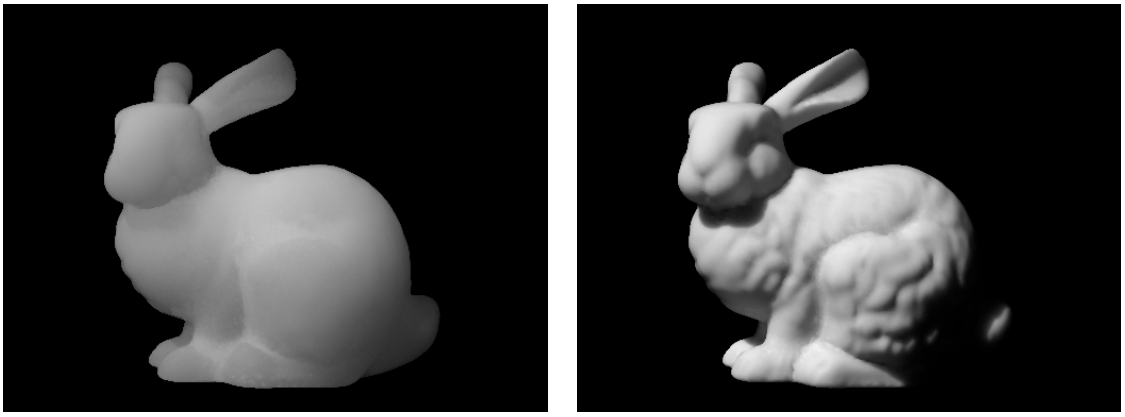

(a) Optically thin translucent object (b) Optically thick translucent object

Figure 1.2: Examples of translucent appearance. Although the shape and illumination are the same, the observed translucent appearances differ in terms of the optical thickness.

the reduction of scattering phenomena is required.

1.2 Contributions of the thesis

This thesis proposes a new shape estimation framework named the *shape from scattering* framework, where the shape of a translucent object is estimated from the observed scattering itself. While scattering is often analyzed for the estimation of the spatial distributions of smoke or milk drops [19, 20], it has not been analyzed for the measurement of the surface shape of translucent objects. Shape estimation from an observed image is considered to be the inverse rendering of a realistic scene appearance in the field of computer graphics. As a realistic image is rendered with known object shapes, illumination, and light transport on the object surface, the object shape is inversely estimated from observed images with known illumination and light transport. Illumination can be obtained from the calibration or controls of the experimental setting. However, it is not easy to obtain arbitrary light transport within a measurement target owing to intricate representations of light transport. Light transport only depends on the optical properties of measurement targets. Figure 1.2 shows that the scene appearances of translucent objects that differ only in optical thickness. While shading in Fig. 1.2 (a) is greatly smoothed, that in (b) is only slightly smoothed. To deal with the difference in light transport, we need to choose or obtain an optimal observation model of material for shape estimation.

We develop a shape measurement method for translucent objects in the following steps.

1. **Measurement and analysis of light transport on a translucent surface:** In terms of analysis of light transport at a surface point, surface reflection has been well studied

in both the fields of computer graphics and computer vision. A variety of models that approximate the reflection by a parametric function have been proposed [21, 22], and dense sampling of the reflection is possible using optical devices [23, 24]. However, in the case of scattering, standard parametric models and sampling methods are restricted to homogeneous media [25] or isotropic scattering [26] because scattering itself is a complicated phenomenon. In this part, we present a novel sampling and analysis method for complicated general light transport in a real scene. To observe light transport on a surface, we need to place many cameras and projectors around the target object. Instead of constructing such an impractical observation setting, we sample the light transport using spherically distributed virtual cameras and projectors using a polyhedral mirror system. We also analyze the sampled light transport to show the relationship between the light transport and optical properties of translucent media. In analysis, we visualize light transport in spherical distributions along outgoing directions. Additionally, we propose a method of decomposing light transport into isotropic and anisotropic components for scattering analysis.

2. **Development of a shape estimation algorithm based on an appropriate scattering model:** The framework of shape estimation using the observed intensity is referred to as the shape-from-intensity framework. Except for scattering, many types of light transport have been used for shape estimation; *e.g.*, diffuse reflection [27, 28, 29], specular reflection [30, 31, 32, 33, 34], and refracted transmission [35]. These methods model the relationship between observed intensities and the object shape to inversely estimate the object shape according to light transport on a surface. Taking the same approach, we develop appropriate observation models for a translucent object based on the result of light transport analysis. In this thesis, we propose two estimation methods, one for optically thin objects and the other for optically thick translucent objects, because the appropriate observation models of scattering are completely different for these different types of objects.

1.3 Organization of thesis

The thesis is organized as follows. Chapter 2 presents related work to show the contribution of our research. We present research on the measurement and analysis of light transport in scattering media and shape measurement for various models of light transport. Chapter 3 summarizes

the basic theory of light transport. We explain typical modes of light transport focusing on scattering effects and how to represent light transports in a mathematical expression. Chapters 4 to 6 describe in the main contribution of this thesis. First, we sample and analyze light transport in various materials to obtain characteristics of light transport that is determined by optical properties. From the analysis in Chapter 4, we develop the shape estimation methods for optically thin and optically thick translucent objects from observed scattered light in Chapters 5 and 6, respectively. The final chapter concludes the thesis with a discussion of the proposed method and future works.

Chapter 2

Related work

We summarize related work focusing on the measurement and analysis of light transport in scattering media and shape measurement under various light transports on object surfaces.

2.1 Measurement and analysis of light transport in scattering media

Light transport in known scattering media has been traditionally studied in the field of computer graphics to render realistic images [36, 37, 38]. More recently, the characteristics of scattering media in terms of light transport from scene appearance have been actively studied in the field of computer vision.

Although general scattering is a complex phenomenon, a single scattering event can easily be modeled because it is a simple one-bounce collision of a light with a particle in a medium. Hence, single scattering is often used to analyze scattering media. Mukaigawa *et al*. [39] estimated the optical parameters of scattering media from results for separate single scattering events and then analyzed the light transport by visualizing each bounce scattering component inspired by light transport analysis of interreflections [40]. Narasimhan *et al*. [41] also obtained scattering parameters by observing single scattering in a diluted scattering medium. Florescu *et al*. [42] applied optical tomography using observed single scattering and a radiative transfer equation and reconstructed the attenuation parameters of the three-dimensional volume. The spatial distributions of scattering media, such as smoke or milk drops, have also been studied [19, 20].

General scatterings have also been analyzed by employing approximated scattering distributions and graphics-processing-unit computing. Jensen *et al*. [26] approximated scattering as a dipole model under the assumption of an infinite homogeneous medium and then fitted

scattering parameters. Mukaigawa *et al*. [43] also estimated scattering parameters of homogeneous media by fitting the dipole model [26] in a known environment of arbitrary illumination. Gkioulekas *et al*. [44] analyzed the effects of the shape of the scattering distribution parameterized by a phase function on object appearance. In the field of medical imaging, optical tomography [45] has been developed to obtain the distribution of optical properties in body tissue from captured surface appearances. Because optical tomography estimates the properties of body tissue by simulating light propagation in media, a graphics-processing-unit is employed to reduce the computation time.

As described above, scattering has been analyzed from the measured spatial distribution. However, recent research has developed an imaging system that captures light propagation at approximately one-half of a trillion frames per second [46]. This ultrafast camera makes it possible to analyze propagating light on a temporal scale. Wu *et al*. [47] estimated the scattering parameter of scattering media employing a light attenuation model and identified the type of light interaction in a scene. Analysis of extended light transport on a temporal scale has also been proposed [48]. Despite the fact that time-scale image sequences can be used to analyze light transport in scattering media, the technique requires an expensive imaging system. We thus analyze the spatial distribution of scattering light and develop a method based on the scattering characteristics.

2.2 Shape measurement for various light transports

2.2.1 Shape-from-intensity

Shape-from-intensity is a generic framework for shape measurement based on observed intensities. While traditional shape-from-intensity estimates the object shape from diffuse reflection [27, 28, 29] or specular reflection [30, 31, 32, 33, 34], other types of light transport on an object surface are also used.

A convex shape tends to cast shadow on its surface because illumination is obstructed by an object itself. We cannot obtain photometric information on shadow areas but a shadow boundary shows the shape of obstructing object. Shafar and Kanade [49] proposed a basic constraint for a surface orientation, which casts the shadow on other surface. Yu and Chang estimated object shape in integrated information of shadow and shading in graph based representation [50]. Savarese *et al*. [51] proposed *shadow carving*, which carves three-dimensional volume based on shadow areas.

On a concave shape, the intensity of the unilluminated surface is often increased by inter-reflections; *i.e*., repeated reflection between two surfaces. Nayar *et al*. [52] iteratively estimated the shape of a concave surface by explicitly modeling the interreflection according to radiosity. Liu *et al*. [53] showed that the light transport of the interreflection itself can be used as a cue for shape estimation. Treibitz *et al*. [54] focused on the characteristics of fluorescence. The fluorescence emission is closer to ideal diffuse reflection even if the shape of the target is concave. They estimated the surface shape as the shape obtained using traditional shape from shading method to capture fluorescence.

Thin-film objects have iridescence along the view and lighting directions. Kobayashi *et al*. [55] modeled the appearance of iridescence and estimated the surface direction. In terms of physics, the light intensity attenuates inversely proportionally to the square of the distance from the light source. Liao *et al*. [56] used this inverse-square law to estimate object shape from light attenuation. Because polarization relates to a refraction on object surfaces, Huynh *et al*. [57] used multi-spectral polarization to simultaneously obtain refractive indices and an object shape.

While the method proposed in this thesis does not use light characteristics raised above to estimate shape, it is related to the described methods from the point of view of the shape-from-intensity framework.

2.2.2 Shape measurement of transparent objects

Translucent and transparent objects transmit incident light into the medium. As light is prevented from spreading in a transparent object, the path of the refracted light itself is used to estimate the shape of the transparent object.

Most existing methods use pixel correspondence between the observed appearance and known background texture to obtain the light path in transparent media. Murase [58] analyzed the optical flow of distorted images to establish correspondence between an unknown original background image and distorted appearance. Ye *et al*. [59] used Bokode [60], which enumerates a pinhole projector as background texture, to obtain a unique refracted light path. Ding *et al*. [61] captured a fluid surface using a camera array and estimated its shape according to the light path derived from pixel correspondence and camera calibration. Simultaneous estimation of a fluid surface and immersed scene depth has also been proposed [62] by combining distortion and defocus analysis.

Although background distortion is useful in obtaining refracted light in transparent media, it is difficult to know or estimate the original background from the appearance of solid objects.

Hence, other types of tractable light are used in shape estimation [63]. Kutulakos and Steger [35] performed triangulation of the transmitted light path analyzed according to specular reflection and transmission. Chari and Sturm [64] extended the method of Kutulakos and Steger [35] using photometric information. Wetzstein *et al*. [65] used a light field probe to analyze the transmitted light path. Miyazaki and Ikeuchi [66] estimated the shape of an object surface by analyzing multiple interreflections in the object employing a polarization ray-tracing method. Hullin *et al*. [67] immersed transparent objects in fluorescent fluid and obtained a surface shape from visualized scan-line illumination.

While the described methods use refracted light, Morris and Kutulakos [68] proposed scatter-trace photography focusing on a transparent object that partially reflects incident light. Trifonov *et al*.'s method [69] immerses target objects in fluid whose refractive index is the same as that of the target and applies tomography to obtain the target shape. Ma *et al*. [70] introduce the transport of intensity equation for phase imaging with coherent illumination to estimation of two and three-dimensional refractive phenomena.

Even though our target object is not transparent object, refracted light is an informative cue in shape estimation. In fact, we estimate the shapes of optically thin translucent objects using light refracted in the target objects.

2.2.3 Shape measurement under scattering effects

Scattering has been removed in shape estimation by including an additional preprocessing stage as described in Section 1.1. In contrast, underwater imaging techniques analyze target scenes in the presence of scattering. The scattering of light under water is described by simple attenuation because most light does not spread in the medium. Narasimhan *et al*. [71] modeled the appearance of an object in a scattering medium using attenuation of a light stripe pattern and estimated the target shape from the obtained reflectance of the target object. Tsiotsios *et al*. [72] modeled the backscattering of a light source in scattering media employing a photometric stereo technique. Treibitz and Schechner [73] estimated the scene depth from the backscattering falloff. However, these methods cannot be directly applied to estimate the shape of translucent objects because incident light spreads in translucent objects.

While shape estimation from scattering effects remains a challenging problem, Dong *et al*. [74] estimated the shapes of translucent objects from observed intensity that includes scattering effects under the assumption of an optically thick homogeneous medium. An exact model of scattering that traces light transport is complex. Conversely, scattering can be described by a simple model when the optical characteristics of the target material are limited to

optical thickness or spatial homogeneity. Our proposal is similar to this approach, where we model simple scattering while constraining the target material according to analysis of light transport in translucent media.

Chapter 3

Basic theory of light transport

Before beginning the main discussion, we describe the basic theory of light transport with emphasis on a translucent surface. We first present typical light phenomena on a translucent surface and then discuss the representation framework of light transport.

3.1 Light transport on a translucent surface

When a light ray incidents on a translucent surface, the light partially reflects on the surface, and partially transmits and scatters in the medium as shown in Fig. 3.1. The ratio of the surface reflection and subsurface scattering is physically determined by the Fresnel reflectance and transmittance [75]. Although distributions of reflected and scattered light are complicated, they can be simply categorized into several elementary components.

Surface reflection is categorized into two basic types: diffuse and specular reflection. Diffuse reflection is the light that reflects in all directions uniformly from a microscopically rough surface. Diffusely reflected light has the same intensity in all observation directions because light randomly reflects from locally rough surface. Ideal diffuse reflection is well known as Lambertian reflection [76]. Most computer vision techniques assume Lambertian reflection for analyzing an observed image simply. The light of ideal specular reflection reflects into the only direction of mirror reflection. In actual, ideal specular reflection does not exist in a real scene, because there is no completely smoothed or clean surfaces. Thus, the light of specular reflection reflects from smooth surface and distributes around the direction of mirror reflection. Such reflection gives an object a glossy or shiny appearance depending on the observation angle.

Subsurface scattering is also categorized into two types: single and multiple scattering. This categorization depends on the number of collisions between light and particles in the medium. While single scattering is the single collision of light with a particle in the medium, multiple scattering is the collision of light with particles more than once in the medium before being

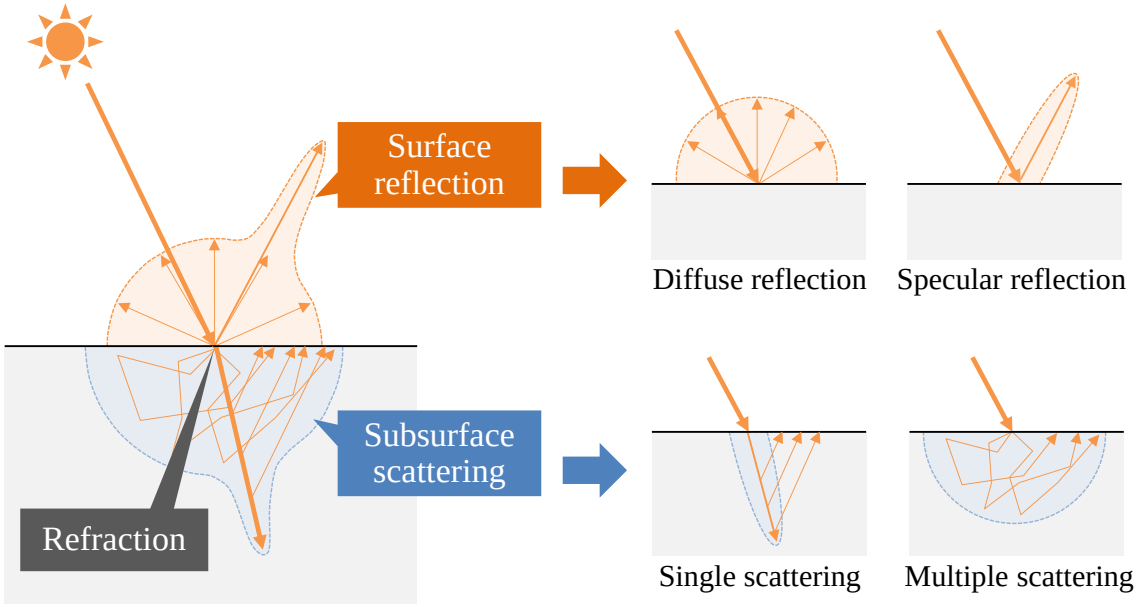

Figure 3.1: Overview of light transport on a translucent surface. Incident light not only reflects on a surface but also travels into the medium. The direction of a light ray changes on a surface because of refraction.

observed. The light path of single scattering is determined by refraction on an object surface, because the single scattering changes its traveling direction only once in the medium. The light of single scattering distributes around the refracted light in the media and exits into a refracted direction. Thus, the single scattering preserves directional distribution in the media and outgoing direction. In contrast, the light path of multiple scattering cannot be identified because repeated scattering produces an uncountable number of light paths. As a result, the light paths of multiple scattering are completely random and the light of multiple scattering randomly distributes in the media and exit into various directions. This random distribution loses directionality of the incident light and attenuates around the incident point according to the distance from the incident point and an optical characteristic.

Light transport on a translucent object is simply modeled by a combination of these reflections and scattering components. The next section introduces a representation framework for reflection and scattering models generally.

3.2 Representation of light transport

As described in Section 3.1, light transport can be characterized as outgoing distributions of light produced by varying incident light. This means that light transport can be represented by

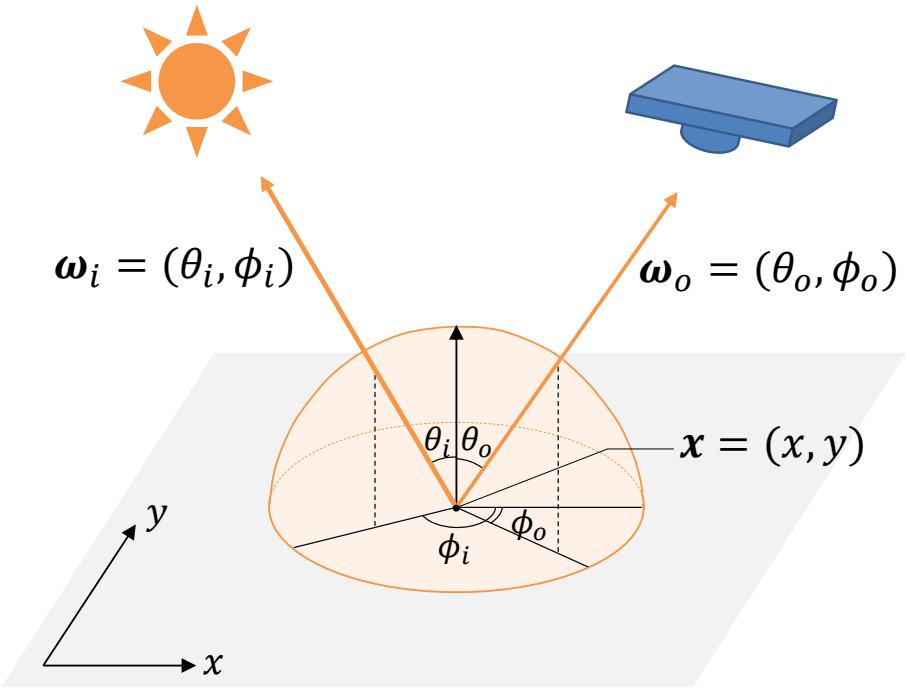

Figure 3.2: Notion of the *bidirectional reflectance distribution function* (BRDF). Incident light ray coming from the direction $\boldsymbol{\omega}_i$ is reflected into the direction $\boldsymbol{\omega}_o$ at point $\boldsymbol{x}$.

a relationship between the incident light ray and outgoing light ray. A *bidirectional reflectance distribution function* (BRDF) and a *bidirectional scattering surface reflectance distribution function* (BSSRDF) provides a framework with which to express the light transport on an object surface [77] with the incident and outgoing light ray. Figure 3.2 and 3.3 illustrate the notions of the BRDF and BSSRDF, respectively.

BRDF f_{BRDF} describes any type of reflection with a ratio of light reflected in a direction $\boldsymbol{\omega}_o = (\theta_o, \phi_o)$ to light arriving from a direction $\boldsymbol{\omega}_i = (\theta_i, \phi_i)$ at a surface point $\boldsymbol{x} = (x, y)$, and is thus denoted

$$f_{BRDF}(\boldsymbol{x}, \boldsymbol{\omega}_i, \boldsymbol{\omega}_o). \tag{3.1}$$

As four-dimensional function with fixed surface point $\boldsymbol{x}$, various BRDF models have been designed according to physical or empirical phenomena [78, 22] such as Lambertian reflection [76] for the diffuse reflection, Phong model [79] for a glossy surface, and Torrance-Sparrow model [80] for rough surface. Alternatively, some researchers made database of reflection by measuring BRDF in real scenes [81, 82, 83, 84, 85]. The obtained BRDF has also been used to analyze the characteristics of reflection in real scenes [86, 87, 88, 89]. Reflection on an optical inhomogeneous material is easily represented by suitable independent BRDFs at

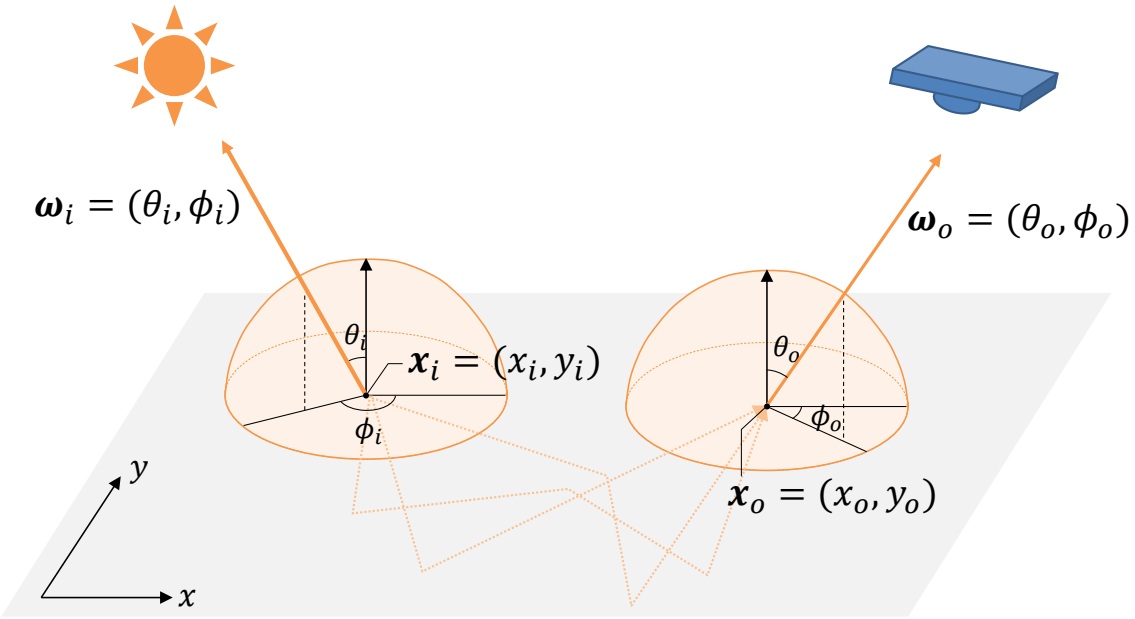

Figure 3.3: Notion of the *bidirectional scattering surface reflectance distribution function* (BSSRDF). When a light ray coming from $\boldsymbol{\omega}_i$ incidents at point $\boldsymbol{x}_i$, part of the light scatters into the subsurface. After scattering in the medium, light outputs from a different point $\boldsymbol{x}_o$ and is distributed in the direction $\boldsymbol{\omega}_o$.

each surface point $\boldsymbol{x}$. Hence, recent research has fabricated arbitrary BRDFs employing wave optics [90], a dynamic display with liquid [91], a programmable liquid-crystal spatial light modulator [92], and by controlling specular highlights on the printing surface [93].

BSSRDF f_{BSSRDF} is an extended framework of the BRDF that expresses subsurface scattering effects. The BSSRDF represents the ratio of outgoing light from point $\boldsymbol{x}_o = (x_o, y_o)$ in direction $\boldsymbol{\omega}_o = (\theta_o, \phi_o)$ to incident light at point $\boldsymbol{x}_i = (x_i, y_i)$ from direction $\boldsymbol{\omega}_i = (\theta_i, \phi_i)$, and is thus expressed

$$f_{BSSRDF}(\boldsymbol{x}_i, \boldsymbol{\omega}_i, \boldsymbol{x}_o, \boldsymbol{\omega}_o). \tag{3.2}$$

Although BRDF models and sampling methods have been well studied, there are neither standard parametric models nor sampled raw data for the eight-dimensional BSSRDF because of its high dimensionality. To sample the eight-dimensional BSSRDF, we need to control not only the direction but also the position of incident and outgoing light ray. Hence, researchers often approximate the BSSRDF as a low-dimensional function by considering only a homogeneous medium [25, 94, 95] or assuming isotropic scattering based on diffusion theory [26, 96, 97] to shrink information of absolute incident and outgoing points. To represent the spatial varying scattering effect, the BSSRDF needs absolute points of the incident and outgoing light. The

use of a full-dimensional BSSRDF to express general scattering effect remains a challenging task in light transport analysis.

Chapter 4

Measurement and Analysis of Light Transport Employing a Full-dimensional BSSRDF

From this chapter, we present the main contribution of our research. Firstly, we analyze the light transport in translucent objects to obtain an appropriate appearance model that reflects analyzed characteristics.

4.1 Introduction

Reflection, which is light transport at a surface point, has been well analyzed as a BRDF. A variety of parametric BRDF models have been proposed [78], and a raw BRDF database has been constructed [81]. Alternatively, dense sampling of the BRDF using optical devices has become possible [24, 23]. However, reflection alone is not enough to represent the translucent appearance owing to the occurrence of subsurface scattering [98].

To analyze light transport on translucent objects, we need to measure the full-dimensional BSSRDF that represents general light transport in real scenes. However, researchers have measured only low-dimensional BSSRDFs for the analysis of isotropic scattering or propagating light in optically homogeneous media [25, 94, 95]. Sampling of the full-dimensional BSSRDF is simply achieved by capturing the intensity for all possible illumination and observation directions via surrounding illumination and observation of the target medium. As this simple sampling takes an enormous time and requires large numbers of devices, we need to develop an appropriate sampling method.

In this chapter, we present a novel sampling and analysis method for the full-dimensional BSSRDF. We sample this full-dimensional BSSRDF using a polyhedral mirror system to place many virtual cameras and projectors around the target medium. We also analyze the sampled

BSSRDF by visualizing four-dimensional slices to observe the characteristics of light transport. In addition, we propose a method of decomposing the BSSRDF into isotropic and anisotropic components for scattering analysis. This research is the first attempt to sample and analyze a full eight-dimensional BSSRDF for both homogeneous and inhomogeneous translucent materials such as rubber and marble. Because the sampled full-dimensional BSSRDF permits the analysis of the scattering distribution in both spatial and angular domains, we decompose the BSSRDF into isotropic and anisotropic components to analyze characteristics of the directional distribution of the BSSRDF.

4.2 Sampling the full-dimensional BSSRDF using a polyhedral mirror system

4.2.1 Polyhedral mirror system

To sample the BSSRDF, we need to surround the target object with many cameras and projectors. Obviously, such large numbers of devices are impractical. Therefore, mirror systems [99, 100] are often used to produce many virtual cameras and projectors. Figure 4.1 shows the principle of creating a virtual camera with a planar mirror. A camera observes a target object as reflections on the mirror. Each reflected image mimics an observation from the back of mirrors. While existing mirror systems [99, 100] are designed for special imaging methods such as shallow depth-of-field imaging and confocal imaging, these systems can observe target scenes from various directions with controlled illuminations. In fact, we have already developed the *Turtleback reflector* as shown in Fig. 4.2 (a) in previous research [100]. The reflector was designed to distribute many virtual cameras and projectors on a hemisphere with uniform density and constant distance. Combining the reflector with a camera and a projector, we can observe and illuminate from a wide area of a hemisphere. We reuse this system to sample the full-dimensional BSSRDF.

The sampling densities of the incident position $\boldsymbol{x}_i$ and outgoing position $\boldsymbol{x}_o$ are 20 by 20 and 100 by 100, respectively. The number of sampling directions of $\boldsymbol{\omega}_i$ and $\boldsymbol{\omega}_o$ is 48. Figure 4.3 shows the position of the virtual cameras and projectors. In total, 19,200 (48 incident directions $\times$ 20 by 20 resolution) images are captured for BSSRDF sampling. If the shutter speed is set to 100ms, the total sampling time becomes 32 minutes. Although the sampling is sparse, the full-dimensional (eight-dimensional) BSSRDF can be obtained using our optical device.

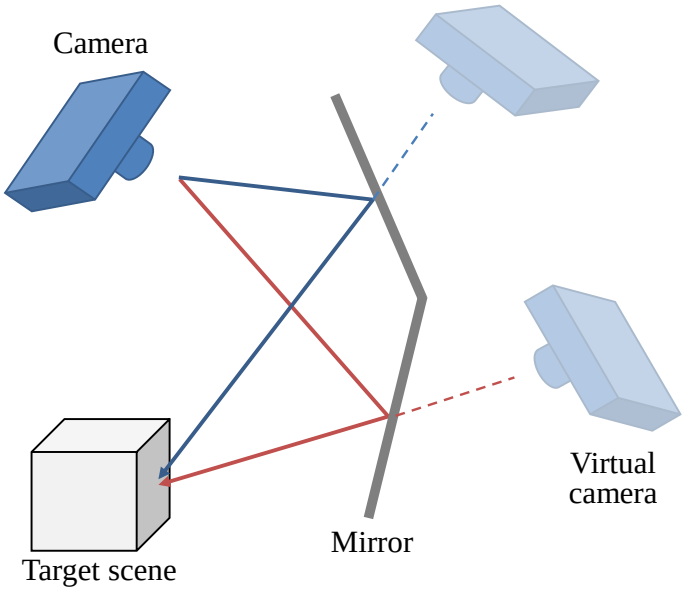

Figure 4.1: Virtual camera with mirror. A camera captures the target scene as a reflection on the mirror.

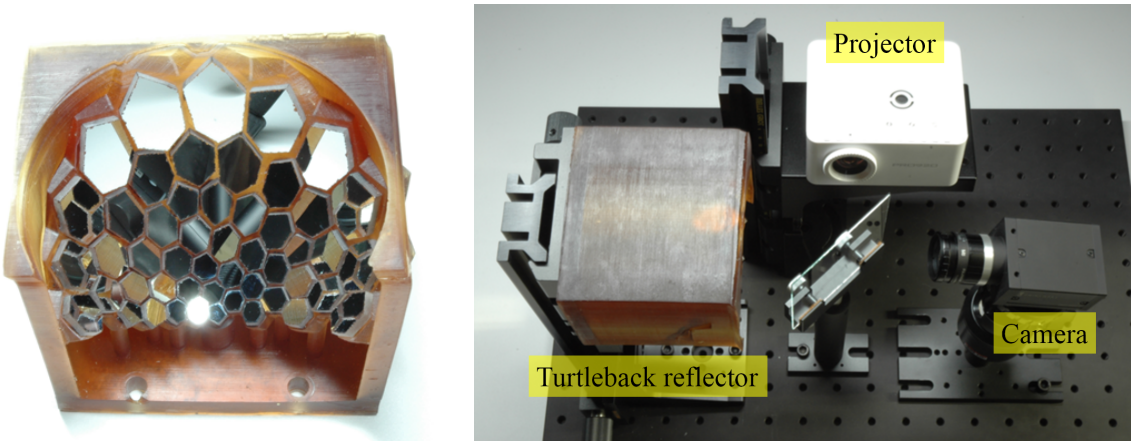

(a) *Turtleback reflector* (b) System overview

Figure 4.2: *Turtleback Reflector* [100]. The combination of the reflector with a camera and a projector. Many virtual cameras and projectors can be distributed on a hemisphere.

4.2.2 Sampled BSSRDF

We sampled BSSRDFs of three different materials, namely (a) epoxy resin, (b) rubber eraser, and (c) marble, as shown in Fig. 4.4. These materials have different properties of translucency. The epoxy resin is optically thin, while the rubber eraser is optically dense. The marble is a typical inhomogeneous material. Square regions indicated by red broken lines show the

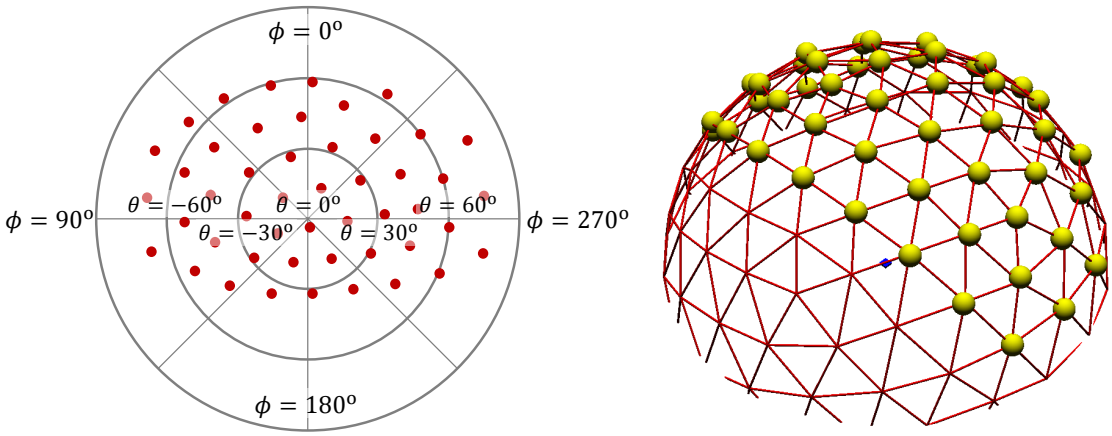

Figure 4.3: Sampling positions on a hemisphere. Left: virtual cameras and projectors are placed uniformly in a spherical coordinate system. Right: sampling positions correspond to the vertexes of the geodesic dome.

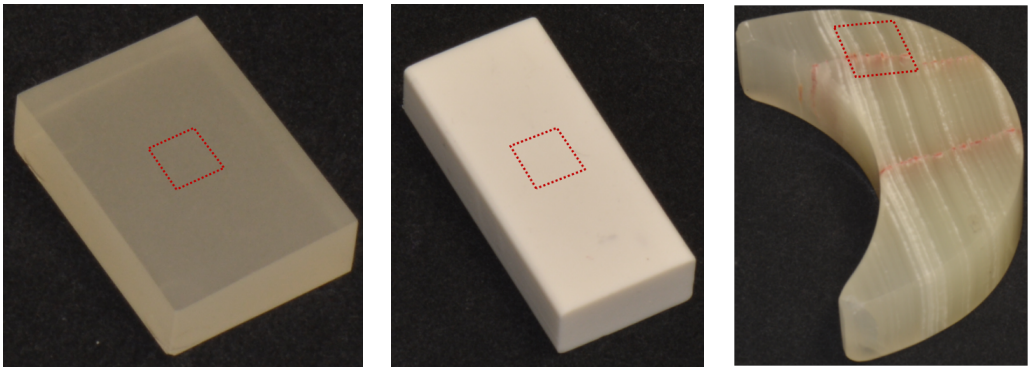

(a) epoxy resin (b) rubber eraser (c) marble

Figure 4.4: Target translucent materials. The epoxy resin is optically thin, while the rubber eraser is optically dense. The marble is a typical inhomogeneous material. Square regions indicated by red broken lines show the sampling areas.

sampling areas. Figure 4.5 shows examples of images captured by virtual cameras that are enhanced by gamma correction ($\gamma = 2.0$). The left column of Fig. 4.5 shows images captured by different virtual cameras under the same incident light. These are four-dimensional $(\boldsymbol{x}_o, \boldsymbol{\omega}_o)$ slices of the sampled BSSRDFs under fixed illumination $\boldsymbol{x}_i = (0, 0)$ and $\boldsymbol{\omega}_i = (2.2°, 154.3°)$. Each small block shows the brightness at each outgoing position $\boldsymbol{x}_o$ from a particular outgoing direction $\boldsymbol{\omega}_o$. The right column of Fig. 4.5 shows images captured by the same virtual camera under different incident lights. These are four-dimensional $(\boldsymbol{x}_o, \boldsymbol{\omega}_i)$ slices sampled from the fixed incident point $\boldsymbol{x}_i = (0, 0)$ and outgoing direction $\boldsymbol{\omega}_o = (2.2°, 154.3°)$. As there is color bleeding in the captured images owing to the color filter pattern of the projector, we analyze the

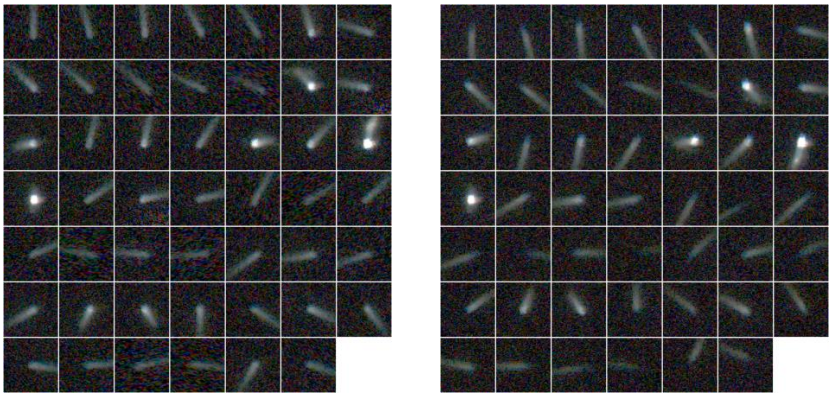

(a) epoxy resin

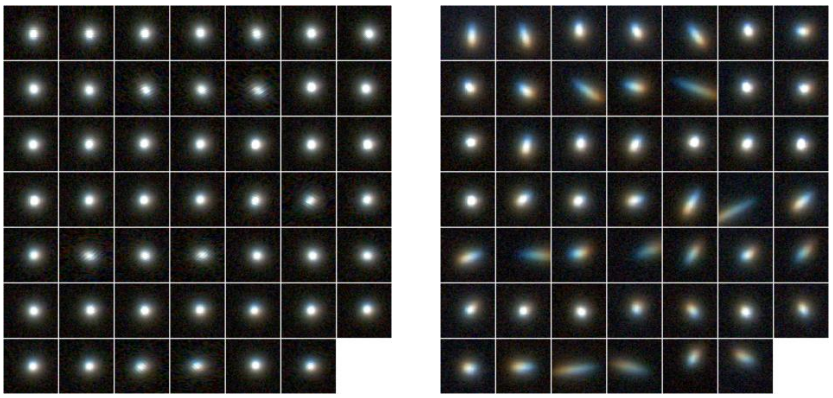

(b) rubber eraser

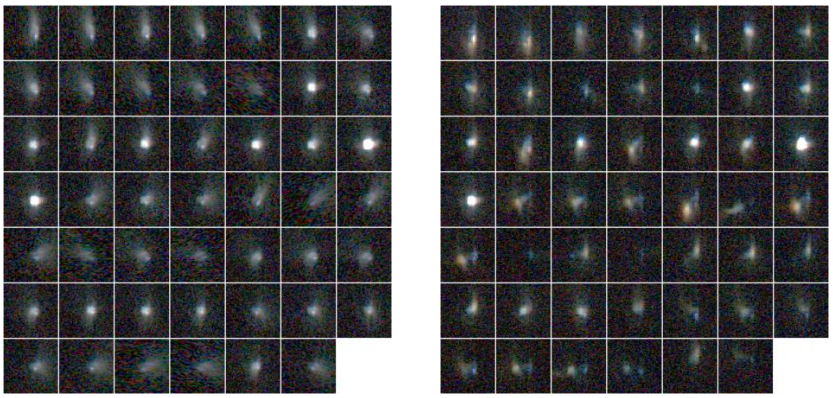

(c) marble

Figure 4.5: Examples of images captured by virtual cameras. The left column shows images captured by different virtual cameras under the same incident light. The right column shows images captured by the same virtual camera under different incident lights. These images are enhanced by gamma correction ($\gamma = 2.0$).

scattering intensities in grayscale. Figure 4.5 shows different light distributions on the epoxy resin and almost the same light distributions on the rubber eraser for both fixed illumination and observation. These distributions show that the light distribution in the epoxy resin changes with the incident and outgoing directions, while the distribution in the rubber eraser does not change with outgoing direction. The marble has spatially varying scattering because of its inhomogeneous structure, including both optically thin and dense parts. Although such simple analysis of the spatially distributed light with fixed illumination and observation directions is possible, it is difficult to observe the directionally distributed light for the outgoing direction from measurements in Fig. 4.5. In the next section, we analyze the sampled BSSRDFs in terms of both directional and spatial distributions.

4.3 Analysis of the Sampled BSSRDF

4.3.1 Visualization of the BSSRDF

Visualization is an effective method of analyzing sampled data. In the case of BRDF $f(\boldsymbol{x}, \boldsymbol{\omega}_i, \boldsymbol{\omega}_o)$, the directional distribution $f(\boldsymbol{\omega}_o)$ for several incident directions $\boldsymbol{\omega}_i$ and positions $\boldsymbol{x}$ is often visualized for reflection analysis. Here, we also analyze sampled BSSRDFs $f(\boldsymbol{x}_i, \boldsymbol{\omega}_i, \boldsymbol{x}_o, \boldsymbol{\omega}_o)$ by the visualization of the low-dimensional BSSRDF $f(\boldsymbol{x}_o, \boldsymbol{\omega}_o)$ with fixed incident light.

First, we compare the visualized low-dimensional BSSRDFs with fixed incident direction $\boldsymbol{\omega}_i$ to observe the change in the BSSRDF with incident position $\boldsymbol{x}_i$. Figure 4.6 shows illuminated positions $\boldsymbol{x}_i$ on each material. Figure 4.7 shows four-dimensional slices $f(\boldsymbol{x}_o, \boldsymbol{\omega}_o) = f(x_o, y_o, \theta_o, \phi_o)$ of the BSSRDF at a couple of incident positions $\boldsymbol{x}_i = (x_i, y_i)$ as six-dimensional slices $f(\boldsymbol{x}_i, \boldsymbol{x}_o, \boldsymbol{\omega}_o) = (x_i, y_i, x_o, y_o, \theta_o, \phi_o)$ of the BSSRDF. The direction of illumination is

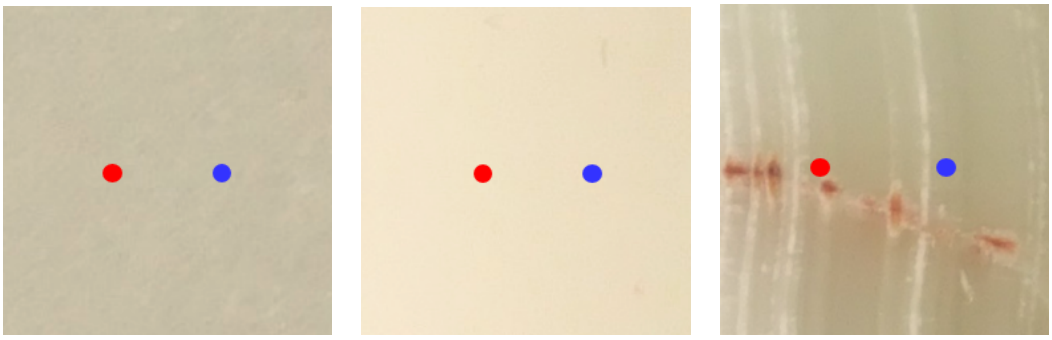

(a) epoxy resin (b) rubber eraser (c) marble

Figure 4.6: Illuminated positions for the visualization of each material

fixed at $\boldsymbol{\omega}_i = (44.9°, 74.8°)$. We plot the value of the BSSRDF at $\boldsymbol{x}_o$ from -30 to 30 in 10 intervals for all viewing directions in log-scale pseudo color on a spherical coordinate system at each outgoing position. The left and right columns in Fig. 4.7 show four-dimensional slices of the BSSRDF obtained with illumination at the red and blue points in Fig. 4.6, respectively. Figure 4.7 (a) shows slices of the BSSRDF of epoxy resin in which there is a straight light distribution. Visualized directional distributions at each position have a peak value for a specific direction and BSSRDFs have large values along the azimuth angle of the direction of illumination. This shows that scattering in epoxy resin is accounted for by single scattering because single scattering preserves the directionality of incident light. Additionally, slices of BSSRDFs are similar despite having different incident positions because epoxy resin is a homogeneous medium. Figure 4.7 (b) shows a visualized slice of the BSSRDF of rubber eraser. BSSRDF slices obtained for different incident points are also similar owing to the homogeneity. The directional distribution at each position has an almost constant value that decreases with distance from the incident point. This shows that multiple scattering loses the directionality of the incident light and is distributed uniformly among the outgoing directions. Figure 4.7 (c) shows the visualized BSSRDF of marble. Because marble is optically thin, light propagates in a particular spatial region as for epoxy resin. However, slices of BSSRDFs for different incident positions are not the same owing to the inhomogeneous structure. As eight-dimensional BSSRDF includes spatial information such as the incident and outgoing positions, we can analyze the spatial structure according to the similarity of BSSRDF slices.

Figure 4.8 shows six-dimensional slices $f(\boldsymbol{\omega}_i, \boldsymbol{x}_o, \boldsymbol{\omega}_o) = f(\theta_i, \phi_i, x_o, y_o, \theta_o, \phi_o)$ of the BSSRDF. The red distribution is obtained for the direction of illumination $(\theta_i, \phi_i) = (44.3°, 127.2°)$, and the blue distribution is obtained for $(\theta_i, \phi_i) = (43.7°, 233.7°)$. Directions of illumination are almost symmetric. Optically thin materials such as epoxy resin and marble changes the shape of the distribution according to the direction of illumination and distributions at each point are anisotropic. Light distributions of optically dense rubber eraser do not change with the incident angle. Additionally, distributions at each incident point are isotropic. For any material, angular distributions with the direction of illumination represent optical characteristics of the material.

In this section, we analyze the sampled BSSRDFs by visualization. If the BSSRDF is represented by an approximated low-dimensional function, it is difficult to analyze both spatial and angular distributions simultaneously. We carry out detailed analysis by sampling the full-dimensional BSSRDF.

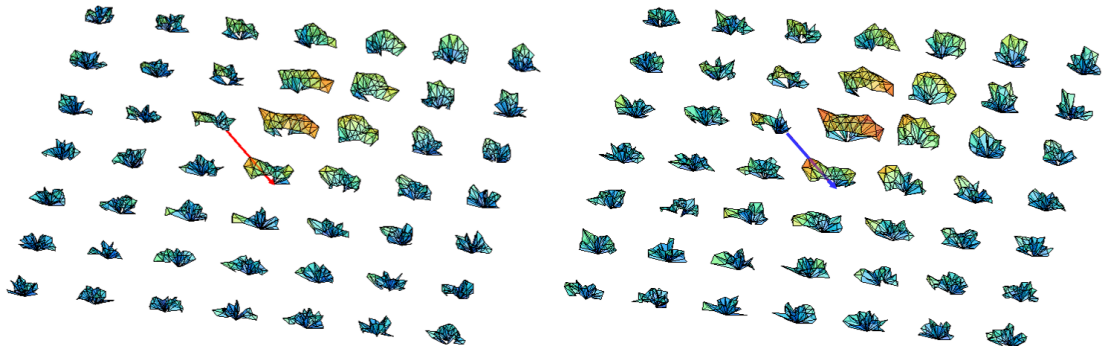

(a) epoxy resin

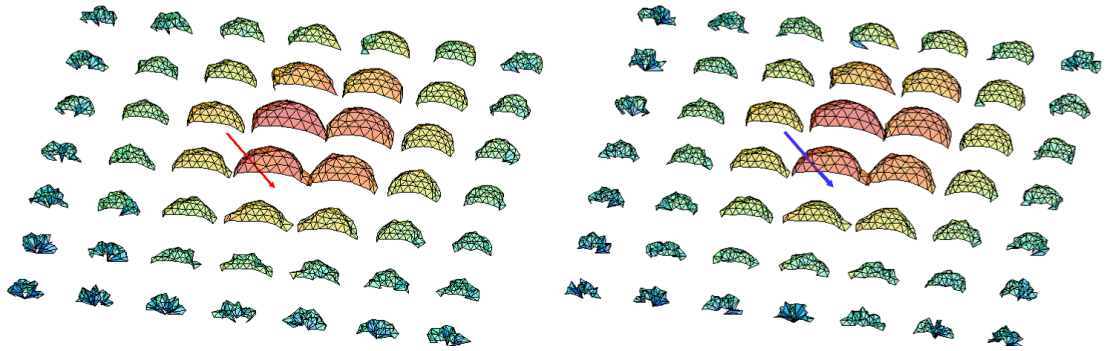

(b) rubber eraser

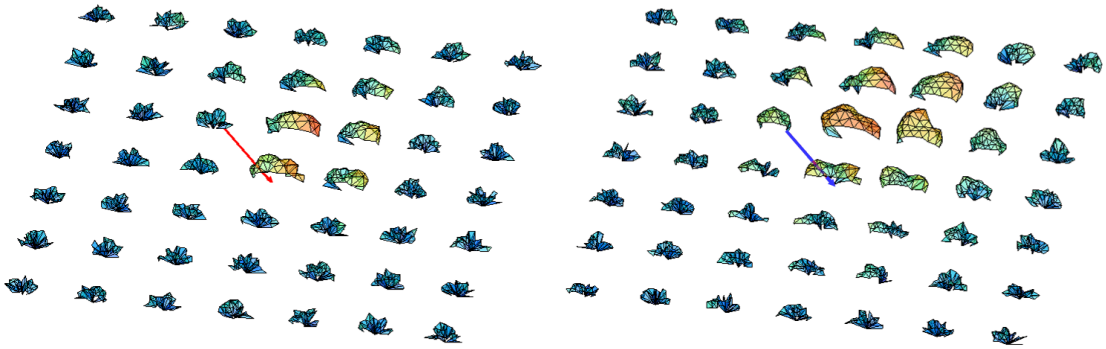

(c) marble

Figure 4.7: Visualized BSSRDF. The direction of illumination is fixed at $(\theta_i, \phi_i) = (44.9°, 74.8°)$. The left column of images in (a) - (c) presents visualizations of the BSSRDF for illumination at the red point in Fig. 4.6. The right column of images in (a) - (c) presents visualizations of the BSSRDF for fixed illumination at the blue point in Fig. 4.6. The red arrow shows the direction of illumination.

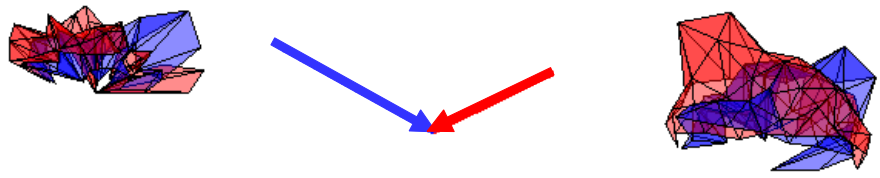

(a) epoxy resin

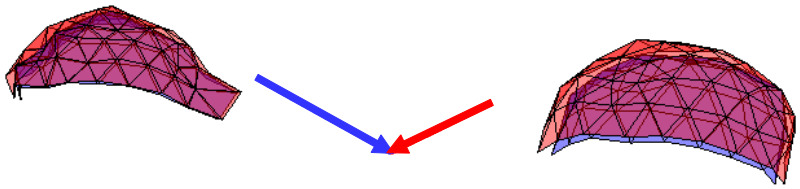

(b) rubber eraser

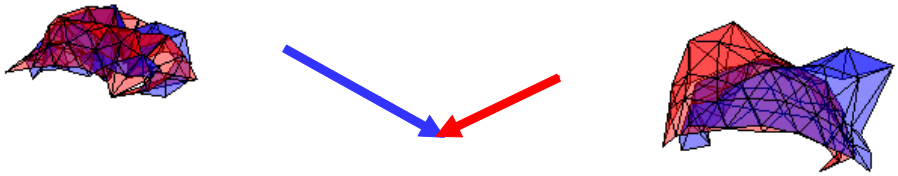

(c) marble

Figure 4.8: Close up of the visualized BSSRDF, showing the angular distribution at $(x_o, y_o) = (-10, 0), (10, 0)$. The red arrow represents the direction of illumination $(\theta_i, \phi_i) = (44.3°, 127.2°)$ and the blue arrow represents the direction of illumination $(\theta_i, \phi_i) = (43.7°, 233.7°)$. Blue and red distributions represent the visualized angular distribution for each illumination

4.3.2 Decomposition of isotropic and anisotropic components

To analyze light transport on an object surface, it is important to decompose the observed phenomenon into basic optical components. As traditional photometric methods have assumed only diffuse reflection, surface reflection is often decomposed into diffuse and specular reflection components to remove specular effect [101]. Nishino et al. [102] focused on the angular dependency of surface reflection, and decomposed surface reflection into angular dependent specular reflection and angular independent diffuse reflection. Inspired by their method, we decompose the observed BSSRDF according to the angular dependency.

In the previous section, we showed various directional dependencies of the scattered light; *i.e.*, the BSSRDF can be decomposed into an angular independent isotropic component and angular dependent anisotropic component as illustrated in Fig. 4.9. The isotropic component does not depend on the viewing direction, while the anisotropic component varies according to

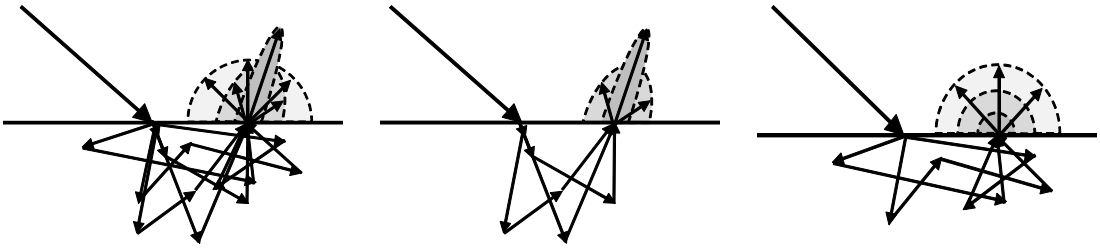

(a) Both components (b) Anisotropic component (c) Isotropic component

Figure 4.9: Concept of decomposition. We decompose sampled BSSRDFs into isotropic and anisotropic components according to the directional dependency.

the viewing direction. Hence, we formulate the decomposition as

$$f(\boldsymbol{x}_i, \boldsymbol{\omega}_i, \boldsymbol{x}_o, \boldsymbol{\omega}_o) = f_i(\boldsymbol{x}_i, \boldsymbol{\omega}_i, \boldsymbol{x}_o) + f_a(\boldsymbol{x}_i, \boldsymbol{\omega}_i, \boldsymbol{x}_o, \boldsymbol{\omega}_o), \tag{4.1}$$

where the function f_i represents the isotropic component and the function f_a represents the anisotropic component. It is noted that the argument $\boldsymbol{\omega}_o$ is not included in the function f_i because of the independency on the viewing direction.

The two components are decomposed according to the constancy of the angular distribution. To implement this idea, we refer to a separation method proposed by Nishino *et al*. [102]. In their work, they simply extracted view-independent components by taking the minimal pixel value at each surface point as a constant component over image sequences. We also apply this idea to decompose sampled BSSRDFs. The isotropic component is separated by finding the minimal value along viewing directions at each surface point:

$$f_i(\boldsymbol{x}_i, \boldsymbol{\omega}_i, \boldsymbol{x}_o) = \min_{\boldsymbol{\omega}_o \in \boldsymbol{\Omega}} f(\boldsymbol{x}_i, \boldsymbol{\omega}_i, \boldsymbol{x}_o, \boldsymbol{\omega}_o), \tag{4.2}$$

where $\boldsymbol{\Omega}$ denotes the hemispherical directions. The anisotropic component is then computed as the residual according to

$$f_a(\boldsymbol{x}_i, \boldsymbol{\omega}_i, \boldsymbol{x}_o, \boldsymbol{\omega}_o) = f(\boldsymbol{x}_i, \boldsymbol{\omega}_i, \boldsymbol{x}_o, \boldsymbol{\omega}_o) - f_i(\boldsymbol{x}_i, \boldsymbol{\omega}_i, \boldsymbol{x}_o). \tag{4.3}$$

An overview of this decomposition is depicted in Fig. 4.10.

Figure 4.11 shows the decomposition results of sampled BSSRDFs of epoxy resin, rubber eraser and marble in pseudo color. The left column shows the sum of sampled BSSRDFs for all observation directions E_{both}, the center column shows the sum of the decomposed anisotropic

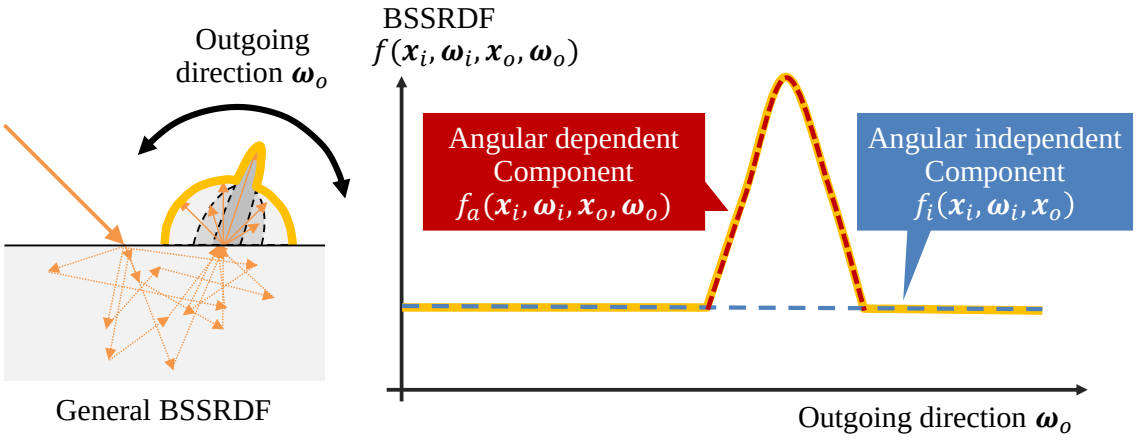

Figure 4.10: BSSRDF decomposition with analysis of outgoing direction $\boldsymbol{\omega}_o$. Constant bias in the BSSRDF corresponds to an angular independent component, and the remainder of the BSSRDF is the component dependent on angle.

BSSRDF for all observation directions E_a and the right column shows the scaled decomposed isotropic BSSRDFs E_i, which are expressed as

$$E_{both} = \sum_{\boldsymbol{\omega}_o} f(\boldsymbol{x}_i, \boldsymbol{\omega}_i, \boldsymbol{x}_o, \boldsymbol{\omega}_o), \tag{4.4}$$

$$E_a = \sum_{\boldsymbol{\omega}_o} f_a(\boldsymbol{x}_i, \boldsymbol{\omega}_i, \boldsymbol{x}_o, \boldsymbol{\omega}_o), \tag{4.5}$$

$$E_i = s f_i(\boldsymbol{x}_i, \boldsymbol{\omega}_i, \boldsymbol{x}_o). \tag{4.6}$$

As epoxy resin has strong directional scattering, most of the light is categorized in the anisotropic component. In contrast, strong multiple scattering in the rubber eraser belongs to the isotropic component. Illuminated light gradually loses its directionality as light scatters in the medium because the light path varies according to a number of scattering, such that low-bounce scattering retains the directionality, while higher-order scattering loses the directionality of a propagating light in the media. Hence, we often see anisotropic scattering in optically thin media and isotropic scattering in optically dense media. This result shows that we can decompose the scattering component into low-bounce and high-order scatterings according to the angular dependency, and the angular dependency is a clue with which to analyze optical density. Marble also has a low isotropic component because its inhomogeneous structure generates angular varying distribution. This result reveals that the spatial structure of an object affects the angular dependency of scattered light in the media.

From the above results of decomposition, we confirm that the sampled BSSRDFs can be decomposed into isotropic and anisotropic components by the analysis of the BSSRDF in out-

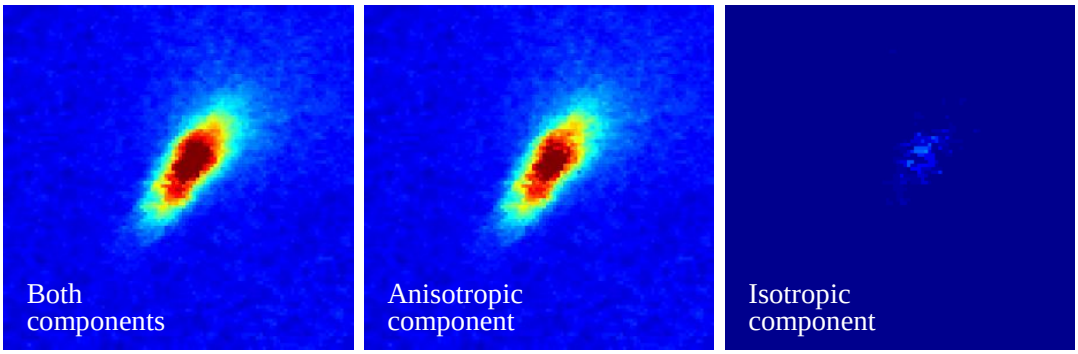

(a) epoxy resin

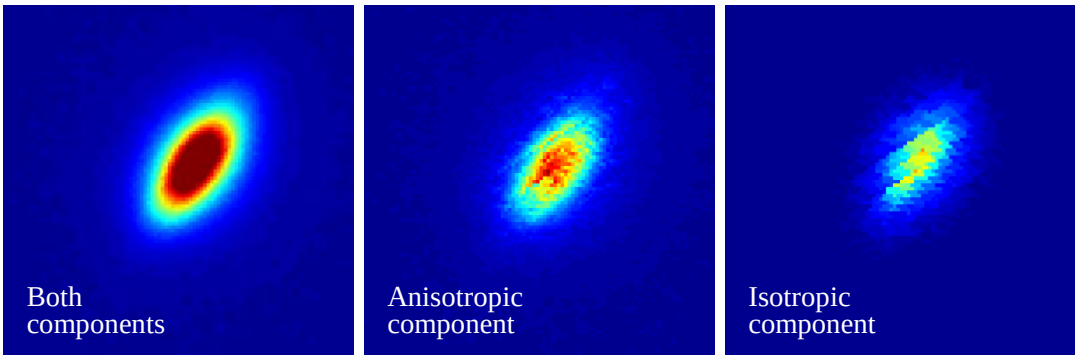

(b) rubber eraser

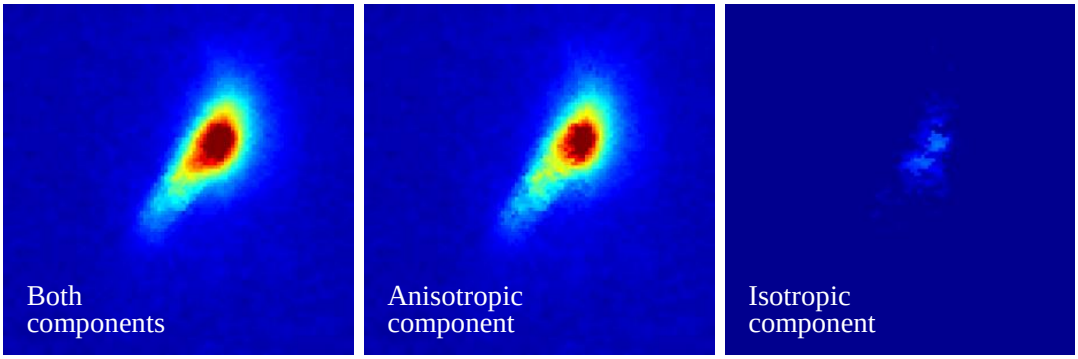

(c) marble

Figure 4.11: Decomposition results for three materials. The left column shows both components, the center column shows the decomposed anisotropic component and the right column shows the decomposed isotropic component. Each image shows the total energies of emitted light at each surface point.

going direction. In addition, we can analyze optical thickness and homogeneity using the decomposed BSSRDF.

4.3.3 Refracted light in optically thin media

As discussed in previous sections, the scattering light in optically thin media saves directionality of propagation. Generally, the incident light on an object surface is refracted and propagates into the object. Direction of a scattering light depends on refraction effect on the surface. In the optically thin epoxy resin, we previously observe the straight light distribution in Section 4.2.2. Here, we confirm whether the straight light distribution in epoxy resin relates refraction.

The path of refracted light is determined based on Snell's law with directions of incident and outgoing light, surface normal on the incident and outgoing point, and a refractive index of the target object. Thus, we can generate the observation of refracted light ray as an image with known direction of the incident and outgoing light. We compare generated image of refracted light ray and observed scattering light and then consider the these relationships.

Figure 4.12 show the plot of refracted light ray with yellow line. We superimpose the refracted light on the images in Fig. 4.5 according to direction of illumination and observation. Although the refractive index of epoxy resin is unknown, we use 1.5 as a value of refractive index for plastics. Figure 4.12 (a) shows that refracted light rays with the fixed illumination $\boldsymbol{x}_i = (0, 0)$ and $\boldsymbol{\omega}_i = (2.2°, 154.3°)$. Plots of refracted light are different in each image because images are observed from different directions. Except for the image in the fourth row and first column, plots of refracted light correspond to straight light distributions in the image. In addition, each light distribution attenuates according to refracted ray. Image in the fourth row and first column are observed from same direction of illumination. Because the light illuminates almost perpendicular direction of object surface, refracted light also travels through same direction. Thus, a plot of refracted light becomes the center point in the image. Figure 4.12 (b) shows that refracted light rays with the fixed observation $\boldsymbol{\omega}_o = (2.2°, 154.3°)$. We observe the similar result of the Fig. 4.12 (a). Each direction of refracted light corresponds to straight light distribution in the image.

From the visualization of refracted light in observed images, we confirm that the refracted light ray contributes scattering in optically thin translucent object determining direction of scattering light.

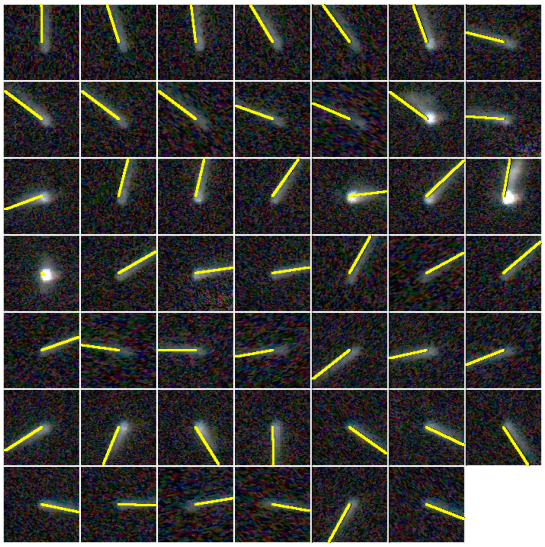

(a) Refracted light with fixed illumination

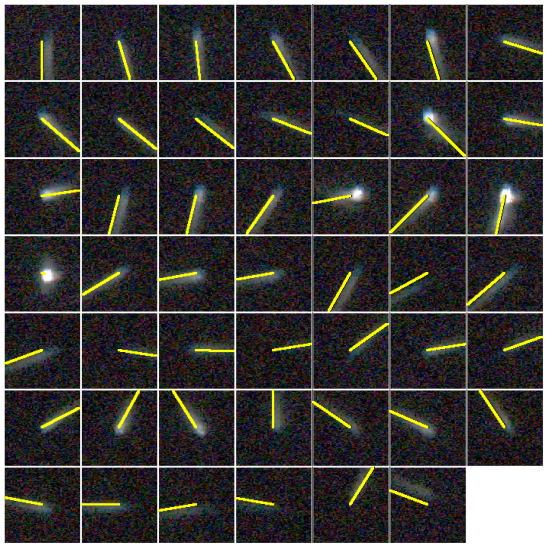

(b) Refracted light with fixed observation

Figure 4.12: Plot of refracted light ray in observed images. The left images are observed with the fixed illumination $\boldsymbol{x}_i = (0, 0)$ and $\boldsymbol{\omega}_i = (2.2°, 154.3°)$. The right images are observed with the fixed observation $\boldsymbol{\omega}_o = (2.2°, 154.3°)$. Yellow line plots refracted light in each image depending on both of direction of illumination and observations.

4.3.4 Approximation of optically thick media employing a dipole model

In the field of computer graphics, optically dense translucent materials are often synthesized using a dipole approximation model [26]. We confirm the accuracy of the dipole model using the sampled BSSRDF of an optically thick rubber eraser. The BSSRDF $f(\boldsymbol{x}_i, \boldsymbol{\omega}_i, \boldsymbol{x}_o, \boldsymbol{\omega}_o)$ based on dipole approximation is represented as

$$f(\boldsymbol{x}_i, \boldsymbol{\omega}_i, \boldsymbol{x}_o, \boldsymbol{\omega}_o) \quad = \quad \frac{1}{\pi} F_t(\eta, \boldsymbol{\omega}_o) R(\boldsymbol{x}_i, \boldsymbol{x}_o) F_t(\eta, \boldsymbol{\omega}_i), \tag{4.7}$$

where $F_t(\eta, \boldsymbol{\omega})$ is the Fresnel transmission function. $R(\boldsymbol{x}_i, \boldsymbol{x}_o)$ is the scattering term of the dipole model parameterized by scattering coefficient σ_s', absorption coefficient σ_t, and refractive index η as

$$R(\boldsymbol{x}_i, \boldsymbol{x}_o) =$$
$$\frac{\alpha}{4\pi} \left(z_r \left(\sigma_{tr} + \frac{1}{d_r(\boldsymbol{x}_i, \boldsymbol{x}_o)} \right) \frac{e^{-\sigma_{tr} d_r(\boldsymbol{x}_i, \boldsymbol{x}_o)}}{d_r^2(\boldsymbol{x}_i, \boldsymbol{x}_o)} + z_v \left(\sigma_{tr} + \frac{1}{d_v(\boldsymbol{x}_i, \boldsymbol{x}_o)} \right) \frac{e^{-\sigma_{tr} d_v(\boldsymbol{x}_i, \boldsymbol{x}_o)}}{d_v^2(\boldsymbol{x}_i, \boldsymbol{x}_o)} \right)$$

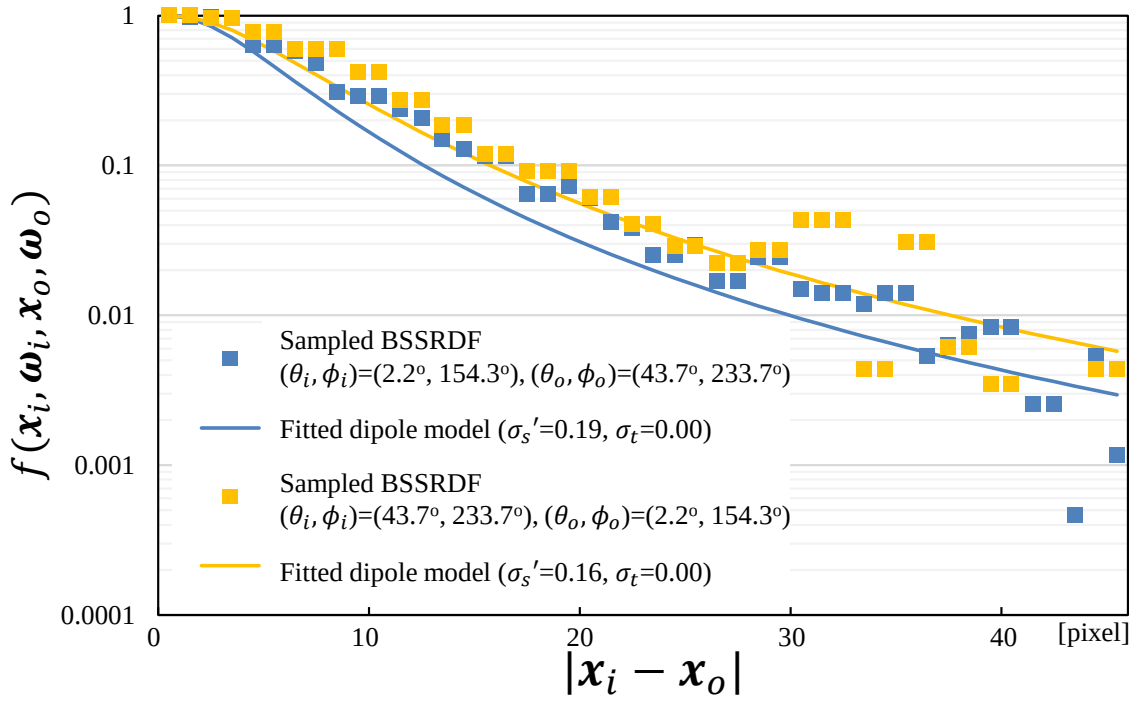

Figure 4.13: Result of dipole model fitting. Dots show the sampled BSSRDF at each ω_i, ω_o. Solid lines show the fitted dipole model.

$$
\begin{aligned}
d_r(\boldsymbol{x}_i, \boldsymbol{x}_o) &= \sqrt{|\boldsymbol{x}_i - \boldsymbol{x}_o|^2 + z_r^2}, \quad d_v(\boldsymbol{x}_i, \boldsymbol{x}_o) = \sqrt{|\boldsymbol{x}_i - \boldsymbol{x}_o|^2 + z_v^2} \\
z_r &= \frac{1}{\sigma_t'}, \quad z_v = z_r(1 + \frac{4}{3}A) \\
A &= \frac{1 + F_{dr}}{1 - F_{dr}}, \quad F_{dr} = -\frac{1.440}{\eta^2} + \frac{0.710}{\eta} + 0.668 + 0.0636\eta \\
\sigma_{tr} &= \sqrt{3\sigma_a\sigma_t'}, \quad \sigma_t' = \sigma_s' + \sigma_a, \quad \sigma_s' = \sigma_s(1 - g), \quad \alpha = \frac{\sigma_s'}{\sigma_t'}.
\end{aligned}
$$

Figure 4.13 shows the result of the dipole model fitting. We normalize the BSSRDF as $f(\boldsymbol{x}_i, \boldsymbol{\omega}_i, \boldsymbol{x}_o, \boldsymbol{\omega}_o) = 1$ at $|\boldsymbol{x}_i - \boldsymbol{x}_o| = 0$ and set refractive index $\eta = 1.3$. Blue dots show the sampled BSSRDF with $(\theta_i, \phi_i) = (2.2°, 154.3°)$ and $(\theta_o, \phi_o) = (43.7°, 233.7°)$ and orange dots show the BSSRDF with interchanged illumination and observation angles.

As shown in Fig. 4.13, the sampled BSSRDFs are similar. This observation satisfies the model described as eq. (4.7) in which the BSSRDF with arbitrary $\boldsymbol{\omega}_i$ and $\boldsymbol{\omega}_o$ corresponds to the BSSRDF with interchanged $\boldsymbol{\omega}_i$ and $\boldsymbol{\omega}_o$. Fitting results are shown by solid lines. The estimated parameters are $\sigma_t' = 0.19, \sigma_a = 0.0$ to $(\theta_i, \phi_i) = (2.2°, 154.3°)$ and $\sigma_t' = 0.16, \sigma_a = 0.0$ to $(\theta_i, \phi_i) = (43.7°, 233.7°)$. Although the estimated parameters are slightly different, the

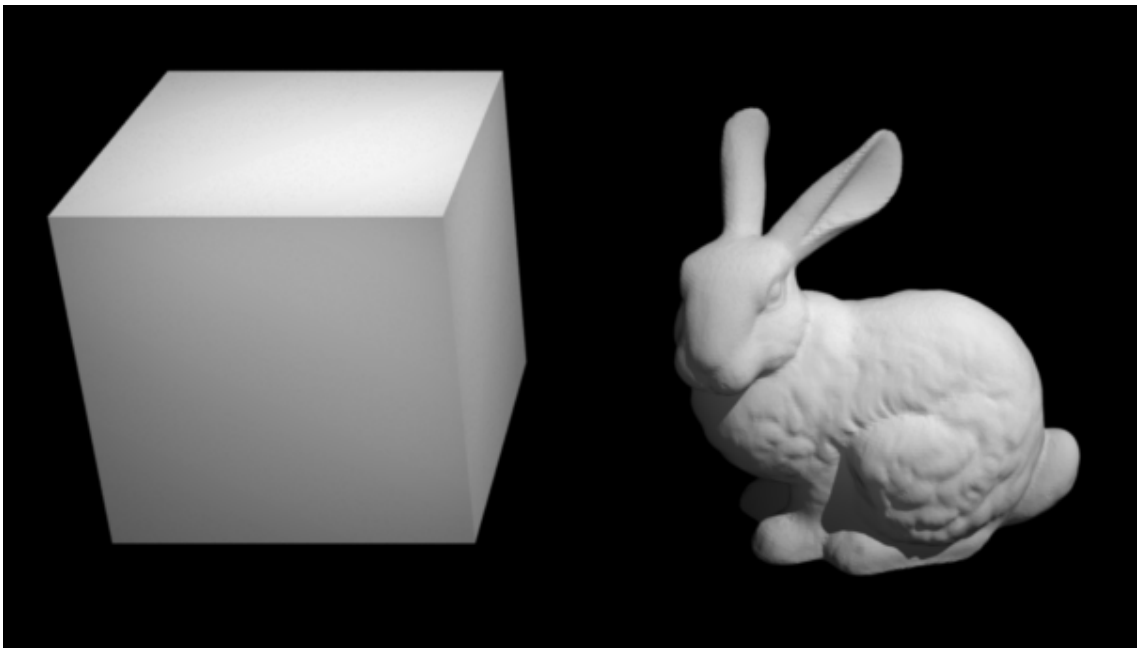

Figure 4.14: Synthesized image with parameters estimated by dipole model fitting.

BSSRDFs are approximated with little error. Figure 4.14 shows the image synthesized using the dipole model with estimated parameters. The synthesized appearances are similar to the appearance of the rubber eraser in Fig. 4.4 (b). The results confirm that the appearance of a rubber eraser can be approximated using a dipole model.

4.4 Discussion

In this chapter, we presented a novel method of sampling and analyzing full-dimensional BSSRDFs. For sampling, we used the *Turtleback reflector*, which is a polyhedral mirror system that illuminates and observes the object surface from various directions by virtual projectors and cameras. This system samples the full-dimensional BSSRDF in relatively short time. For analysis, we visualized spatial and angular distributions by slicing BSSRDFs with fixed incident light ray and direction of outgoing direction. The analysis on directional distributions of the light transport has already done in research on BRDFs, the analysis on incident and outgoing points is achieved by the full-dimensional BSSRDF. In addition, we decomposed the BSSRDF into angular isotropic and anisotropic components by the analysis of outgoing direction. The analysis revealed that the ratio of the two components strongly depends on the optical thickness and homogeneousness of the medium.

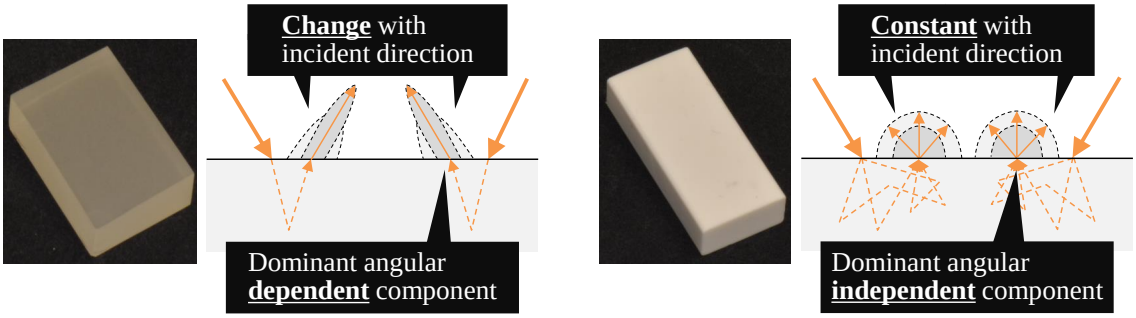

Optically thin object
(epoxy resin)

Optically thick object
(rubber eraser)

Figure 4.15: Summary of the analysis of the BSSRDF in terms of optical thickness. Light transport in optically thin and thick objects has different characteristics of directionality.

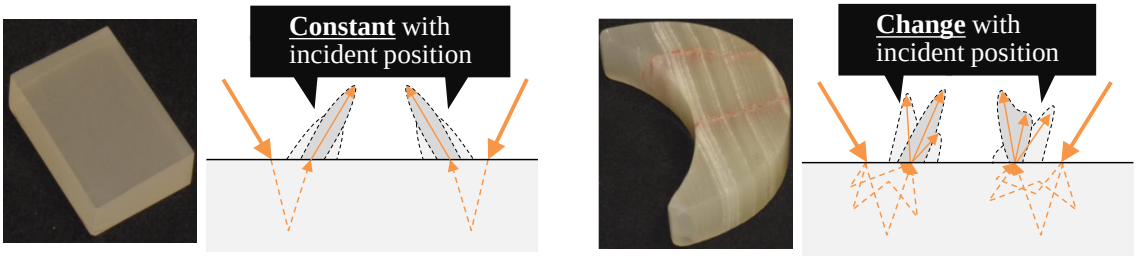

Optically homogeneous object
(epoxy resin)

Optically inhomogeneous object
(marble)

Figure 4.16: Summary of the analysis of the BSSRDF in terms of optical homogeneity. Light transport has spatially different propagation.

We summarize the characteristics of light transport in translucent media, which are analyzed using the full-dimensional BSSRDFs in Figs. 4.15 and 4.16. Here, we discuss an appropriate model to represent scattering in translucent media, which we will use in the following chapters.

In optically thin translucent media, observed light transport depends on the incident and outgoing direction because the incident light attenuates around the refracted light ray. Small number of particles in optically thin media does not prevent the incident light from traveling through the media, and the light does not spatially distribute but travels along a refracted ray. Thus, scattering light in optically thin translucent media can be modeled by light attenuation along with the refracted light ray depending on direction of the incident and outgoing light. Analysis of refracted light in optically thin media as described in Section 4.3.3 also shows this phenomena.

Meanwhile, incident light in optically thick translucent media does not depend on the direc-

tion of the incident and outgoing light, because the light loses its directionality due to repeated scatterings in the media. Repeated scatterings make uncountable light paths, and the light randomly travels in the media independently of incident and outgoing directions. This means that we can ignore the effect of directions of incident and outgoing light in modeling scattering light in optically thick translucent media. The dipole model that we use for the model fitting of scattering light on a rubber eraser is parameterized using only the distance between an incident point and outgoing point $|\boldsymbol{x}_i - \boldsymbol{x}_o|$ without the directions of the incident and outgoing light.

While we select a scattering model focusing on angular dependency to deal with optical thickness, we have to additionally change the scattering model at each position to deal with optical homogeneity. A spatially variant translucent medium is difficult to represent with the parametric model owing to the complex structure of the medium such as optical discontinuity owing to cracks between optically different layers [103]. In addition, it is difficult to deal with completely different appropriate scattering models according to the optically thickness at each position in the same formulation. Hence, we calibrate or estimate scattering model at each position for the spatially varying translucent medium to avoid complex parametric expression of scattering model.

Based on these analyses of the scattering model, we propose shape estimation methods for optically thin and optically thick translucent objects in the following chapter.

Chapter 5

Shape Estimation of an Optically Thin Translucent Objects

From this chapter, we propose a shape estimation method for a translucent object based on the discussion in Section 4.4. Firstly, we present the estimation method for optically thin translucent objects.

5.1 Introduction

When traveling through a translucent medium, light collides with particles and scatters in the medium. Because the density of particles is low in optically thin translucent media, incident light rarely collides with particles and travels almost in a straight line. Thus, attenuated light is often observed around refracted light as shown in Section 4.3.

The attenuation of light is modeled using the Lambert-Beer law [104] in physics. The law describes that incident light exponentially attenuates along the length of the light path in a medium. While the light path of scattering is usually complex owing to uncountable collisions with particles, the light path of a single scattering is identified uniquely because light collides with a particle only once in the medium. Propagating light in an optically thin medium is dominated by low-bounce scattering, and the light attenuation model of single scattering is thus appropriate for our target.

In this chapter, we develop a shape estimation method based on the observation of single scattering, and its attenuation along the light path. We derive a solution method using a scattering model that takes into account the refraction, an extinction coefficient, and a phase function.

The primary contributions of this work are as follows. We propose a new shape estimation technique based on the scattering effect for translucent objects. Scattering is introduced as a

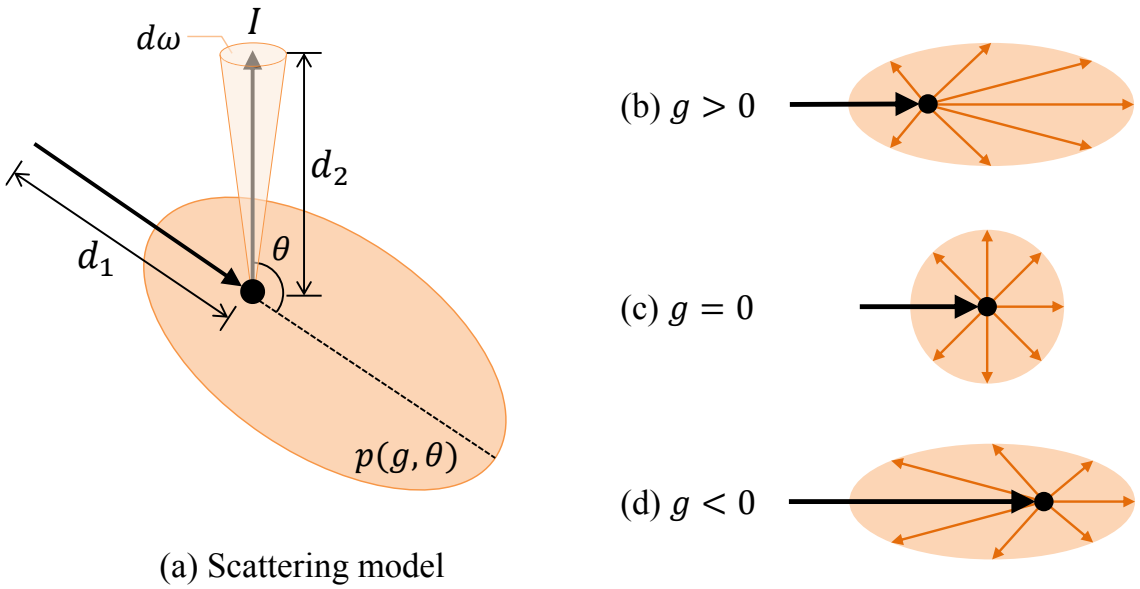

(a) Scattering model

Figure 5.1: Illustration of the scattering model and examples of distribution profiles with a varying phase function.

signal beneficial for determining the shape. The proposed method is effective when the target object generates strong transmitted scattering, which is a situation in which other shape estimation approaches cannot be applied. This work is the first attempt to directly use the observed intensities of single scattering for shape measurement. Additionally, we develop an effective solution method based on energy minimization for the simultaneous estimation of the shape and scattering parameters.

5.2 Shape from Single Scattering

5.2.1 Background

Figure 5.1(a) shows a parametric single scattering model. In a scattering medium, incident light exponentially attenuates along the length of the light path according to the Lambert-Beer law [104]. It also scatters through a solid angle in the medium, and a good approximation of the phenomenon is the Henyey-Greenstein phase function [105]. With this phase function, the observed intensity I of single scattering is described as [39, 41]

$$I = sp(g,\theta)e^{-\sigma_t(d_1+d_2)}d\omega, \tag{5.1}$$

$$p(g,\theta) = \frac{1}{4\pi}\frac{1-g^2}{(1+g^2-2g\cos\theta)^{\frac{3}{2}}}, \tag{5.2}$$

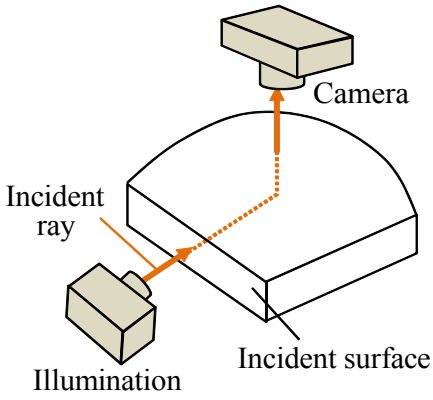

Figure 5.2: Setting for shape estimation. A translucent object is illuminated from the side and observed from the top.

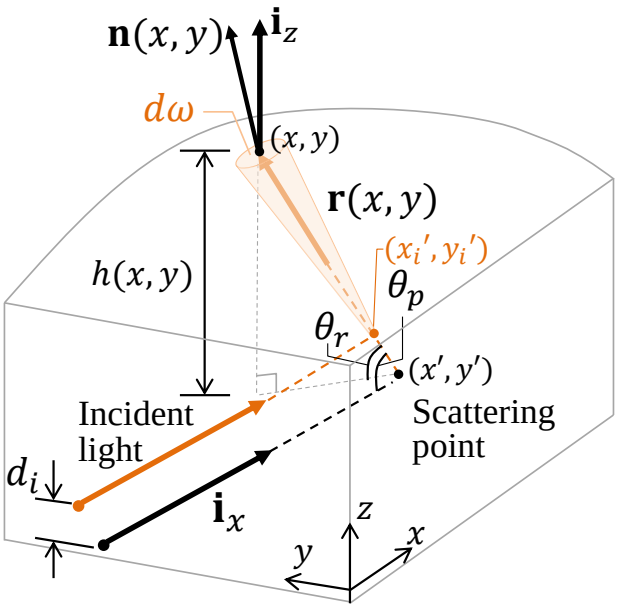

Figure 5.3: Light path in the target object. The incident plane is almost planar, and incident light is assumed to be parallel to the x-axis. The illuminated ray reaches the surface point (x, y), changing its travel direction at the scattering point (x', y').

where s is a scaling constant that includes the intensity of the incident light and scattering coefficient, σ_t is an extinction coefficient, $(d_1 + d_2)$ is the length of the light path in the medium, $d\omega$ is the solid angle of the light ray, and $p(g, \theta)$ is the phase function. The phase function represents the scattering distribution, and the distribution profile is controlled by a parameter g $(-1 \leq g \leq 1)$. Figures 5.1(b), (c), and (d) show examples of the distribution profiles produced by varying g.

5.2.2 Formulation

We formulate the relationship between observed intensities of single scattering and the shape of a translucent target. Figure 5.2 shows our setting for the shape measurement. A translucent object is illuminated from one side and observed from the top. We assume a homogeneous material as a target object and orthographic projection for both illumination and observation. We also assume that a incident light ray attenuates along horizontal line in an object and does not reflect on other surfaces of the object. In addition, we ignore multiple scattering for now, but explain a method for handling it in later sections.

Figure 5.3 illustrates a light path of single scattering in a medium. The incident ray $\mathbf{i}_x$ scatters through a solid angle $d\omega$ at scattering point (x', y'), and reaches surface point (x, y). $\mathbf{n}(x, y)$ represents the surface normal and $\mathbf{i}_x = [1, 0, 0]^T$ and $\mathbf{i}_z = [0, 0, 1]^T$ are incident and exiting light vectors, respectively. $\mathbf{r}(x, y)$ is a unit scattering vector pointing from the scattering point (x', y') to the surface point (x, y). The angle between the incident vector $\mathbf{i}_x$ and the scattering vector $\mathbf{r}(x, y)$ is denoted as θ_p. θ_r represents the projected angle of θ_p on the plane spanned by $\mathbf{r}(x, y)$ and $\mathbf{i}_z$. Our purpose is to estimate the height of the translucent object $h(x, y)$ from the observed intensity $I(x, y)$ at the surface point (x, y) on the surface, where the height of the incident ray is $z = 0$. The scattered incident ray $\mathbf{i}_x$ is finally refracted at the object surface. The angle of refraction obeys Snell's law, expressed as

$$\mathbf{n}(x, y) \times \mathbf{i}_z = \eta \mathbf{n}(x, y) \times \mathbf{r}(x, y), \tag{5.3}$$

where η is the refractive index, and $\times$ represents a cross-product operator. The total length of the light path becomes the sum of x', which corresponds to the sum of the distance from the incident point to the scattering point and the distance from the scattering point to the surface point, $h(x, y)/\sin\theta_r$. As the intensity of single scattering is modeled as eq. (5.1), the observed intensity is expressed as

$$\begin{aligned} I(x, y) &= s F_t^{in} F_t^{out}(x, y) p(g, \theta_p) e^{-\sigma_t \left(x' + \frac{h(x,y)}{\sin\theta_r}\right)} d\omega(h(x, y), \theta_r), \\ d\omega(h(x, y), \theta_r) &= \frac{\sin\theta_r dA}{h(x, y)^2}, \end{aligned} \tag{5.4}$$

where s is a scaling constant, $F_t^{out}(x, y)$ is the Fresnel transmittance on the surface point (x, y), and F_t^{in} is the constant Fresnel transmittance on the incident point because the incident light is perpendicular to the incident plane. dA is the physical size of a pixel in the observed image. Equation (5.4) shows that the observed intensity depends on both the geometric shape and scattering parameters, namely the extinction parameter σ_t, refractive index η, and phase function parameter g. Given these scattering parameters, the height of the translucent object is determined to an unknown offset owing to s as

$$\begin{aligned} h(x, y) = \frac{\sin\theta_r}{\sigma_t} \big(&\log s + \log F_t^{in} + \log F_t^{out}(x, y) + \log p(g, \theta_p) \\ &+ \log d\omega(h(x, y), \theta_r) - \log I(x, y)\big) - x' \sin\theta_r. \end{aligned} \tag{5.5}$$

.

5.3 Solution method

In the previous section, we described a basic theory for obtaining the shape from single scattering. However, in reality, we cannot directly estimate the object height $h(x, y)$ using eq. (5.5) because of the unknown parameters and unclosed form of the function. In addition, the observed intensities include contributions from not only single scattering but also multiple scattering. In this section, we discuss a method that solves these problems. Our method assumes that the refractive index η is known because it can be directly measured using a refractometer.

5.3.1 Shape estimation by energy minimization

In our method, we employ an energy minimization approach to simultaneously determine both the shape and scattering parameters. When the unknown parameters and height are correctly estimated, eq. (5.4) should give an intensity that is equivalent to the observed intensity $I(x, y)$. Although we can estimate the unknown parameters by seeking parameters that generate the observed intensity, parameter estimation tends to be unstable owing to a larger number of unknown parameters than the captured intensity. To reliably derive a solution to this problem, we use multiple $n(2 \leq n)$ images that are captured by changing the height of the incident ray; *i.e.*, we record multiple intensities $I_i(x, y)$ with varying heights of the incident rays $z = d_i \ \ (i = 1, \ldots, n)$ as shown in Fig. 5.3. We now have n intensity observations per scene point $I_i(x, y)$, expressed as

$$I_i(x, y) = sF_t^{in}F_t^{out}(x, y)p(g, \theta_p)e^{-\sigma_t(x_i' + \frac{h(x,y)-d_i}{\sin\theta_r})}d\omega(h(x, y), \theta_r), \quad i = 1, \ldots, n. \tag{5.6}$$

We also take into account the signal-to-noise ratio of the observed intensities; the darker observations suffer more from image noise while the brighter observations are more reliable. We incorporate this by introducing a weighting factor w_i when determining the unknown parameters. We thus define an energy function for computing heights $h(x, y)$ and scattering parameters s, g, σ_t as

$$E(h(x, y), s, g, \sigma_t) = \sum_i w_i \sum_{x,y} \left(I_i(x, y) - I_i^{gen}(h(x, y), s, g, \sigma_t)\right)^2, \tag{5.7}$$

where I_i^{gen} is the generated intensity obtained using eq. (5.6), and w_i is a weighting factor that reduces the effect of noise. We define the weighting factor w_i as

$$w_i = \frac{\sum_{x,y} I_i(x, y)}{\sum_{k=1}^{n} \sum_{x,y} I_k(x, y)}. \tag{5.8}$$

The energy function E evaluates the closeness between the observed intensity and intensity generated using eq. (5.6). The minimization of the energy function E gives us estimates of the height $h(x, y)$ per-pixel and scattering parameters s, g and σ_t as

$$\{h(x,y), s, g, \sigma_t\} = \underset{h(x,y),s,g,\sigma_t}{\operatorname{argmin}} E(h(x,y), s, g, \sigma_t). \tag{5.9}$$

We describe the optimization method in the following section.

5.3.2 Implementation

This section describes the implementation details of the solution method. Our method employs non-linear optimization because of the non-convexity of eq. (5.7) with respect to the unknown parameters. We now describe the method for making the initial guess of the height $h(x, y)$ and the following optimization strategy.

Estimation of initial shape

To make an initial guess of the estimated parameters, we use the initial shape $h^0(x, y)$ computed by ignoring refraction ($\eta = 1$). When $\eta = 1$, the scattering vector coincides with the output vector $\mathbf{i}_z$, the two-dimensional projection of the scattering point (x', y') becomes identical to the surface point (x, y), and Fresnel transmittance $F_t^{out}(x, y)$ is constant because refraction is disregarded. Since the angle θ_p equals $\pi/2$, the phase function $p(g, \theta_p)$ becomes constant. In addition, we assume that solid angle $d\omega(h(x, y), \theta_r)$ is a constant value. The intensity generated from initial height $h^0(x, y)$ is described as

$$I_i^0(x,y) = Se^{-\sigma_t(h^0(x,y)+x-d_i)}, \quad S = sF_t^{in}F_t^{out}p\left(g, \frac{\pi}{2}\right)d\omega. \tag{5.10}$$

Here, unknown parameters are the height $h^0(x, y)$, scaling constant S, and extinction coefficient σ_t. Using a pair of intensity observations $I_i(x, y)$ and $I_j(x, y)$ obtained for different heights of incident rays d_i and d_j, the extinction coefficient is calculated as

$$\sigma_t = \frac{\log I_i(x,y) - \log I_j(x,y)}{d_i - d_j} \quad (d_i \neq d_j). \tag{5.11}$$

In practice, we take the average for all pairs of d_i and d_j as the estimate of σ_t. We employ the intensity at the incident point as the initial scaling constant S for the scaling without attenuation. The initial guess of the height $h^0(x, y)$ is therefore described as

$$h^0(x,y) = \frac{1}{\sigma_t}\left(\log S - \log I_i(x,y)\right) - x + d_i, \tag{5.12}$$

and is estimated using the parameters σ_t and S. We use this initial guess as an input to the optimization: $h(x, y) \leftarrow h^0(x, y)$.

Optimization

Now we estimate the shape and parameters by minimizing eq. (5.9) using h^0 as the initial guess of the shape. The unknowns to be estimated are the per-pixel height $h(x, y)$ and scattering parameters s, g, and σ_t. To efficiently avoid local minima, we use a two-step approach for the optimization. Specifically, we first apply particle swarm optimization [106] to limit the search range in a coarse manner, and then use the Nelder-Mead method [107] to find the optimal parameter set on a fine scale.

Extraction of single scattering

As discussed above, actual observations are both of single and multiple scatterings as shown in Chapter 3.1. To separate the single scattering component from multiple scattering, we employ a separation method [39] that uses a projector as a light source, as shown in Fig. 5.4. We illuminate one-dimensional high-frequency stripe pattern and capture several images with shifting its phase to an object. Although black pixels do not directly illuminate the object, the brightness of regions corresponding to black pixels is not zero due to multiple scattering. Since the brightness of unilluminated regions does not change with shifted projection, the constant component corresponds to multiple scattering. We extract the multiple scattering component $I_{multiple}$ as the constant component by taking minimal value along observed images with shifted projection. In actual, the extracted minimal value I_{min} is the half of multiple scattering $I_{multiple}$ because the high-frequency stripe pattern illuminates the half of pixels on a horizontal line. Thus, the multiple scattering is the two times of the constant component as

$$I_{multiple} = 2I_{min}. \tag{5.13}$$

On the other hand, the illuminated region in observed image includes both single scattering and multiple scattering. Thus, the image I_{max} by taking maximum value along images with shifted observed images has both single scattering and multiple scattering. Then, we obtain single scattering by subtracting the constant component I_{min} from I_{max} as

$$I_{single} = I_{max} - I_{min}. \tag{5.14}$$

Although this method allows us to extract the single scattering component easily, accuracy of separation depends on frequency of stripe pattern [108]. In the experiment, we select appropriate frequency to separate scattering components on target objects.

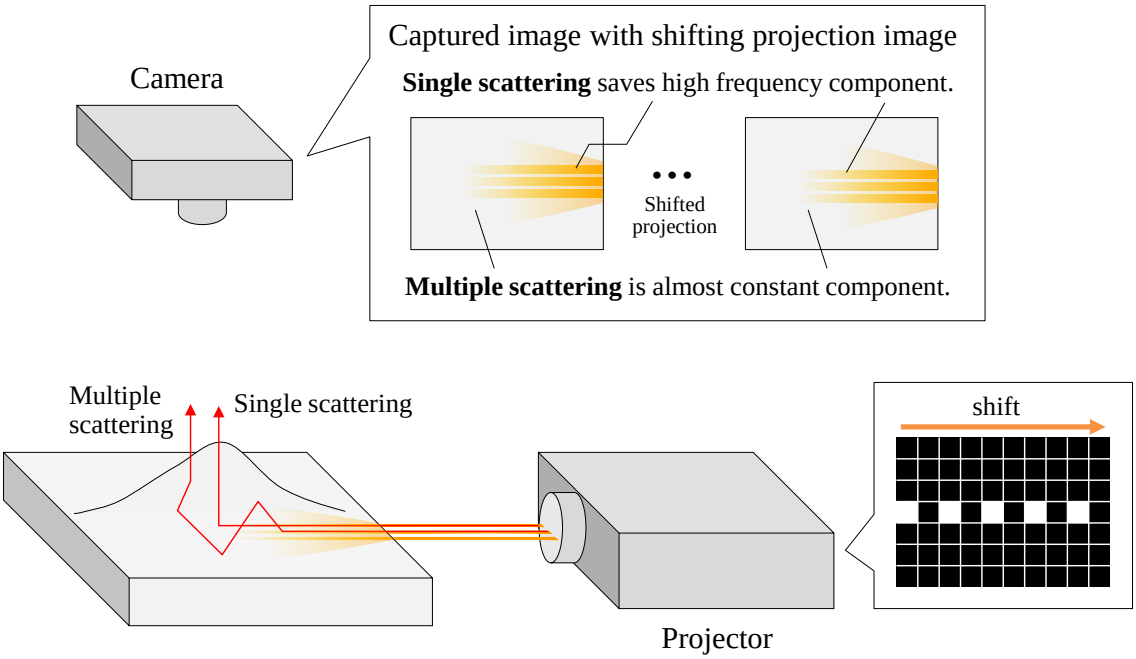

Figure 5.4: Decomposition method employing the projection of high-frequency illumination. In this setting, single scattering and multiple scattering are observed as a high-frequency component and almost constant component, respectively. Hence, single and multiple scatterings are decomposed by analyzing the difference in captured images, using a shifting projection pattern.

5.4 Experiments

We assess the effectiveness of the proposed method for both synthetic and real-world scenes. For the synthetic scenes, we assess the accuracy of the proposed method by making a comparison with the ground truth. For the real-world scenes, we prepare two objects where the ground truth shape is available while the scattering parameters are unknown.

5.4.1 Synthetic scenes

For the synthetic scene experiment, we use two one-dimensional curved surfaces and one discontinuous surface $h(x)$ as the scenes, referred to as Scenes A, B, and C. For each scene, we simulate intensity observations $I_i(x)$ with varying heights of incident rays $d_i = 0.2 \times i$[mm], $i = 0, \cdots, 9$ using the scattering model of eq. (5.6). We add Gaussian noise to the intensity observations at five levels ($\mu = 0$ and $\sigma = 0, 5, 10, 15, 20$). The optical parameters are consistently set to $\eta = 1.2$, $g = 0.1$, $\sigma_t = 0.15[\text{mm}^{-1}]$, and $s = 50000$.

Figure 5.5(a) shows Scene A and (b) shows the simulated intensity observation in the case of Gaussian noise $\sigma = 10$. From this intensity, we estimate the object shapes. Figure 5.5(c)

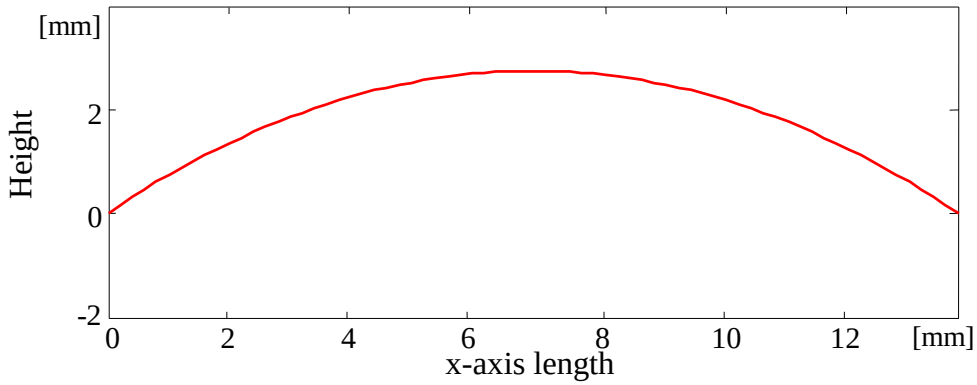

(a) Synthetic scene

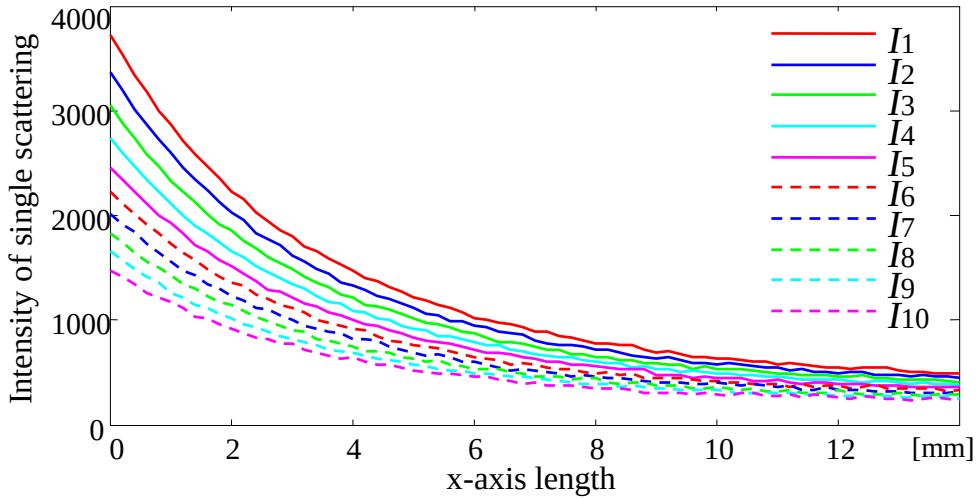

(b) Intensity observations

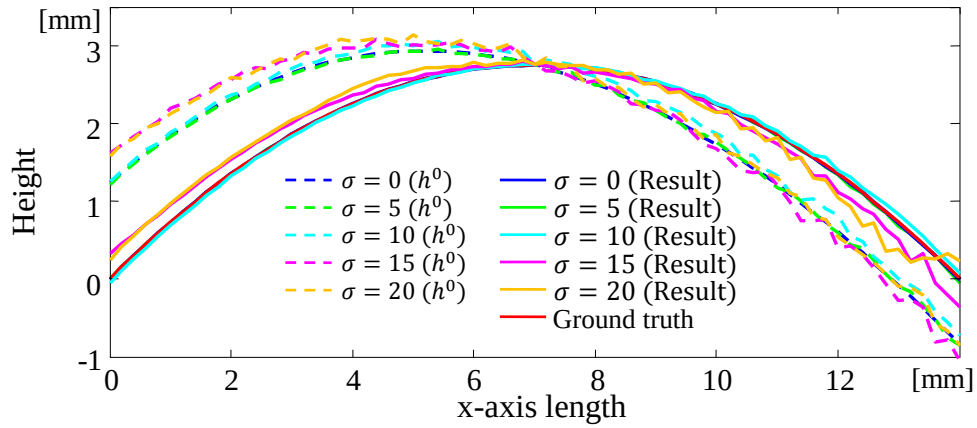

(c) Estimated result at each noise level

Figure 5.5: Estimated heights of Scene A

Table 5.1: Estimated parameters and RMSE of the estimated height at each noise level.

	Scaling constant s	Parameter g	Extinction coefficient σ_t [mm^{-1}]	RMSE of height [mm^{-1}]
Ground truth	5.0×10^4	0.1	0.15	—
$\sigma = 0$	5.08×10^4	0.069	0.15	0.05×10^{-1}
$\sigma = 5$	4.95×10^4	0.007	0.15	0.15×10^{-1}
$\sigma = 10$	4.95×10^4	0.002	0.15	0.42×10^{-1}
$\sigma = 15$	6.09×10^4	-0.002	0.16	1.64×10^{-1}
$\sigma = 20$	6.33×10^4	0.003	0.16	1.90×10^{-1}

shows the estimated result of Scene A. The initial height is globally skewed owing to the inaccurate assumption of the refractive index $\eta = 1$ and local deformations due to observation noise. In particular, when the Gaussian noise levels are $\sigma = 15$ and 20, the estimated shapes become noisier as the length of the light path increases because of the low signal-to-noise ratio. However, optimized results consistently agree well with the ground truth except for some fluctuations.

Estimated scattering parameters and the root-mean-square error (RMSE) values are summarized in Table 5.1. With small noise, the scaling parameter s and extinction coefficient σ_t are almost correct. The scattering parameter g has a larger deviation from its ground truth. Although g controls the scattering distribution, it affects both the intensity scale and intensity attenuation depending on the object shape. Thus, estimating g becomes more difficult than estimating other parameters. While the RMSE increases according to the noise amplitude, the overall errors are small and demonstrate the accuracy of the method.

Other experimental results are obtained for a synthetic one-dimensional stepped shape (Scene B) and two-dimensional pyramid like shape (Scene C). The ground truth and estimation result in the case of Gaussian noise $\sigma = 10$ are shown in Fig. 5.6(a) and Fig. 5.7(a). Scattering parameters are the same as those in the experiment for Scene A. Figure 5.6 shows experimental results for Scene B. The initial estimation has errors along a discontinuous edge because the intensity of the synthesized observations changes discontinuously. The estimation well converges to the ground truth, and scattering parameters are estimated almost correctly as $s = 4.89 \times 10^4$, $g = 0.044$, and $\sigma_t = 0.15$[mm^{-1}]. Figure 5.7 shows results for Scene C, which is an asymmetric and discontinuous scene. Although the initial shape as shown in Fig. 5.7(c) also has errors along the ridges of the pyramid shape, these errors are reduced in the final estimation.

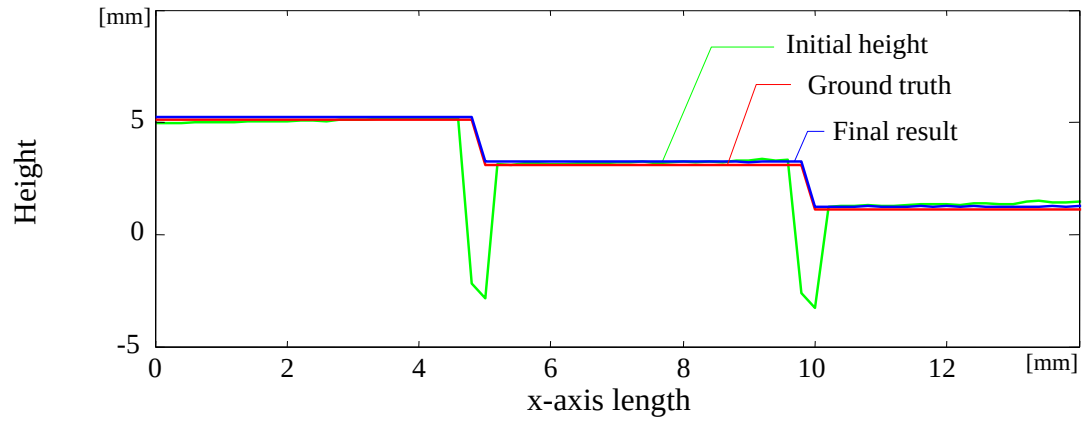

(a) Scene B and estimation result

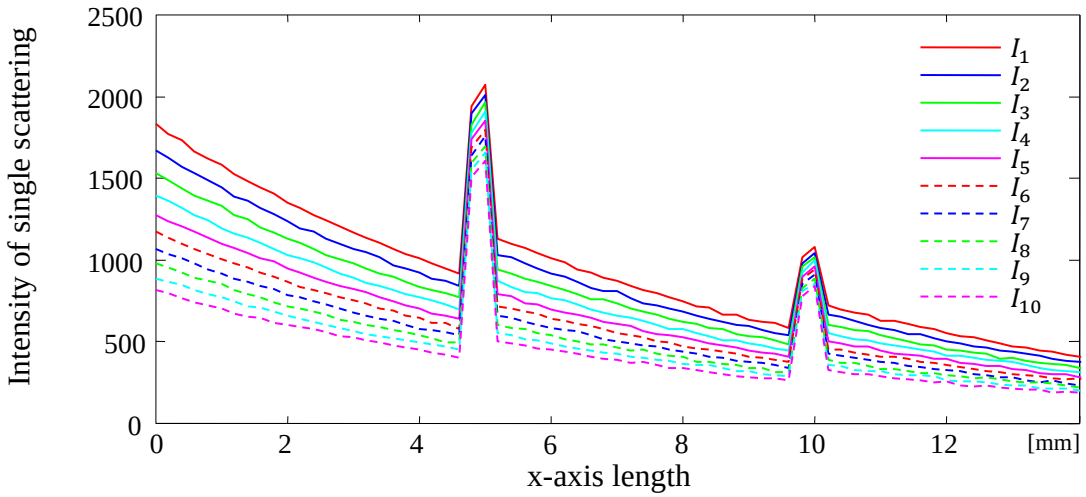

(b) Intensity observations

Figure 5.6: Estimated heights of discontinuous Scene B. Estimated scattering parameters are $s = 4.89 \times 10^4$, $g = 0.044$, and $\sigma_t = 0.15[\text{mm}^{-1}]$.

Estimated scattering parameters are $s = 4.33 \times 10^4$, $g = 0.025$, and $\sigma_t = 0.147[\text{mm}^{-1}]$. For these asymmetric and discontinuous scenes as well, the estimation well converges to near the ground truth. The scaling parameter s and extinction coefficient σ_t as scattering parameters are also estimated correctly.

5.4.2 Real-world scenes

We also applied the proposed method to real-world scenes. Figure 5.8 shows the experimental setting. A 3M MPro110 projector was placed on the side of the target object, and a Point Grey Grasshopper camera that had a linear response sensor was vertically placed to obtain a

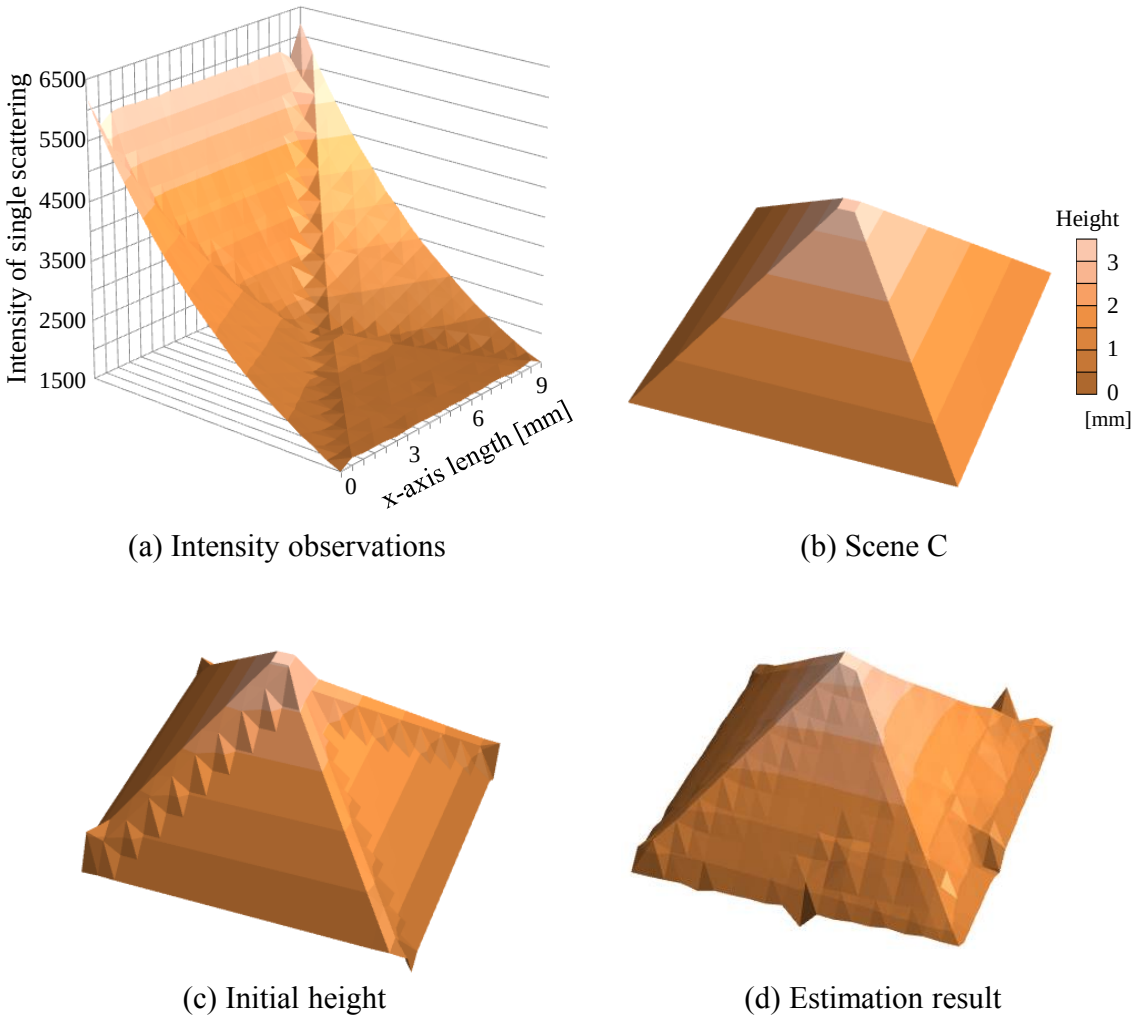

(a) Intensity observations

(b) Scene C

(c) Initial height

(d) Estimation result

Figure 5.7: Estimated heights of discontinuous and asymmetric Scene C. The estimated parameters are $s = 4.33 \times 10^4$, $g = 0.025$, and $\sigma_t = 0.147[\text{mm}^{-1}]$.

top view. To avoid the perspective effect of the imaging system, we used an Edmund optics telecentric lens for approximating an orthographic projection. To perform a comprehensive analysis, we used two different shapes of translucent objects, one being concave and the other being convex. We made these objects using the same material as shown in Fig. 1.1 (b). We show target objects and their sizes in Figure 5.9. The ground truth of these objects was known for quantitative evaluation. We set the refractive index η as 1.3. We captured intensities of single scattering $I_i(x, y)$ $(d_i = 0.25 \times i[\text{mm}], i = 0, \cdots, 9)$ while shifting the height of incident light.

Figure 5.10 shows the experimental result for the concave object. Figure 5.10(a) shows the decomposition of the scattering components in pseudo color. We also horizontally plot intensities of each scattering component in Fig. 5.10(b). The red, green, and blue plots show the

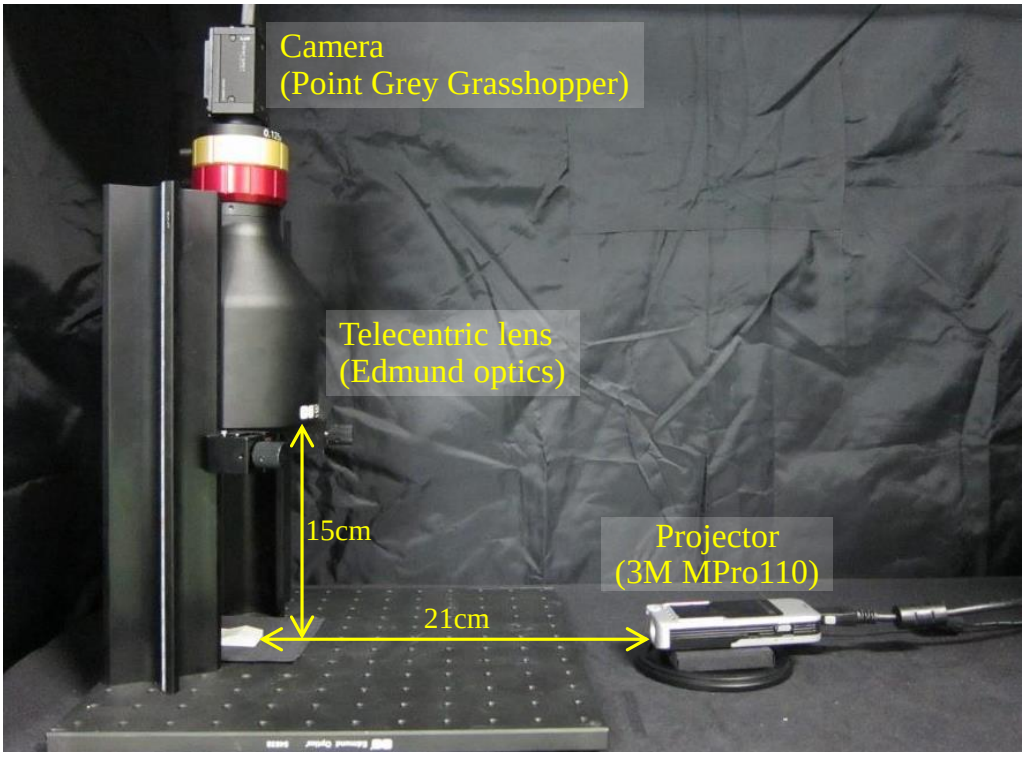

Figure 5.8: Experimental setting. A projector is placed on the side of the object, and a camera is vertically placed. We used a telecentric lens for orthographic projection.

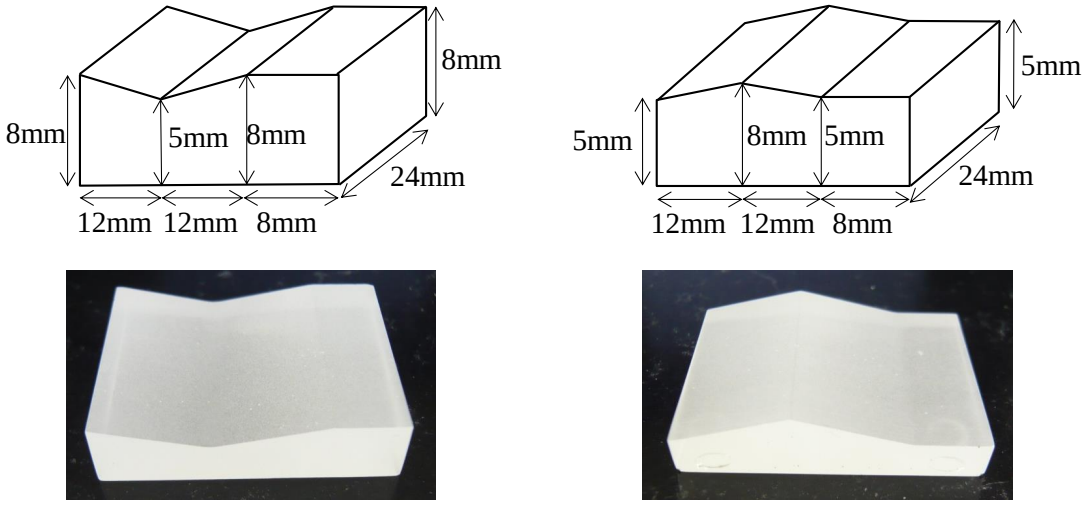

(a) Concave scene (b) Convex scene

Figure 5.9: Target objects for evaluation

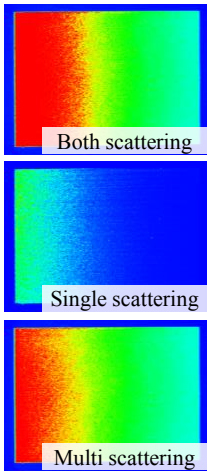

(a) Decomposed scattering

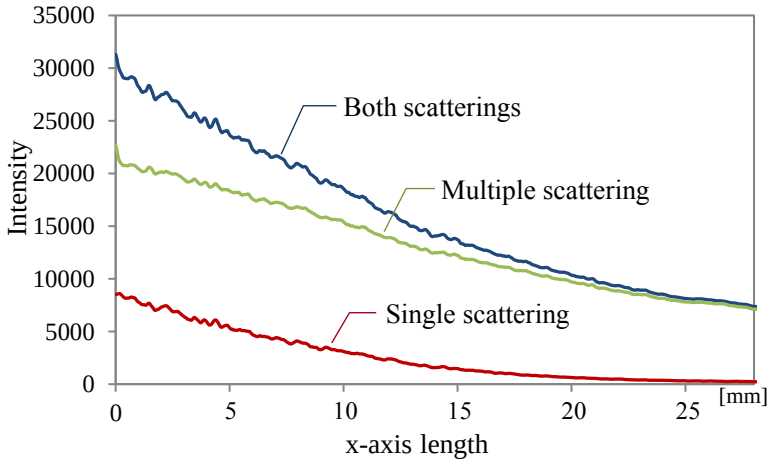

(b) Plot of scattering components

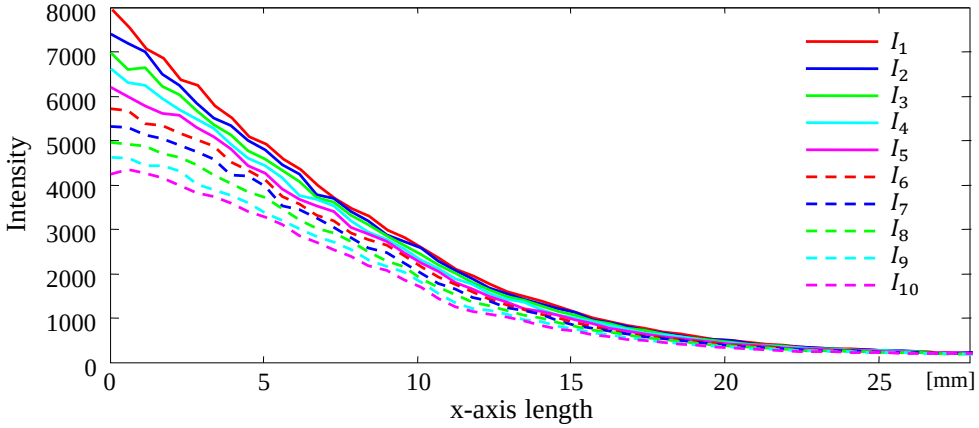

(c) Plot of single scatterings

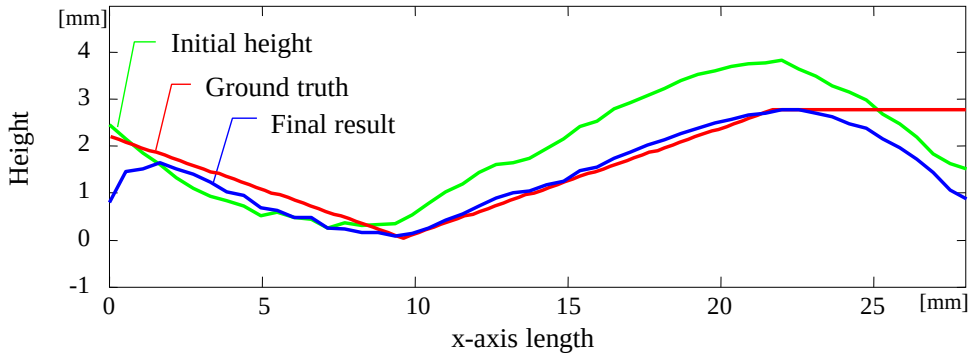

(d) Estimated shape

Figure 5.10: Experimental result for a concave scene.

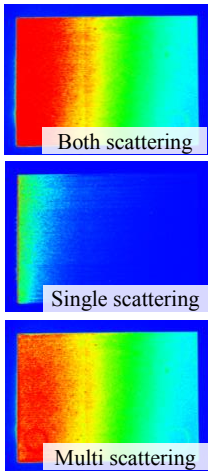

(a) Decomposed scattering

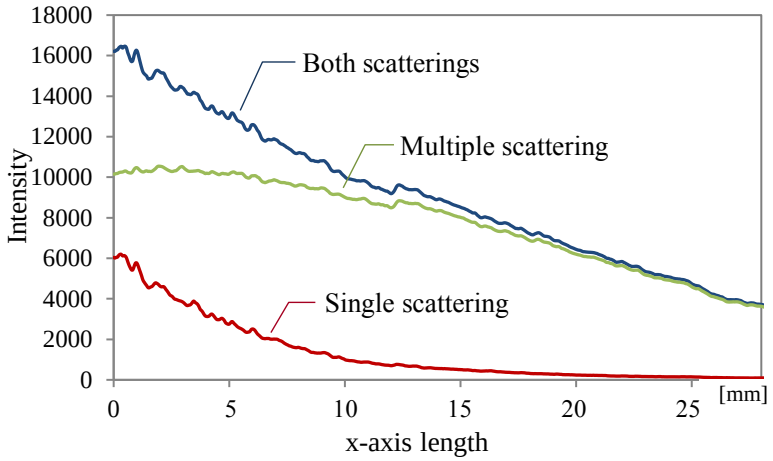

(b) Plot of scattering components

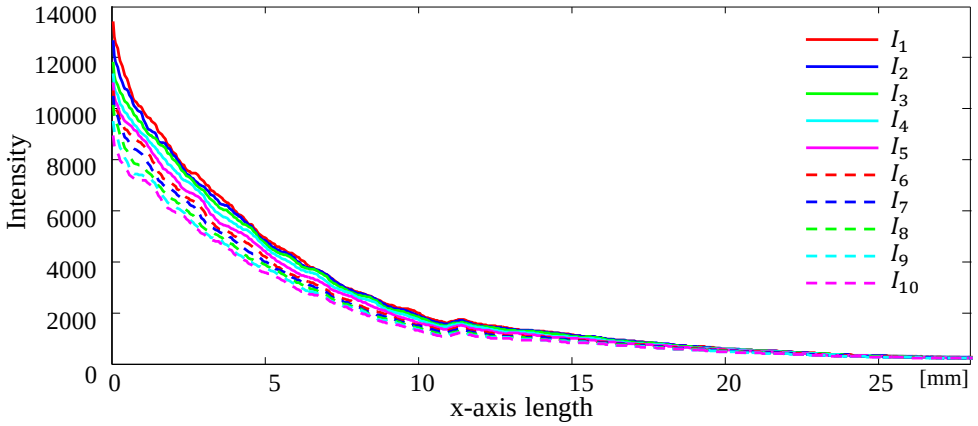

(c) Plot of single scatterings

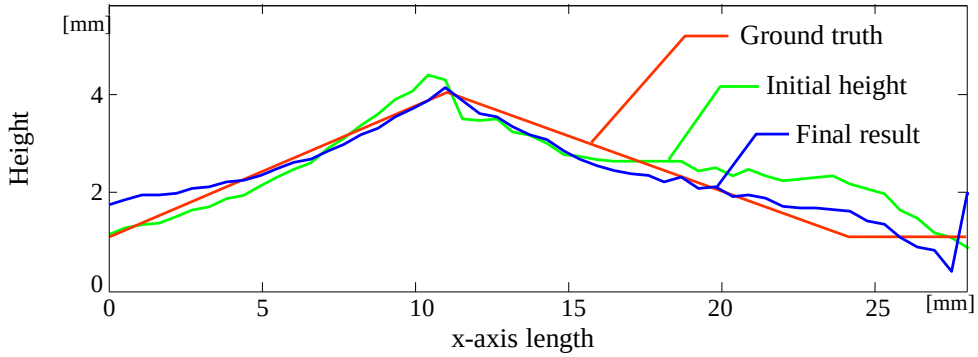

(d) Estimated shape

Figure 5.11: Experimental result for a convex scene.

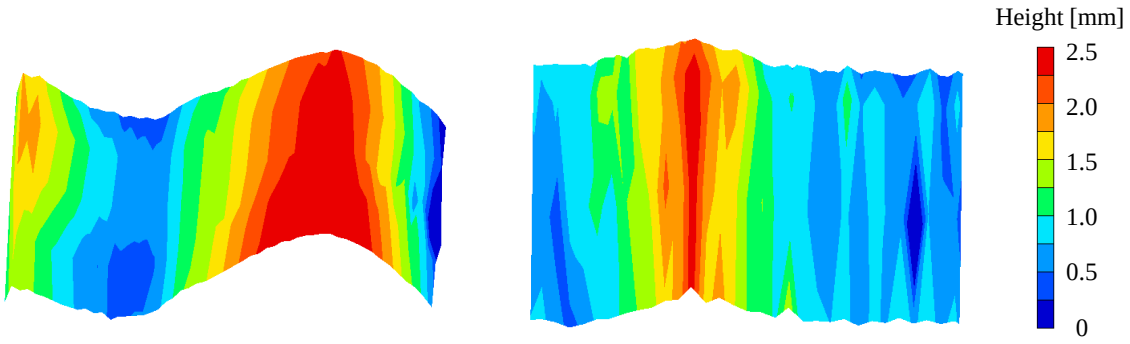

(a) Concave scene (b) Convex scene

Figure 5.12: Three-dimensional plots of estimated concave and convex scene.

intensities of single scattering, multiple scattering, and observed scattering, respectively. It is observed that single scattering is almost exponentially attenuated with increasing distance from the incident point. Figure 5.10(c) shows plots of extracted single scattering with for different heights of incident light. We estimate the target shape from these intensities. One-dimensional plots of estimation results are shown in Fig. 5.10(d). The red, green, and blue lines are the ground truth, initial height, and final result, respectively. The initial height is not very far from the ground truth. The final result is estimated as being close to the ground truth. However, the final result is estimated incorrectly in the region of a planar surface. A possible reason for the incorrect estimation is insufficient intensity of single scattering for shape estimation because the light paths are longer in observing this region. In addition, the shape near the incident plane does not match the ground truth well owing to the bright observation at the incident point and its glare. Scattering parameters are estimated as $s = 1.21 \times 10^4$, $g = 0.042$, and $\sigma = 0.132[\text{mm}^{-1}]$.

We also show the experimental result of the convex scene in Fig. 5.11. Figures 5.11(a) and (b) show the separated scattering component and intensity plot, respectively. Figure 5.11(d) is the shape estimated from single scatterings as shown in Fig. 5.11(c). Discontinuous shape at the top of the convex shape in the initial shape is improved to the correct shape in the final result. Estimated scattering parameters are $s = 1.27 \times 10^4$, $g = -0.083$, and $\sigma_t = 0.143[\text{mm}^{-1}]$. These parameters are similar to the concave case because the objects are made of the same materials.

We show the result of another convex scene in Fig. 5.13. Figure 5.13(c) shows the reconstruction result given by single scattering with illumination from the front of the target object. Because of the insufficient intensities of single scattering as shown in Fig. 5.13 (b), the estimated height has large error in the back area. To reduce the error, we capture the intensities

(a) Target object

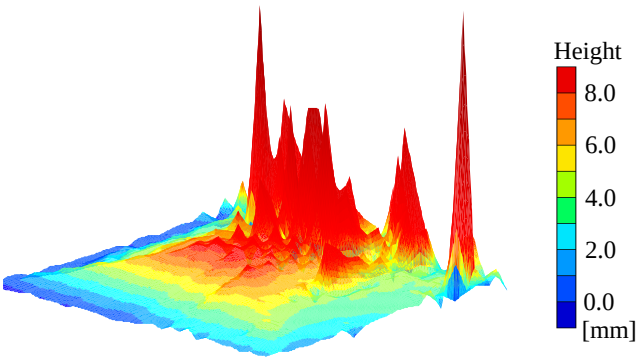

(c) Three-dimensional plot of the result with illumination only from one side of the object

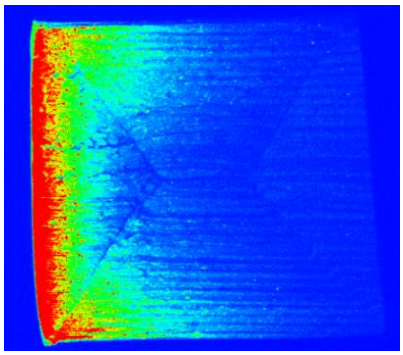

(b) Observed single scattering in pseudo color

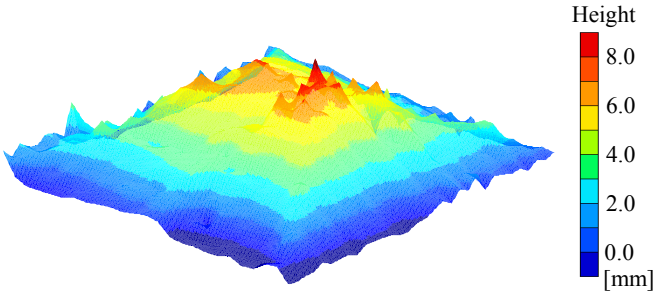

(d) Three-dimensional plot of the merged result

Figure 5.13: Experimental results for an asymmetric convex scene. (b) Observed single scattering in pseudo color. (c) Three-dimensional plot of the estimation result with illumination only from one side of the object. (d) Three-dimensional plot of the merged result.

of single scattering by illuminating from the other side of the target object, and then merge the two estimated reconstruction results. Figure 5.13(d) shows the merged result. Large noise is reduced and whole the shape is estimated. However, estimated surfaces are not planar due to artifacts in the decomposed single scattering as shown in Fig. 5.13 (b). This artifact is occurred by projected high-frequency stripe pattern. It remains difficulty on separation of scattering components with high accuracy.

5.4.3 Discussion

Computation time

In this experiment, it took about 15 minutes to capture images (six images for extracting single scattering at each of 10 different depths), and it takes a few hours to compute the shape with an unoptimized Matlab implementation. We computed estimates on an Intel Core 2 Duo central processing unit (3.00 GHz) with 3GB random access memory. The size of the problem is 74 (71 points for $h(x)$, s, g, and σ_t) in synthetic data, 259 (256 points for $h(x, y)$, s, g, and σ_t) in symmetric real data, and 873 (870 points for $h(x, y)$, s, g, and σ_t) in asymmetric real data.

Limitations

There are a few limitations to the current method. These limitations will be overcome in our future work.

Object shape: Our current formulation requires that the incident plane is planar and incident light on the target object is parallel to the x-axis for the extraction of single scattering using high-frequency projection. When projected patterns interfere with each other, single scattering cannot be extracted. This assumption needs to be relaxed when it is applied to a more general shape.

Single scattering in an inhomogeneous material: As our method uses single scattering, which exponentially attenuates with constant scattering parameters, we cannot estimate the shape of an inhomogeneous material. To deal with spatially varying scattering media, it is required to estimate scattering parameters in a three-dimensional volume. However, estimation of a huge number of unknown scattering parameters is a challenging task.

5.5 Summary

In this chapter, we proposed a method of estimating the shape of optically thin translucent objects based on the attenuation of single scattering. Because the light in optically thin translucent object is dominated by low-bounce scattering, the attenuation model of single scattering is appropriate for target objects in this chapter. We modeled the light attenuation in the object based on Lambert Beer's law and make relationship between the shape of target object and observed intensities of single scattering. Experiments with synthetic and real-world results demonstrated that our method has the potential for the accurate modeling of translucent objects, which has been difficult to achieve with other appearance-based methods. While the method works well for various translucent objects, the accuracy suffers from low-intensity measurements and a

high signal-to-noise ratio when measuring optically thick objects, for which multiple scattering dominates the appearance. In addition, the accuracy of shape estimation depends on quality of extracting single scattering by high-frequency illumination. Another issue relating to the current approach is the high computational cost. We are interested in looking into these aspects further to make the approach more practical.

Chapter 6

Shape Estimation of an Optically Thick Translucent Objects

6.1 Introduction

The shape of the optically thin translucent object is estimated from single scattering, which is attenuated light along the refracted light. Refracted light is useful in reconstructing the object shape because it depends directly on the surface direction. By contrast, in optically thick translucent objects, incident light does not propagate along the refractive direction, but rather distributes around the incident point owing to uncountable collisions with particles in the medium as described in Section 4.3. As a result, we cannot observe refractive transmitted light in the medium but rather obtain shading of the target object.

Observed shadings are often used to estimate surface normals, which represent the direction of the object surface, in a photometric stereo technique [28]. The photometric stereo technique is known as a method of estimating object shape from multiple shading images in the field of computer vision. While conventional photometric stereo methods have been developed for simple Lambertian diffuse surfaces [76], recent generalizations can handle more complex reflections in real-world scenes [109, 110]. However, the estimation of the surface normals of translucent materials remains a difficult task, with subsurface scattering being significant [111].

While the exact modeling of subsurface scattering remains a difficult task that requires complicated models, prior studies in the field of computer graphics show that the image formation model of subsurface scattering can be well approximated as the convolution of the scattering kernel and surface radiance of optically thick materials, which distribute light regardless of the incident direction [95]. In Chapter 4, we show that light transport in an optically thick translucent medium does not depend on the directions of the incident and outgoing light. Hence, we use this approximation to develop *surface normal deconvolution*, which recovers the original

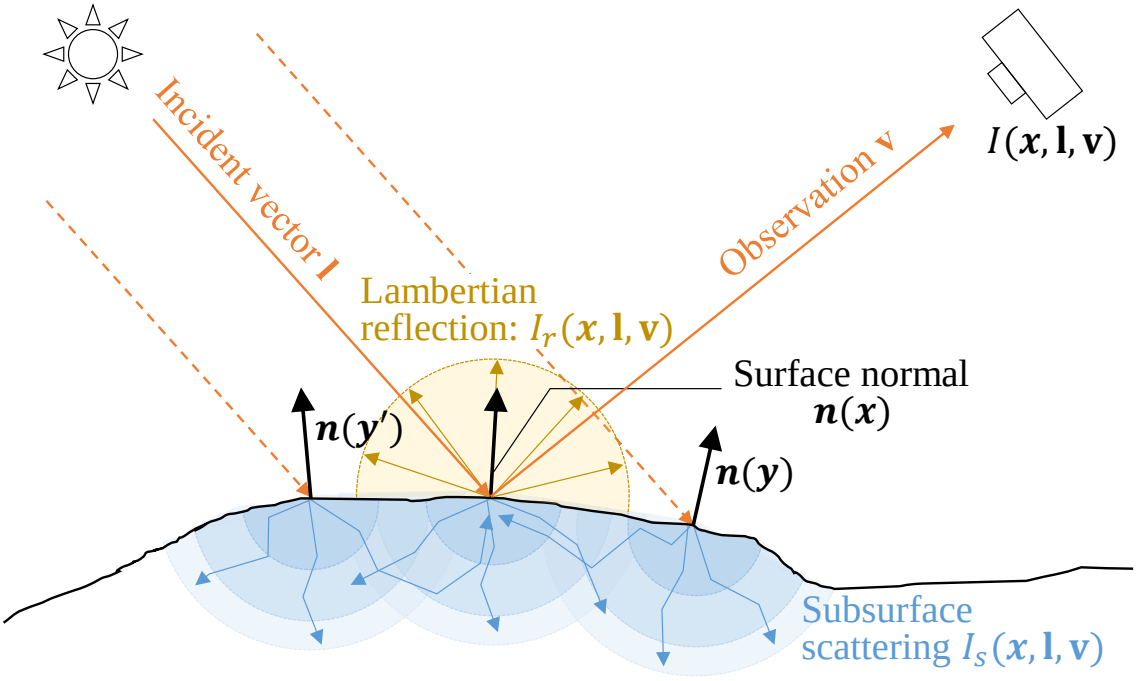

Figure 6.1: Light interactions on a translucent surface. Incident light is partially reflected from the surface, while the remaining light transmits and spreads inside the subsurface.

surface normal from the *blurry* surface normal obtained by applying the conventional photometric stereo method to translucent objects. This idea is similar to Dong *et al.*'s method [112], which estimates the surface normal using deconvolved input images to remove the subsurface scattering effect. While Dong *et al.* assumed parametric subsurface scattering (*i.e.*, photon beam diffusion of optically homogeneous media), we represent subsurface scattering by non-parametric convolution kernels for either optically homogeneous or inhomogeneous media. The convolution kernels can be either calibrated or estimated, and various deconvolution techniques in the literature (such as image deblurring methods) can be used in the implementation to recover the deblurred surface normal. We present estimation results obtained using our deconvolution formulation and using existing deconvolution in experiments.

6.2 Convolutional Image Formation Model

We begin with the image formation model for a translucent surface. When light illuminates a translucent surface, it is reflected, transmitted and absorbed as depicted in Fig. 6.1. A portion of the transmitted light returns to the surface via subsurface scattering; thus, the radiance $I(x, \mathbf{l}, \mathbf{v})$ at a scene point x with incident vector $\mathbf{l}$ and observation vector $\mathbf{v}$ becomes the sum of the

reflection $I_r(x, \mathbf{l}, \mathbf{v})$ and subsurface scattering $I_s(x, \mathbf{l}, \mathbf{v})$ components:

$$I(x, \mathbf{l}, \mathbf{v}) = I_r(x, \mathbf{l}, \mathbf{v}) + I_s(x, \mathbf{l}, \mathbf{v}). \tag{6.1}$$

The subsurface scattering component $I_s(x, \mathbf{l}, \mathbf{v})$ is modeled as [26]

$$I_s(x, \mathbf{l}, \mathbf{v}) = \gamma(x)\ F(\mathbf{v}, \mathbf{n}(x), \eta) \int_{y \in A} R(x, y) F(\mathbf{l}, \mathbf{n}(y), \eta) \mathbf{n}(y)^T \mathbf{l} dy, \tag{6.2}$$

where $\gamma(x)$ is a scale factor for the subsurface scattering component, F represents Fresnel transmission, and $\mathbf{v}, \mathbf{n}, \mathbf{l} \in \mathbb{R}^3$ are the observation, surface normal, and incident vectors, respectively. η is a refractive index, $R(x, y)$ represents an extinction term for light traveling from scene point x to its neighbor y such as a dipole model [26], and A defines a neighboring area. Generally, the subsurface scattering component describes a nonlinear relation between the surface normal and observed intensity owing to the Fresnel transmission term. To relax this complexity, we approximate the original model as a simpler form by assuming an optically thick material, as in [113]. On the surface of an optically thick material, subsurface scattering does not depend on the direction of the light, because the transmitted light scatters uncountable times and loses its directionality due to random light paths as in the diffusion approximation. Thus, subsurface scattering is invariant to the incident direction and outgoing direction, and the Fresnel term F can be regarded as constant for an optically thick material. As a result, the subsurface scattering component $I_s(x, \mathbf{l}, \mathbf{v})$ is simplified as

$$I_s(x, \mathbf{l}) = \gamma'(x) \int_{y \in A} R(x, y) \mathbf{n}(y)^T \mathbf{l} dy, \tag{6.3}$$

where $\gamma'(x)$ is a new scale factor of subsurface scattering that includes constant Fresnel transmission terms.

Assuming a Lambertian reflectance model for the reflection component $I_r(x, \mathbf{l}) = \rho(x)\mathbf{n}(x)^T\mathbf{l}$ with a diffuse albedo $\rho(x)$, the intensity observation $I(x, \mathbf{l}, \mathbf{v})$ can be written as

$$I(x, \mathbf{l}) = \left(\rho(x)\mathbf{n}(x) + \gamma'(x) \int_{y \in A} R(x, y)\mathbf{n}(y) dy \right)^T \mathbf{l}. \tag{6.4}$$

The first factor of eq. (6.4) can be regarded as a simple convolution model as

$$I(x, \mathbf{l}) = \left(\int_{y \in A} h(x, y)\mathbf{n}(y) dy \right)^T \mathbf{l} = (h * \mathbf{n}(x))^T \mathbf{l}, \tag{6.5}$$

where $*$ is the convolution operation, and the kernel h represents a scattering effect for the surface normals and is expressed as

$$h(x, y) = \rho(x)\delta(x - y) + \gamma'(x)R(x, y). \tag{6.6}$$

The kernel h expresses the spatial attenuation of scattering from incident point on the object surface.

A similar convolutional approximation of subsurface scattering is also discussed in the work of Munoz *et al*. [113] for the forward rendering of optically thick materials. This method is inspired by the works of convolutional approximated subsurface scattering by d'Eon *et al*. [114] for the rendering of human skin and Donner *et al*. [25] for multi-layered materials. Unlike their method, where the extinction term $R(x, y)$ is defined as a function parameterized only by the relative positions of x and y, our method allows more flexibility for the extinction term $R(x, y)$ so that inhomogeneous translucent materials can also be handled.

6.3 Solution method

6.3.1 Surface normal obtained by the conventional photometric stereo method

Based on the convolutional image formation model, we develop a photometric stereo method for estimating the surface normals of an optically thick translucent surface. Our input is the same as that of the traditional photometric stereo method in that a set of images is taken under varying lighting directions from a fixed viewpoint. To simplify the discussion, we assume that the light directions are calibrated and the observations do not include shadows. In the rest of the paper, we consider the discretized pixel sites u and v that correspond to scene points x and y, respectively; thus, eq. (6.5) becomes

$$I(u, \mathbf{l}) = \left(h(u, v) * \mathbf{n}(u)\right)^T \mathbf{l}. \tag{6.7}$$

The convolution equation eq. (6.7) has the simple linear algebraic expression

$$\mathbf{D} = \mathbf{HNL}, \tag{6.8}$$

where $\mathbf{D} \in \mathbb{R}^{m\times k}$ is an observation matrix, m and k are the numbers of pixels and light directions, respectively, $\mathbf{H} \in \mathbb{R}^{m\times m}$ is a scattering matrix, $\mathbf{N} \in \mathbb{R}^{m\times 3}$ is a surface normal matrix,

and $\mathbf{L} \in \mathbb{R}^{3\times k}$ is an incident light matrix, which is assumed to be known. This linear expression indeed has similarity to the expression of the Lambertian photometric stereo method [28], where the observation $\mathbf{D}$, scaled surface normal $\mathbf{N}_s$, and light matrix $\mathbf{L}$ have the relationship

$$\mathbf{D} = \mathbf{N}_s\mathbf{L}. \tag{6.9}$$

From Eqs. (6.8) and (6.9), we see that the scaled surface normal $\mathbf{N}_s$ corresponds to $\mathbf{HN}$ according to

$$\mathbf{N}_s = \mathbf{HN}. \tag{6.10}$$

Therefore, we can regard the scaled surface normal $\mathbf{N}_s$ as a *blurry* version of the original surface normal $\mathbf{N}$ that we wish to estimate. In the following, we call $\mathbf{N}_s$ a smoothed surface normal.

6.3.2 Estimation process

According to the observation in the previous section, we estimate the surface normal $\mathbf{N}$ by taking the following two-step approach. (a) Obtain the smoothed surface normal $\mathbf{N}_s$ by Lambertian photometric stereo [28], (b) Estimate the surface normal $\mathbf{N}$ in a deconvolution framework using the subsurface scattering matrix $\mathbf{H}$.

(a) Estimation of the smoothed surface normal $\mathbf{N}_s$. We use a conventional Lambertian photometric stereo method [28] to derive the smoothed surface normal $\mathbf{N}_s$ as

$$\mathbf{N}_s = \mathbf{DL}^{\dagger}, \tag{6.11}$$

where † represents a Moore-Penrose pseudo inverse.

(b) Estimation of the original surface normal $\mathbf{N}$. Once the smoothed surface normal $\mathbf{N}_s$ is obtained, we use eq. (6.10) to derive the original surface normal $\mathbf{N}$. If the scattering matrix $\mathbf{H}$ is available and invertible, we can directly obtain the estimate of the original surface normal $\mathbf{N}$ in a linear least-squares fashion as $\mathbf{N} = \mathbf{H}^{-1}\mathbf{N}_s$. As the estimation result produced by such simple deconvolution is often degraded by ringing artifacts owing to the loss of high-frequency information in the original signal, we use a smoothness constraint to stabilize the estimation. We design the smoothness term s as a weighted second-order difference of $\mathbf{n}(u)$ between u's neighborhood locations t and v as

$$\mathbf{n}''(u) = w(t,u)\left(\mathbf{n}(t) - \mathbf{n}(u)\right) - w(u,v)\left(\mathbf{n}(u) - \mathbf{n}(v)\right). \tag{6.12}$$

The weight $w(u,v)$ controls the discontinuity of surface normals by taking the difference of intensity observations across varying lightings $\mathbf{l}_i$ as

$$w(u,v) = \exp\left(-\frac{1}{m}\sum_{i}^{k}\left(I(u,\mathbf{l}_i) - I(v,\mathbf{l}_i)\right)^2\right). \tag{6.13}$$

The matrix expression of the smoothness $\mathbf{N}''$ is given as

$$\mathbf{N}'' = \mathbf{W}\mathbf{N}, \tag{6.14}$$

where $\mathbf{W} \in \mathbb{R}^{a\times m}$ is a matrix of the second-order derivative filter, and a is the number of triplets used to compute the second-order derivatives. In our case, we define the triplets along horizontal and vertical directions in the image coordinates. Finally, our estimation problem becomes a ridge regression problem expressed as

$$\hat{\mathbf{N}} \;=\; \underset{\mathbf{N}}{\operatorname{argmin}}\, ||\mathbf{H}\mathbf{N} - \mathbf{N}_\mathbf{s}||_F^2 + \lambda||\mathbf{W}\mathbf{N}||_F^2, \tag{6.15}$$

where λ controls the smoothness of the estimates. An explicit solution to this problem is given by setting the first-order derivative to zero as expressed by

$$\mathbf{N} = \left(\mathbf{H}^T\mathbf{H} + \lambda\mathbf{W}^T\mathbf{W}\right)^{-1}\mathbf{H}^T\mathbf{N}_\mathbf{s}. \tag{6.16}$$

In this manner, the estimates for the original surface normal $\mathbf{N}$ can be obtained in a closed-form.

The mathematical expression of the problem is equivalent to that of the image deblurring problem, where the original sharp image is recovered via deconvolution. The important difference, however, is that our problem deals with the deconvolution of surface normals. Therefore, conventional image priors that are developed for natural images may not be suitable. Other than this aspect, existing deconvolution techniques can be alternatively used to estimate the surface normal $\mathbf{N}$ from the smoothed surface normal $\mathbf{N}_s$. The convolution kernel $\mathbf{H}$ is generally unknown, but can be either calibrated (non-blind deconvolution) or estimated (blind deconvolution). While most image deblurring techniques are limited to spatially invariant point spread functions (PSFs), which corresponds to handling optically homogeneous materials in our case, the formulation of eq. (6.16) can naturally handle optically inhomogeneous materials, corresponding to the case of spatially-varying PSFs.

6.3.3 Calibration of the Convolution Kernel

As mentioned above, the surface normal deconvolution can be performed without knowing the convolution kernel using blind deconvolution techniques; however, knowledge of the convolution kernel is useful for stabilizing the estimation. In addition, spatially variant deconvolution is

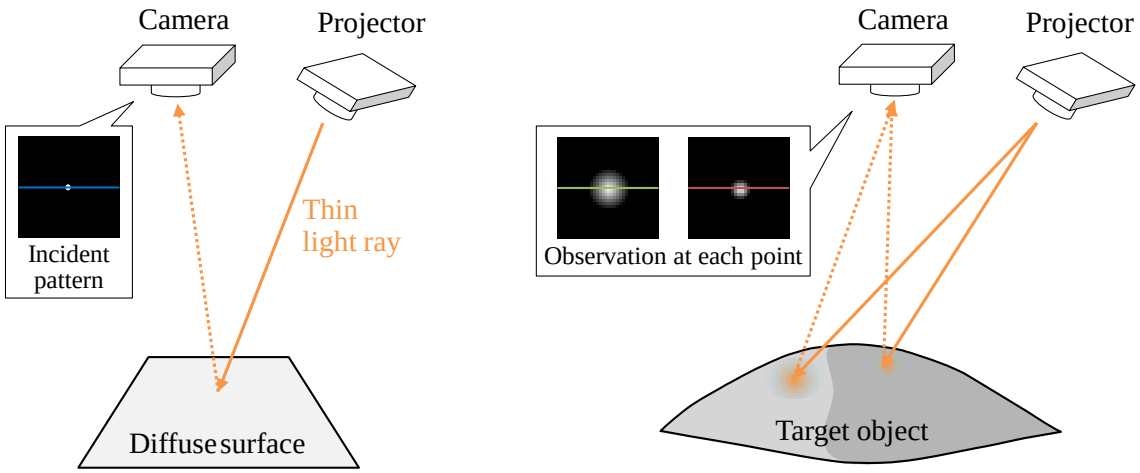

(a) Setting for measuring the convolution kernel

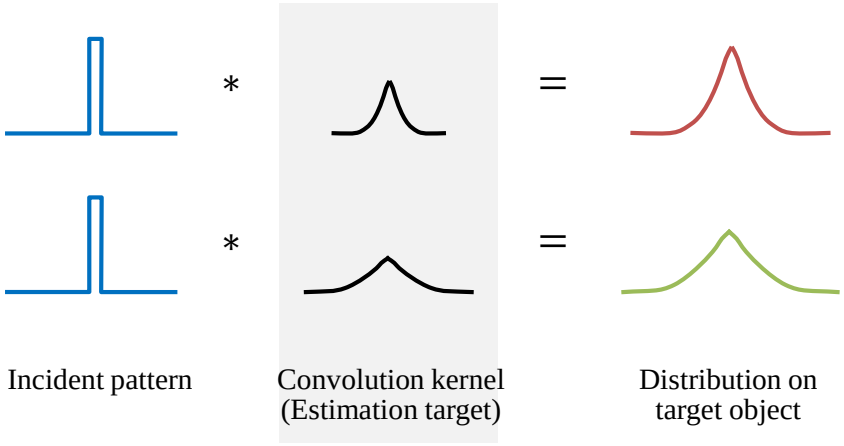

(b) Estimation of convolution kernel from captured distribution

Figure 6.2: Setting for measuring the convolution kernel. A projector casts a thin light ray on the target object. We estimate the convolution kernel from the incident pattern and light distributions on the target object. In the case of an inhomogeneous medium, we capture light distributions of optically different regions.

a challenging task in research on image deconvolution [115, 116]. Thus, we need to know convolution kernels at each position for dealing with optically inhomogeneous translucent objects. Here we describe a simple procedure for measuring the convolution kernel. Fig. 6.2 shows our setting for measuring the convolution kernel. By illuminating a diffuse surface and the target translucent material individually by a thin ray emitted from a projector, we obtain the measurements of the incident light distribution and scattering response on the surface, respectively. The measured scattering response corresponds to the convolution between the incident light

distribution and the convolution kernel. From this relationship, we calibrate the convolution kernel h which represents spatial attenuation of scattering. When the target medium is optically inhomogeneous, we need to calibrate the convolution kernel in each optically different region.

6.4 Experiments

We now evaluate our method using both synthetic and real-world data for the purposes of quantitative and qualitative evaluations.

6.4.1 Synthetic scenes

Homogeneous media

As the synthetic scene, we use the rough surface scene shown in Fig. 6.3. The image size is 160×160 pixels. To synthesize the input images under varying lightings, we use eq. (6.1) with the subsurface scattering model of eq. (6.2). For the extinction term $R(x, y)$ in eq. (6.2), we use the dipole model [26] with the same parameters described in their paper. The camera model is orthographic and the area of a pixel is $(4/15)^2[\mathrm{mm}^2]$.

Figure 6.3 (b) shows the result obtained using the Lambertian photometric stereo method based on eq. (6.11) and its angular error in pseudo color. Although the estimated surface normals are smoothed by subsurface scattering, especially around the edges, a low-frequency signal of the overall surface normal directions is largely obtained.

To apply our surface normal deconvolution of eq. (6.16), we use the extinction term $R(x, y)$ as the convolution kernel. The distance between scene points x and y is approximated as the distance between pixel sites u and v in the image coordinates. Figures 6.3 (c) and (d) show the results obtained using our method with smoothness factors of $\lambda = 0.01$ and $\lambda = 0.1$, respectively. While results with a small smoothness factor $\lambda = 0.01$ yield sharper reconstructions, they suffer from ringing artifacts around surface normal edges. Although the choice of a proper value for λ depends on the scene and is thus difficult as is the case for any regularization technique, with a proper value of λ, our method has notably better reconstruction accuracy than the Lambertian photometric stereo method that only considers the local illumination model, even though we assume the same Lambertian model as for the reflectance component. Table 6.1 summarizes the maximum and mean angular errors of the surface normal estimates made using various material parameters. In general, we observe that a smaller magnitude of subsurface scattering yields better accuracy, because stronger subsurface scattering cuts off the

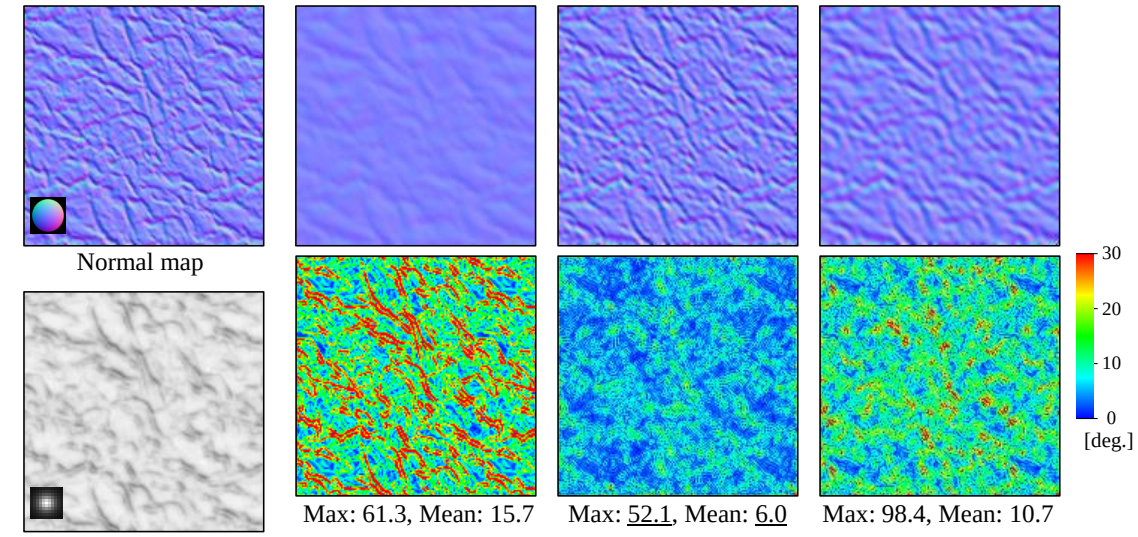

(a) Example of image and PSF for deconvolution

(b) Lambertian photometric stereo

(c) Our method $\lambda = 0.01$

(d) Our method $\lambda = 0.1$

Figure 6.3: Result for a synthetic rough scene. (a) Example of synthetic images obtained using the dipole model with the parameters for skim milk given in [26]. (b) Surface normal and error maps of the Lambertian photometric stereo method. More faithful surface normals are obtained using our method in (c) and (d) different smoothness factors λ.

Table 6.1: Maximum and mean angular errors [deg.] of scenes A and B for various materials. Parameters of each material are described in [26].

Plot of kernels 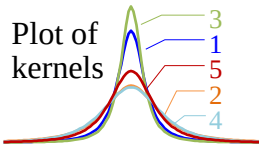	Lambertian PS		Our method $\lambda = 0.01$		Our method $\lambda = 0.1$	
	max	mean	max	mean	max	mean
1. Marble	56.2	11.9	29.1	1.9	36.2	5.6
2. Skim milk	61.3	15.7	52.1	6.0	98.4	10.7
3. Whole milk	52.4	10.7	22.1	1.5	28.5	4.4
4. Skin1	63.4	15.3	43.1	6.5	105.1	10.6
5. Skin2	61.5	14.3	47.9	4.2	86.2	8.7

high-frequency signals more notably. This shows that, by properly accounting for subsurface scattering, the accuracy is roughly $2 \sim 5$ times better than that of the baseline technique that only considers the local illumination model.

For optically homogeneous materials, we can also use conventional deconvolution methods in place of solving eq. (6.16). Figures 6.4 and 6.5 show the results of conventional non-blind deconvolution and blind deconvolution for scene B, respectively. For the non-blind deconvo-

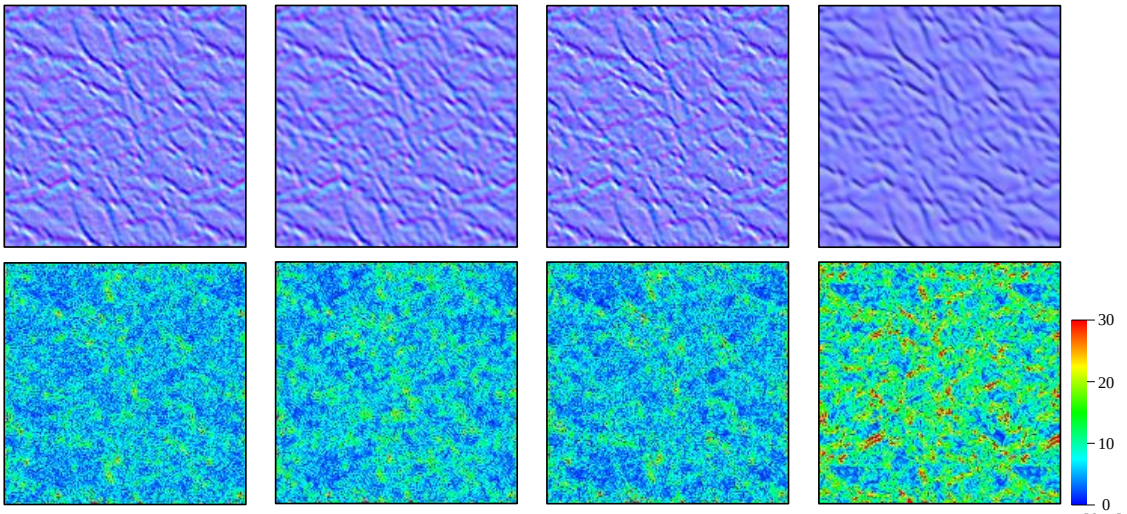

Max: 47.0, Mean: 6.4 | Max: 47.8, Mean: 6.9 | Max: 56.0, Mean: 6.8 | Max: 54.6, Mean: 11.0

(a) Wiener filter [117] (b) RichardsonLucy [118] (c) Cho *et al*. [119] (d) Dong *et al*. [120]

Figure 6.4: Surface normal estimates made using non-blind deconvolution methods

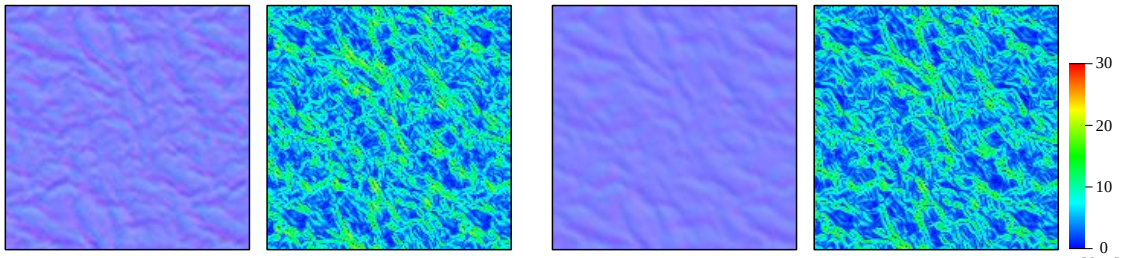

Max: 53.6, Mean: 9.1 | Max: 54.9, Mean: 11.5

(a) Levin *et al*. [121] (b) Krishnan *et al*. [122]

Figure 6.5: Surface normal estimates of scene B made using blind deconvolution methods

lution methods, we use the same convolution kernel as that used in producing the result of Fig. 6.3. The results show consistent improvement over the Lambertian photometric stereo method, although these original methods are not particularly designed to deblur surface normal fields. In addition, the results of blind deconvolution methods in Fig. 6.5, where the convolution kernel is not given but simultaneously estimated, also show improvement. While the blind deconvolution is a harder problem than non-blind deconvolution to solve and the results are generally worse, when knowledge of the convolution kernel is unavailable, it is a viable option for our method.

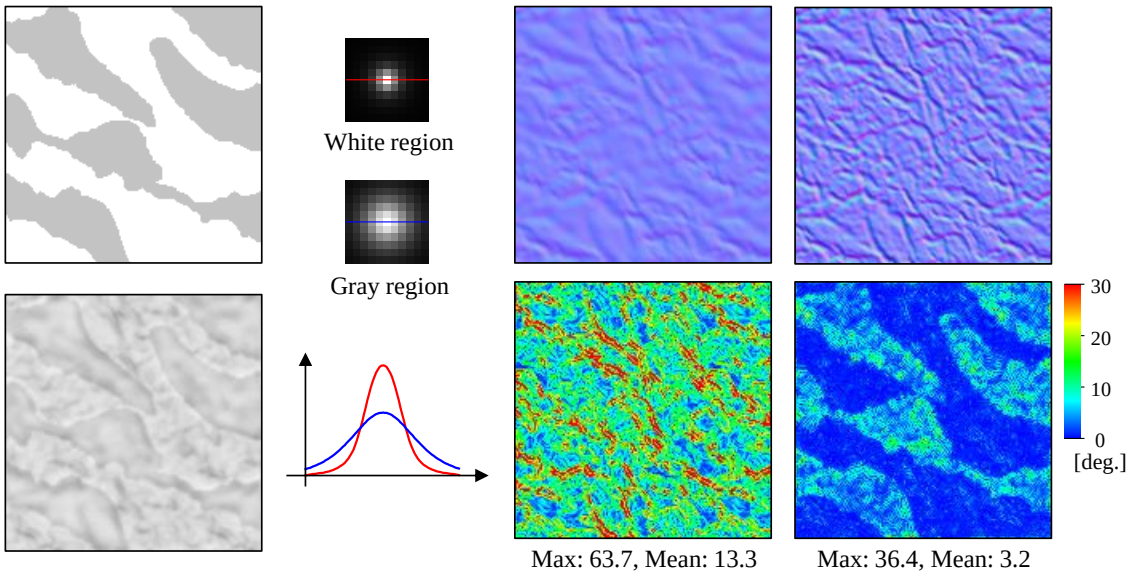

(a) Material region mask and synthesized image | (b) Kernel for each region | (c) Lambertian photometric stereo | (d) Our method

Figure 6.6: Results for a scene of an optically inhomogeneous medium using rough scene. (a) Masks indicating different material regions and synthesized images. (b) Two types of convolution kernels used for these distinct regions. (c) and (d) Smoothed surface normals obtained employing the Lambertian photometric stereo method and our results, respectively.

Inhomogeneous media

Our solution method is naturally applicable to the case of inhomogeneous materials, as long as the convolution kernel $\mathbf{H}$ in eq. (6.16) is defined. To evaluate the performance of our method for inhomogeneous materials, we produce synthetic images that contain different optical thicknesses using masks that indicate the material regions as shown in Fig. 6.6 (a) and (b). Because of the difference in the magnitudes of subsurface scattering in the material regions, the surface normal estimates obtained using the Lambertian photometric stereo method, shown in Fig. 6.6 (c), exhibit varying smoothnesses; smoother in the gray mask region, and sharper in the white mask region.

By applying our method, the surface normal field is consistently improved regardless of the material regions as shown in the Fig. 6.6 (d). This recovery is more accurate than that of Fig. 6.3, because the inhomogeneous example contains a region where there is less scattering. Estimated normals in the gray mask region are less accurate than normals in the white mask because deconvolution of a strong blur effect is more difficult than a weak blur effect.

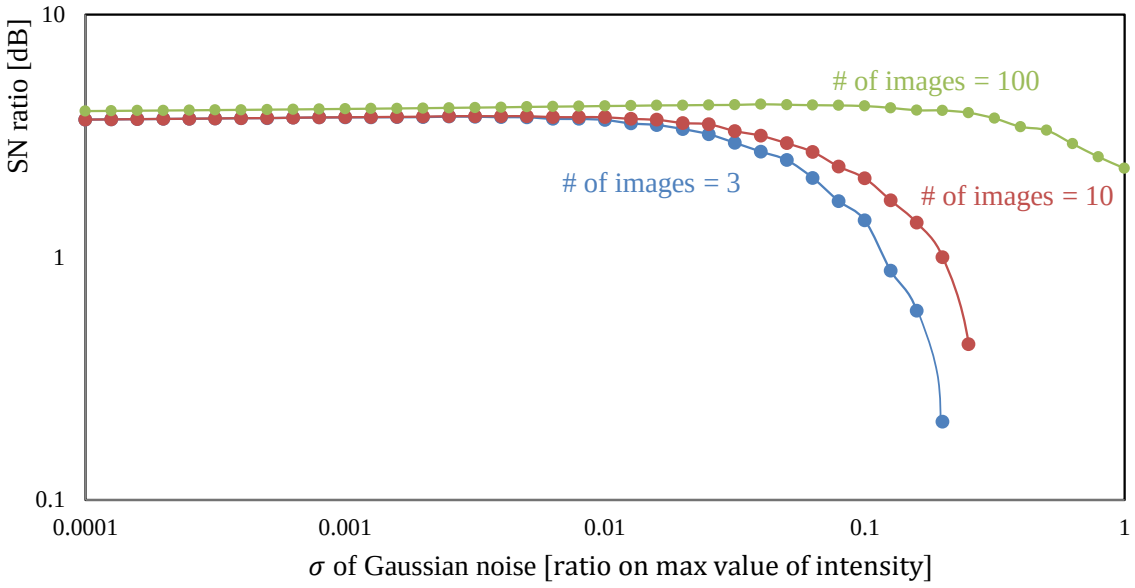

Figure 6.7: RMSE of estimated surface normals at each noise level

Robustness of estimation results against observation noise

We evaluate the robustness of our method against observation noise in the rough scene. The optical parameters are set to those of skim milk as described in [26]. We add Gaussian noise to the synthesized intensity at various levels ($\mu = 0$ and $\sigma = [0.0001, 1] \times I_{max}$, I_{max} is the maximum value of the synthesized intensity). We also change the number of input synthesized images as 3, 10, and 100. Figure 6.7 plots the RMSE of estimated normals against the noise level. The blue, red, and green lines are the results for 3, 10 and 100 input images, respectively. The RMSE is constant at a low σ level but gradually decreases as σ increases. For 14-bit raw data, the RMSE decreases at $\sigma = 0.1 \times I_{max} = 163.8$ and $\sigma = 0.01 \times I_{max} = 16.3$ with 100 and 10 input images, respectively. These conditions are closer to a commercial camera. If a camera captures noisy data, we can reduce errors in the estimated surface normals owing to observation noise by increasing the number of input images.

6.4.2 Real-world scenes

We also tested our method using real-world translucent objects. Figure 6.8 (a) shows our experiment setting. We used a Nikon D90 camera with a linear radiometric response function (RAW mode) and a telescopic lens to approximate an orthographic projection. We used a 3M MP220 projector to provide illumination. The target scenes are illuminated under directional lighting, and the light directions are calibrated using a dark specular sphere. In addition, to

avoid specular reflections from the scene, we placed polarizers in front of both the light source and camera. We used three target objects: a bar of soap as a homogeneous medium and angel and unicorn ornaments as inhomogeneous media, as shown in Fig. 6.8 (b). Each scene was recorded for 12 different lighting directions. The image sizes of the soap, angel, and unicorn scenes were 232×164, 206×257, and 158×230 pixels, respectively. Prior to the measurement, the convolution kernels were measured using the procedure described in Section 6.3.3. For the inhomogeneous objects, we measured two distinct kernels for the different material regions, one for a white region and the other for a pink region.

Figure 6.9 shows the experimental results for the soap. The recorded intensity image is not notably blurry, but the details are smoothed by subsurface scattering as shown in Fig. 6.9 (a). The observed PSF shows incident light distributed on the surface of the soap. Fig. 6.9 (b) shows the surface normals estimated using the Lambertian photometric stereo method [28], our method, and Gu *et al*.'s method [123]. Gu *et al*.'s method estimates surface normals from images in which scattering effects are reduced by high-frequency sinusoidal projection. We used a projector to control the projection pattern, and decomposed the direct reflection images as shown in Fig. 6.9. While the result of the Lambertian photometric stereo method shows smoothed surface normals, our result is sharper. Even though the decomposed direct image has moderate wave artifacts throughout, Gu *et al*.'s method shows surface normals on a fine scale. We also reconstruct the surface shape from normals estimated using Agrawal *et al*.'s method[124] as shown in Fig. 6.9 (c). We recognize that detailed shapes can be estimated from the normals of our method and Gu *et al*.'s method.

Figures 6.10 and 6.11 show experimental results for the angel and unicorn, respectively. Observed PSFs have different light distributions for the different materials as shown in Figures 6.10 and 6.11 (a). Although the observed image is blurred compared with decomposed direct image, our method estimates sharper surface normals by reducing scattering effects. Gu *et al*.'s method also estimates sharp surface normals. However, the reconstructed shape has noise in the planar region because of wave artifacts on the decomposed direct image. Subsurface scattering components can be reduced by high-frequency sinusoidal projection. Nevertheless, it is difficult to completely avoid artifacts in the decomposed image using a projection pattern.

6.4.3 Discussion

Computation time.

The above experiments show that, in the case of optically homogeneous materials, we can apply various fast deconvolution methods for image deblurring to recover the surface normal.

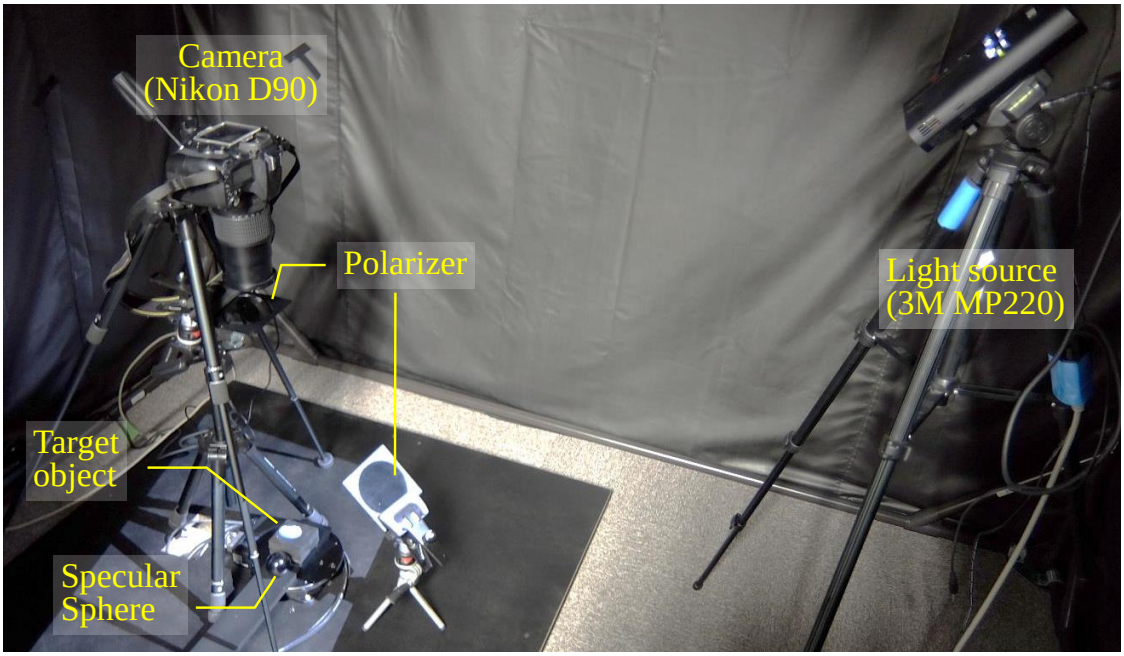

(a) Experiment setting

Soap

Angel

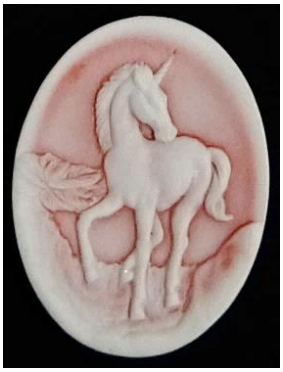

Unicorn

(b) Target objects

Figure 6.8: Experiment setting and target objects. We used a projector as a light source. The camera was equipped with a telescopic lens. Polarizers were used to reduce the effects of specular reflection on the target object.

However, in the case of inhomogeneous media, we have to solve eq. (6.16) to deal with spatially variant convolution kernels. Our Matlab implementation on an Intel Core i7 central processing unit (3.5 GHz) takes about 17.6, 39, and 3.5 seconds to recover the surface of the soap, angel, and unicorn scenes, respectively. The density of non-zero elements of matrix $\mathbf{F}^T\mathbf{F} + \lambda\mathbf{W}^T\mathbf{W}$ in eq. (6.16) is about 2.5%. The computation time depends on the size and number of non-zero

(a) Example of measured image and observed PSF

Lambertian photometric stereo

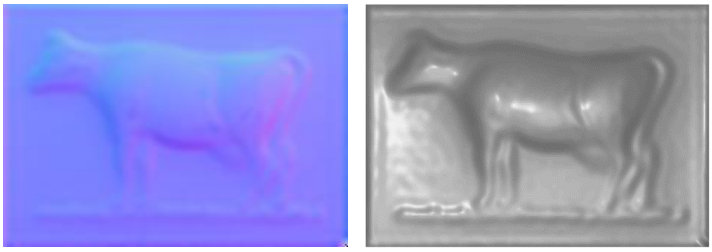

Our method

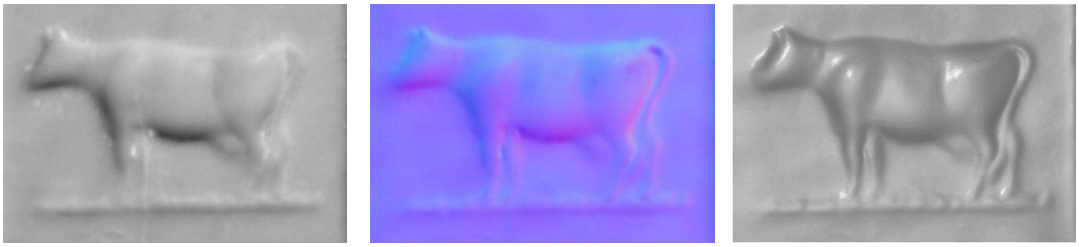

Decomposed direct image

Gu et al.'s method

(b) Estimated surface normals

(c) Reconstructed shape from surface normals

Figure 6.9: Result for a real-world scene of soap as a homogeneous medium. The direct image is calculated using Gu *et al.*'s method[123], and shapes are reconstructed using Agrawal *et al.*'s method [124].

elements of matrix $\mathbf{F}^T\mathbf{F}+\lambda\mathbf{W}^T\mathbf{W}$, which are determined by the input image size and apparent sizes of PSFs in the image coordinates.

Limitations.

Our method has a couple of limitations. First, we have ignored the effect of Fresnel transmissions. Thus, our method is restricted to optically thick materials. As a material has directional scattering, the accuracy of our method may gradually decrease. We are interested in exploring an iterative estimation framework that can be used to adaptively update the convolution kernels for the incorporation of the Fresnel transmission effects. The second limitation is that

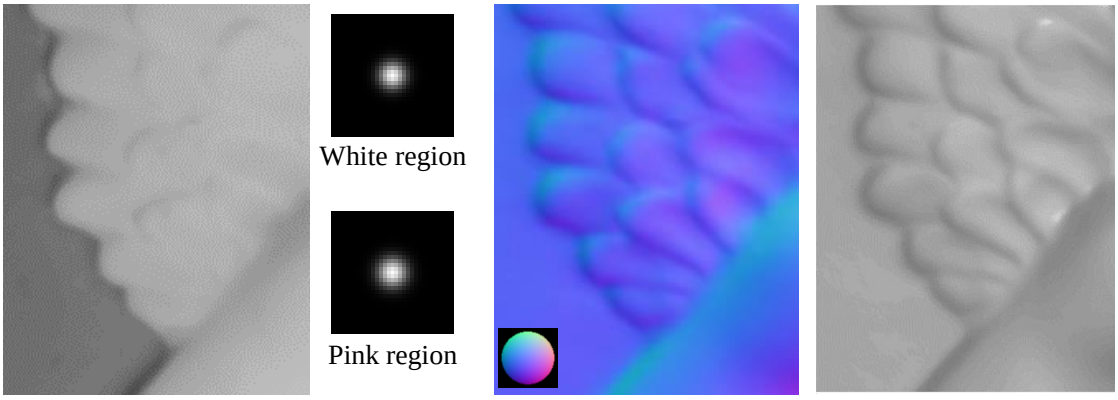

(a) Example of measured image and observed PSF

Lambertian photometric stereo

Our method

Decomposed direct image

Gu et al.'s method

(b) Estimated surface normals

(c) Reconstructed shape from surface normals

Figure 6.10: Result for a real-world scene of an angel ornament as an inhomogeneous medium.

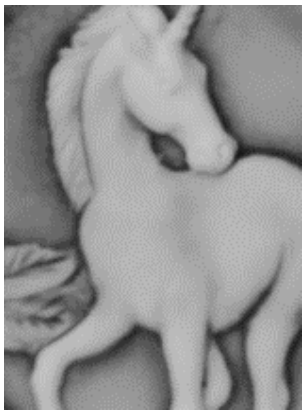

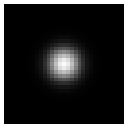

White region

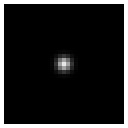

Pink region

(a) Example of measured image and observed PSF

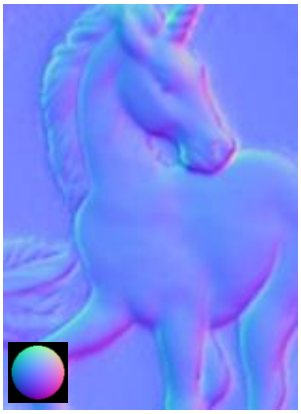

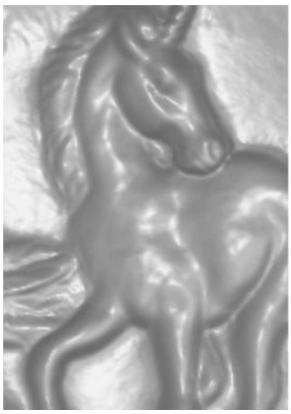

Lambertian photometric stereo

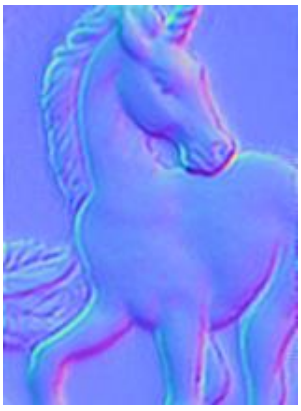

Our method

Decomposed direct image

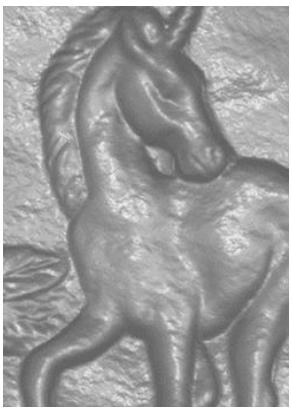

Gu et al.'s method

(b) Estimated surface normals

(c) Reconstructed shape from surface normals

Figure 6.11: Result for a real-world scene of a unicorn ornament as an inhomogeneous medium.

our method in practice relies on known convolution kernels, especially when dealing with optically inhomogeneous materials. Although a sophisticated blind deconvolution method may resolve this issue, at this point, knowledge of the convolution kernel plays an important role in obtaining accurate surface normal estimates. We are interested in investigating good prior information for surface normal fields that may potentially improve the blind deconvolution.

6.5 Summary

In this chapter, we proposed a shape estimation method for optically thick translucent objects. As optically thick translucent objects show shading on their surfaces, we estimate surface normals as the object shape from observed images employing the photometric stereo method. We extended the previous study on the convolutional approximation of subsurface scattering and developed a surface normal deconvolution technique, which consists of a conventional photometric stereo method and image deconvolution. Our experiment shows that the surface normals of translucent objects are reliably estimated by our method. As illustrated in the experiment section, our method can benefit from a large body of image deblurring methods in the literature, including blind deconvolution methods. In addition, we showed that our method is able to deal with optically inhomogeneous media.

Chapter 7

Summary and Discussions

In this thesis, we proposed methods of estimating the shape of translucent objects from observed scattering light according to light transport analysis. Scattering in translucent media adversely affects shape measurement because it prevents reference to the incident points of the laser range finder [4] and notably affects the object appearance as shown in Fig. 1.2. While most existing methods extract the scattering effect and thus ignore complex phenomena, scattering is not completely reduced owing to the degree of the spatial distribution [18]. Our *shape from scattering* framework tackles these problems by obtaining the object shape from the observed scattering effect itself. The key concept is how to model the relationship between the observed scattering effect and shape of the target object. Scattering observations depend not only on the target shape but also on the optical characteristics of the medium. Hence, we developed an approximation model of subsurface scattering according to the analysis of light transport in a real translucent medium.

First, we measured light transport in real translucent objects as described in Chapter 4. We used the *Turtleback Reflector* to distribute virtual illuminations and observations around the target scene, and captured the light transport as the eight-dimensional BSSRDF that is parameterized by the directions and positions of incident and outgoing light. The captured BSSRDF was visualized as a distribution around the outgoing direction at each outgoing point with fixed illumination for the analysis of the behavior of light transport. We also decomposed the BSSRDF into directional and nondirectional components by analyzing the BSSRDF along outgoing directions. As a result, we obtained the characteristics of the response of the BSSRDF to optical properties such as the directional light in an optically thin translucent medium, directionally invariant light in optically thick translucent objects, spatially invariant light in a homogeneous medium, and spatially varying light in an inhomogeneous medium. While reflection analysis of the outgoing direction is conducted using the four-dimensional BRDF, spatial analysis of light transport is available using the eight-dimensional BSSRDF.

According to the discussion in Chapter 4, we constructed shape estimation methods for translucent objects. We related scattering observations and object shape with optical parameters, and estimated the object shape from observations. For optically thin translucent objects, we used the attenuation model of single scattering to represent the directional light distribution around the refracted light in the medium. We formulated single scattering observed the experimental setting as a function of object shape, and estimated object shape by minimizing an energy function, which evaluates the difference between observed and synthesized intensities. We evaluated the estimation accuracy using synthetic data, and showed the availability of our method when single scattering inputs are sufficiently bright. Although the observation of a real translucent object includes varied types of scattering, we applied our estimation method to extract single scattering. The method simultaneously estimates the scattering parameters and target shape assuming an optically homogeneous translucent object. For optically thick translucent objects, we approximate non-directional scattering in the convolution model. This models not the direct relationship between the observed intensity and surface shape but the observed intensity and surface normals, which represent the direction of the object surface. Although the object shape needs to be reconstructed from the estimated normals, the convolution model provides a simple estimation process using a deconvolution algorithm. While we need to calibrate the scattering distribution on the target surface of each material, we can handle optically inhomogeneous media. Experiments employing synthetic and real scenes were conducted to evaluate the effectiveness of deconvolution-based scattering reduction in our method.

Our proposal of the *shape from scattering* framework allows us to estimate a translucent shape from observed scattering itself without complicated light transport analysis. *Shape from scattering* extends shape estimation to a variety of targets having translucent appearance. Such extension could benefit a wide range of applications in the field of computer vision that require shape information; *e.g.*, the automatic visual inspection of industrial products and the archiving of artistic sculptures, where translucent objects are made of plastic, marble, and wax. Meanwhile, our framework can also be used in the application of medical imaging because target organs have strong scattering properties. On the microscope scale, the main application of our method would be cell imaging.

We still face the problem that our method works on only translucent objects whose scatterings are modeled as the attenuation of single scattering or non-directional multiple scattering. In particular, while we extracted single scattering component from scatterings in optically thin translucent objects, the single scattering does not always become a main component in scattering. In optically thin materials, low-bounce scatterings such as two and three-bounce

scattering are also a main scattering component. Thus, even if the target object is relatively optically thin translucent, there is a possibility that extracted single scattering is insufficient intensity for shape estimation. The spatial optical properties of targets are also limited in both proposed shape estimation. In the method for optically thin translucent objects, we assume the spatially homogeneous material. This constraint allows us to estimate optical parameters such as extinction coefficient, however, we cannot apply this shape estimation method to optically inhomogeneous translucent object. On the other hand, in the method for optically thick translucent objects, we can handle optically inhomogeneous objects, but advancely calibrated scattering kernels at each point on the object surface are needed. Simultaneous estimating the object shape and optical parameters of optically inhomogeneous material is the most difficult problem setting.

The ultimate solution to deal with any type of translucency is a brute-force search via the simulation of light propagation in arbitrary translucent media without any parametric scattering models. However, it is an ill-posed problem to estimate spatially distributed optical properties and the object shape from a two-dimensional observed image in real time because a search range of an enormous number of unknowns is too huge to obtain an optimal solution. A conventional camera obtains only two-dimensional information, whereas recently developed advanced cameras can obtain richer information; *e.g.*, the light field camera [125] and ultrafast imaging camera [126, 127]. The light field camera [125] can store directions of incoming light from a scene, and the captured data then give the directional information of propagating light. Because the information of directionality relates to the directional distribution on BSSRDFs of a target object, the light field camera imaging helps to shrink the search range of shape estimation. Ultrafast imaging [126, 127] observes the temporal sequence of light propagation at a trillion frames per second. Since this ultrafast speed competes with the speed of light, we see the process of the light propagation from the captured image sequence. In the field of computer graphics, realistic image is rendered by simulating the propagation of light rays. Therefore, temporal image sequence becomes a clue for inversely rendering of target scene. This rich information will allow us to analyze light transport and make it possible to obtain the shape of a general translucent material in the future.

Our *shape from scattering* framework contributes technique of photometric analysis in the field of computer vision in the terms of using scattering light for obtaining object shape.

Reference

[1] F. Blais, “Review of 20 Years of Range Sensor Development,” *Journal of Electronic Imaging*, vol. 13, pp. 231–240, 2004.

[2] G. Sansoni, M. Trebeschi, and F. Docchio, “State-of-the-art and applications of 3d imaging sensors in industry, cultural heritage, medicine, and criminal investigation,” *Sensors*, vol. 9, no. 1, pp. 568–601, 2009.

[3] P. R. Apeagyei, “Application of 3D body scanning technology to human measurement for clothing Fit,” 2010.

[4] G. Godin, M. Rioux, and J. A. Beraldin, “An assessment of laser range measurement on marble surfaces,” in *Conference on Optical 3D Measurement Techniques*, 2001.

[5] T. Chen, H. P. A. Lensch, C. Fuchs, and H. P. Seidel, “Polarization and phase-shifting for 3d scanning of translucent objects,” in *Proceedings of IEEE Conference on Computer Vision and Pattern Recognition (CVPR)*, 2007.

[6] M. P. Rowe, J. E. N. Pugh, J. S. Tyo, and N. Engheta, “Polarization-difference imaging: a biologically inspired technique for observation through scattering media.,” *Optics letters*, vol. 20, pp. 608–610, 1995.

[7] Y. Y. Schechner and N. Karpel, “Recovery of underwater visibility and structure by polarization analysis,” *IEEE Journal of Oceanic Engineering*, vol. 30, pp. 570–587, 2005.

[8] M. Gupta, “On controlling light transport in poor visibility environments,” in *Proceedings of IEEE Conference on Computer Vision and Pattern Recognition (CVPR)*, 2008.

[9] M. Goesele, H. P. A. Lensch, J. Lang, C. Fuchs, and H. P. Seidel, “Disco - acquisition of translucent objects,” in *Proceedings of ACM SIGGRAPH*, pp. 835–844, 2004.

[10] S. K. Nayar, G. Krishnan, M. D. Grossberg, and R. Raskar, "Fast separation of direct and global components of a scene using high frequency illumination," *Proceedings of ACM SIGGRAPH*, vol. 25, pp. 935–944, 2006.

[11] K. Tanaka, Y. Mukaigawa, Y. Matsushita, and Y. Yagi, "Descattering of transmissive observation using Parallel High-Frequency Illumination," in *Proceedings of IEEE International Conference on Computational Photography (ICCP)*, 2013.

[12] D. Reddy, R. Ramamoorthi, and B. Curless, "Frequency-space decomposition and acquisition of light transport under spatially varying illumination," in *Proceedings of European Conference on Computer Vision (ECCV)*, 2012.

[13] J. Kim, D. Lanman, Y. Mukaigawa, and R. Raskar, "Descattering transmission via angular filtering," in *Proceedings of European Conference on Computer Vision (ECCV)*, pp. 86–99, 2010.

[14] M. Gupta, A. Agrawal, A. Veeraraghavan, and S. G. Narasimhan, "Structured light 3d scanning in the presence of global illumination," in *Proceedings of IEEE Conference on Computer Vision and Pattern Recognition (CVPR)*, 2011.

[15] M. Gupta and S. K. Nayar, "Micro phase shifting," in *Proceedings of IEEE Conference on Computer Vision and Pattern Recognition (CVPR)*, 2012.

[16] M. Gupta, A. Agrawal, A. Veeraraghavan, and S. G. Narasimhan, "A practical approach to 3d scanning in the presence of interreflections, subsurface scattering and defocus," *International Journal of Computer Vision (IJCV)*, vol. 102, pp. 33–55, 2013.

[17] M. Holroyd and J. Lawrence, "An analysis of using high-frequency sinusoidal illumination to measure the 3d shape of translucent objects," in *Proceedings of IEEE Conference on Computer Vision and Pattern Recognition (CVPR)*, 2011.

[18] T. Chen, H.-P. Seidel, and H. P. A. Lensch, "Modulated phase-shifting for 3D scanning," in *Proceedings of IEEE Conference on Computer Vision and Pattern Recognition (CVPR)*, 2008.

[19] T. Hawkins, P. Einarsson, and P. Debevec, "Acquisition of time-varying participating media," *ACM Transactions on Graph. (ToG)*, vol. 24, no. 3, pp. 812–815, 2005.

[20] J. Gu, S. K. Nayar, and E. Grinspun, "Compressive structured light for recovering inhomogeneous participating media," in *Proceedings of European Conference on Computer Vision (ECCV)*, 2008.

[21] C. Schlick, "A survey of shading and reflectance models," in *Computer Graphics Forum*, pp. 121–131, 1994.

[22] M. Kurt and D. Edwards, "A survey of brdf models for computer graphics," *SIGGRAPH Computer Graphics*, vol. 43, pp. 4:1–4:7, May 2009.

[23] A. Ghosh, S. Achutha, W. Heidrich, and M. OŤoole, "BRDF Acquisition with Basis Illumination," in *Proceedings of International Conference on Computer Vision (ICCV)*, 2007.

[24] Y. Mukaigawa, K. Sumino, and Y. Yagi, "Rapid BRDF Measurement using an Ellipsoidal Mirror and a Projector," *IPSJ Trans. on Computer Vision and Applications*, vol. 1, pp. 21–32, 2009.

[25] C. Donner, J. Lawrence, R. Ramamoorthi, T. Hachisuka, H. W. Jensen, and S. K. Nayar, "An Empirical BSSRDF Model," in *Proceedings of ACM SIGGRAPH*, 2009.

[26] H. W. Jensen, S. R. Marschner, M. Levoy, and P. Hanrahan, "A practical model for subsurface light transport," in *Proceedings of ACM SIGGRAPH*, 2001.

[27] B. K. P. Horn, "Shape from shading: A method for obtaining the shape of a smooth opaque object from one view," tech. rep., Massachusetts Institute of Technology, 1970.

[28] R. J. Woodham, "Photometric method for determining surface orientation from multiple images," *Optical Engineering*, vol. 19, no. 1, pp. 139–144, 1980.

[29] R. Zhang, P.-S. Tsai, J. E. Cryer, and M. Shah, "Shape-from-shading: a survey," *IEEE Transactions Pattern Analysis and Machine Intelligence (PAMI)*, vol. 21, no. 8, pp. 690–706, 1999.

[30] G. Healey and T. O. Binford, "Local shape from specularity," *Computer Vision, Graphics, and Image Processing*, vol. 42, pp. 62–86, 1987.

[31] S. Savarese, L. Fei-Fei, and P. Perona, "What do reflections tell us about the shape of a mirror?," in *Proceedings of the 1st Symposium on Applied perception in graphics and visualization*, pp. 115–118, ACM, 2004.

[32] Y. Adato, Y. Vasilyev, O. Ben-Shahar, and T. Zickler, "Toward a theory of shape from specular flow," in *Proceedings of International Conference on Computer Vision (ICCV)*, pp. 1–8, IEEE, 2007.

[33] A. C. Sankaranarayanan, A. Veeraraghavan, O. Tuzel, and A. Agrawal, "Specular surface reconstruction from sparse reflection correspondences," in *Proceedings of IEEE Conference on Computer Vision and Pattern Recognition (CVPR)*, 2010.

[34] M. F. Tappen, "Recovering shape from a single image of a mirrored surface from curvature constraints," in *Proceedings of IEEE Conference on Computer Vision and Pattern Recognition (CVPR)*, pp. 2545–2552, IEEE, 2011.

[35] K. N. Kutulakos and E. Steger, "A theory of refractive and specular 3d shape by light-path triangulation," in *Proceedings of International Conference on Computer Vision (ICCV)*, 2005.

[36] J. T. Kajiya and B. P. Von Herzen, "Ray tracing volume densities," in *Proceedings of ACM SIGGRAPH*, vol. 18, pp. 165–174, ACM, 1984.

[37] J. T. Kajiya, "The rendering equation," in *Proceedings of ACM SIGGRAPH*, vol. 20, pp. 143–150, ACM, 1986.

[38] M. Pauly, T. Kollig, and A. Keller, "Metropolis light transport for participating media," in *Proceedings of the Eurographics Workshop on Rendering Techniques*, (London, UK, UK), pp. 11–22, Springer-Verlag, 2000.

[39] Y. Mukaigawa, Y. Yagi, and R. Raskar, "Analysis of light transport in scattering media," in *Proceedings of IEEE Conference on Computer Vision and Pattern Recognition (CVPR)*, 2010.

[40] S. M. Seitz, Y. Matsushita, and K. N. Kutulakos, "A theory of inverse light transport," in *Proceedings of International Conference on Computer Vision (ICCV)*, vol. 2, pp. 1440–1447, IEEE, 2005.

[41] S. G. Narasimhan, M. Gupta, C. Donner, R. Ramamoorthi, S. K. Nayar, and H. W. Jensen, "Acquiring scattering properties of participating media by dilution," in *Proceedings of ACM SIGGRAPH*, pp. 1003–1012, 2006.

[42] L. Florescu, J. C. Schotland, and V. A. Markel, "Single-scattering optical tomography," *Physical Review E*, vol. 79, no. 3, p. 036607, 2009.

[43] Y. Mukaigawa, K. Suzuki, and Y. Yagi, "Analysis of subsurface scattering based on dipole approximation," *IPSJ Transactions on Computer Vision and Applications*, vol. 1, pp. 128–138, 2009.

[44] I. Gkioulekas, B. Xiao, S. Zhao, E. H. Adelson, T. Zickler, and K. Bala, "Understanding the role of phase function in translucent appearance," *ACM Transactions on Graph. (ToG)*, vol. 32, no. 5, p. 147, 2013.

[45] S. R. Arridge and J. C. Schotland, "Optical tomography: forward and inverse problems," *Inverse Problems*, vol. 25, no. 12, p. 123010, 2009.

[46] A. Velten, D. Wu, A. Jarabo, B. Masia, C. Barsi, C. Joshi, E. Lawson, M. Bawendi, D. Gutierrez, and R. Raskar, "Femto-photography: Capturing and visualizing the propagation of light," *ACM Transactions on Graph. (ToG)*, vol. 32, no. 4, p. 44, 2013.

[47] D. Wu, M. O 'Toole, A. Velten, A. Agrawal, and R. Raskar, "Decomposing global light transport using time of flight imaging," in *Proceedings of IEEE Conference on Computer Vision and Pattern Recognition (CVPR)*, 2013.

[48] D. Wu, G. Wetzstein, C. Barsi, T. Willwacher, Q. Dai, and R. Raskar, "Ultra-fast lensless computational imaging through 5d frequency analysis of time-resolved light transport," *International Journal of Computer Vision (IJCV)*, vol. 110, no. 2, pp. 128–140, 2014.

[49] S. A. Shafer and T. Kanade, "Using shadows in finding surface orientations," *Computer Vision, Graphics, and Image Processing*, vol. 22, no. 1, pp. 145–176, 1983.

[50] Y. Yu and J. T. Chang, "Shadow graphs and surface reconstruction," in *Proceedings of European Conference on Computer Vision (ECCV)*, 2002.

[51] S. Savarese, M. Andreetto, H. Rushmeier, F. Bernardini, and P. Perona, "3d reconstruction by shadow carving: Theory and practical evaluation," *International Journal of Computer Vision (IJCV)*, vol. 71, no. 3, pp. 305–336, 2007.

[52] S. K. Nayar, K. Ikeuchi, and T. Kanade, "Shape from interreflections," *International Journal of Computer Vision (IJCV)*, vol. 6, pp. 173–195, 1991.

[53] S. Liu, T.-T. Ng, and Y. Matsushita, "Shape from second-bounce of light transport," in *Proceedings of European Conference on Computer Vision (ECCV)*, 2010.

[54] T. Treibitz, Z. Murez, B. G. Mitchell, and D. Kriegman, "Shape from fluorescence," in *Proceedings of European Conference on Computer Vision (ECCV)*, 2012.

[55] Y. Kobayashi, T. Morimoto, I. Sato, Y. Mukaigawa, and K. Ikeuchi, "Reconstructing shape and appearance of thin film objects with hyper spectral sensor," in *Proceedings of Asian Conference on Computer Vision (ACCV)*, 2014.

[56] M. Liao, L. Wang, R. Yang, and M. Gong, "Light fall-off stereo," in *Proceedings of IEEE Conference on Computer Vision and Pattern Recognition (CVPR)*, 2007.

[57] C. P. Huynh, A. Robles-Kelly, and E. Hancock, "Shape and refractive index recovery from single-view polarisation images," in *Proceedings of IEEE Conference on Computer Vision and Pattern Recognition (CVPR)*, 2010.

[58] H. Murase, "Surface shape reconstruction of a nonrigid transport object using refraction and motion," *IEEE Transactions Pattern Analysis and Machine Intelligence (PAMI)*, vol. 14, pp. 1045–1052, Oct 1992.

[59] J. Ye, Y. Ji, F. Li, and J. Yu, "Angular domain reconstruction of dynamic 3d fluid surfaces," in *Proceedings of IEEE Conference on Computer Vision and Pattern Recognition (CVPR)*, 2012.

[60] A. Mohan, G. Woo, S. Hiura, Q. Smithwick, and R. Raskar, "Bokode: imperceptible visual tags for camera based interaction from a distance," *ACM Transactions on Graph. (ToG)*, vol. 28, no. 3, p. 98, 2009.

[61] Y. Ding, F. Li, Y. Ji, and J. Yu, "Dynamic fluid surface acquisition using a camera array," in *Proceedings of International Conference on Computer Vision (ICCV)*, 2011.

[62] M. Zhang, X. Lin, M. Gupta, J. Suo, and Q. Dai, "Recovering scene geometry under wavy fluid via distortion and defocus analysis," in *Proceedings of European Conference on Computer Vision (ECCV)*, 2014.

[63] I. Ihrke, K. N. Kutulakos, H. Lensch, M. Magnor, and W. Heidrich, "Transparent and specular object reconstruction," *Computer Graphics Forum*, vol. 29, no. 8, pp. 2400–2426, 2010.

[64] V. Chari and P. Sturm, "A theory of refractive photo-light-path triangulation," in *Proceedings of IEEE Conference on Computer Vision and Pattern Recognition (CVPR)*, 2013.

[65] G. Wetzstein, D. Roodnick, W. Heidrich, and R. Raskar, "Refractive shape from light field distortion," in *Proceedings of International Conference on Computer Vision (ICCV)*, 2011.

[66] D. Miyazaki and K. Ikeuchi, "Shape estimation of transparent objects by using inverse polarization raytracing," *IEEE Transactions Pattern Analysis and Machine Intelligence (PAMI)*, vol. 29, no. 11, pp. 2018–2030, 2007.

[67] M. B. Hullin, M. Fuchs, I. Ihrke, H. P. Seidel, and H. P. A. Lensch, "Fluorescent immersion range scanning," *ACM Transactions on Graph. (ToG)*, vol. 27, no. 3, p. article no.87, 2008.

[68] N. J. Morris and K. N. Kutulakos, "Reconstructing the surface of inhomogeneous transparent scenes by scatter trace photography," in *Proceedings of International Conference on Computer Vision (ICCV)*, 2007.

[69] B. Trifonov, D. Bradley, and W. .Heidrich, "Tomographic reconstruction of transparent objects," in *Proceedings of Eurographics Symposium on Rendering (EGSR)*, 2006.

[70] C. Ma, X. Lin, J. Suo, Q. Dai, and G. Wetzstein, "Transparent object reconstruction via coded transport of intensity," in *Proceedings of IEEE Conference on Computer Vision and Pattern Recognition (CVPR)*, pp. 3238–3245, June 2014.

[71] S. G. Narasimhan, S. K. Nayar, B. Sun, and S. J. Koppal, "Structured light in scattering media," in *Proceedings of International Conference on Computer Vision (ICCV)*, 2005.

[72] C. Tsiotsios, M. E. Angelopoulou, T.-K. Kim, and A. J. Davison, "Backscatter compensated photometric stereo with 3 sources," in *Proceedings of IEEE Conference on Computer Vision and Pattern Recognition (CVPR)*, 2014.

[73] T. Treibitz and Y. Y. Schechner, "Instant 3Descatter," in *Proceedings of IEEE Conference on Computer Vision and Pattern Recognition (CVPR)*, vol. II, pp. 1861–1868, 2006.

[74] B. Dong, K. D. Moore, W. Zhang, and P. Peers, "Scattering parameters and surface normals from homogeneous translucent materials using photometric stereo," in *Proceedings of IEEE Conference on Computer Vision and Pattern Recognition (CVPR)*, 2014.

[75] E. Hecht, *Optics*. Addison-Wesley, 2002.

[76] J. H. Lambert, *Photometria sive de mensure de gratibus luminis*. Eberhard Klett In Eberhard Klett, 1760.

[77] U. S. N. B. of Standards and F. E. Nicodemus, *Geometrical considerations and nomenclature for reflectance*, vol. 160. US Department of Commerce, National Bureau of Standards Washington, D. C, 1977.

[78] R. Montes and C. Ureña, "An overview of brdf models," *Technical Report LSI-2012-001 en Digibug Coleccion: TIC167 - articulos*, 2012.

[79] B. T. Phong, "Illumination for computer generated pictures," *Communications of the ACM*, vol. 18, pp. 311–317, June 1975.

[80] K. E. Torrance and E. M. Sparrow, "Theory for off-specular reflection from roughened surfaces," *Journal of the Optical Soceity of America (JOSA)*, vol. 57, no. 9, pp. 1105–1112, 1967.

[81] W. Matusik, H. Pfister, M. Brand, and L. McMillan, "Efficient isotropic brdf measurement," in *Proceedings of the 14th Eurographics workshop on Rendering*, pp. 241–247, 2003.

[82] P. Peers, T. Hawkins, and P. Debevec, "A reflective light stage," *ICT Technical Report ICT-TR-04*, 2006.

[83] M. Ben-Ezra, J. Wang, B. Wilburn, X. Li, and L. Ma, "An LED-only BRDF measurement device," in *Proceedings of IEEE Conference on Computer Vision and Pattern Recognition (CVPR)*, 2008.

[84] M. Aittala, T. Weyrich, and JaakkoLehtinen, "Practical svbrdf capture in the frequency domain," *ACM Transactions on Graph. (ToG)*, vol. 32, no. 4, p. 110, 2013.

[85] J. Filip, R. Vavra, M. Haindl, M. Krupika, and V. Havran, "Brdf slices: Accurate adaptive anisotropic appearance acquisition," in *Proceedings of IEEE Conference on Computer Vision and Pattern Recognition (CVPR)*, pp. 1468–1473, 2013.

[86] W. Matusik, H. Pfister, M. Brand, and L. McMillan, "A data-driven reflectance model," *ACM Transactions on Graph. (ToG)*, vol. 22, pp. 759–769, July 2003.

[87] K. Nishino, "Directional statistics brdf model," in *Proceedings of International Conference on Computer Vision (ICCV)*, 2009.

[88] A. Bilgili, A. ztrk, and M. Kurt, "A general brdf representation based on tensor decomposition," *Computer Graphics Forum*, vol. 30, no. 8, pp. 2427–2439, 2011.

[89] A. Ngan, F. Durand, and W. Matusik, "Experimental analysis of brdf models," in *Proceedings of the Sixteenth Eurographics conference on Rendering Techniques*, pp. 117–126, 2005.

[90] A. Levin, D. Glasner, Y. Xiong, F. Durand, W. Freeman, W. Matusik, and T. Zickler, "Fabricating brdfs at high spatial resolution using wave optics," *ACM Transactions on Graph. (ToG)*, vol. 32, no. 4, p. 144, 2013.

[91] M. B. Hullin, H. Lensch, R. Raskar, H.-P. Seidel, and I. Ihrke, "Dynamic display of brdfs," *Computer Graphics Forum*, vol. 30, no. 2, pp. 475–483, 2011.

[92] D. Glasner, T. Zickler, and A. Levin, "A reflectance display," *Proceedings of ACM SIGGRAPH*, 2014.

[93] T. Malzbender, R. Samadani, S. Scher, A. Crume, D. Dunn, and J. Davis, "Printing reflectance functions," *ACM Transactions on Graph. (ToG)*, vol. 31, no. 3, p. 20, 2012.

[94] S. Premovze, M. Ashikhmin, J. Tessendorf, R. Ramamoorthi, and S. K. Nayar, "Practical rendering of multiple scattering effects in participating media," in *Proceedings of the Fifteenth Eurographics conference on Rendering Techniques*, pp. 363–374, Eurographics Association, 2004.

[95] A. Munoz, J. I. Echevarria, F. J. Seron, J. Lopez-Moreno, M. Glencross, and D. Gutierrez, "Bssrdf estimation from single images," *Computer Graphics Forum*, vol. 30, no. 2, pp. 455–464, 2011.

[96] J. Stam, "Multiple scattering as a diffusion process," in *Rendering Techniques ' 95*, pp. 41–50, Springer, 1995.

[97] E. d'Eon and G. Irving, "A quantized-diffusion model for rendering translucent materials," *ACM Transactions on Graph. (ToG)*, vol. 30, no. 4, p. 56, 2011.

[98] N. Kurachi, *The Magic of Computer Graphics*. CRC Press, 2011.

[99] M. Levoy, B. Chen, V. Vaish, M. Horowitz, I. McDowall, and M. Bolas, "Synthetic Aperture Confocal Imaging," in *Proceedings of ACM SIGGRAPH*, pp. 825–834, 2004.

[100] S. Tagawa, Y. Mukaigawa, J. Kim, R. Raskar, Y. Matsushita, and Y. Yagi, "Hemispherical Confocal Imaging," *IPSJ Trans. on Computer Vision and Applications*, vol. 3, pp. 222–235, 2011.

[101] S. K. Nayar, X.-S. Fang, and T. Boult, "Separation of Reflection Components Using Color and Polarization," *International Journal of Computer Vision*, vol. 21, pp. 163–186, February 1997.

[102] K. Nishino, Z. Zhang, and K. Ikeuchi, "Determining Reflectance Parameters and Illumination Distribution from a Sparse Set of Images for View-dependent Image Synthesis," in *Proc. ICCV2001*, 2001.

[103] P. Peers, K. vom Berge, W. Matusik, R. Ramamoorthi, J. Lawrence, S. Rusinkiewicz, and P. Dutré, "A compact factored representation of heterogeneous subsurface scattering," *ACM Transactions on Graph. (ToG)*, vol. 25, pp. 746–753, July 2006.

[104] A. Beer, "Bestimmung der absorption des rothen lichts in farbigen flussigkeiten," *Annalen der Physik und Chemie*, vol. 86, pp. 78–88, 1852.

[105] L. G. Henyey and J. L. Greenstein, "Diffuse radiation in the galaxy," *Astrophysical Journal*, vol. 93, pp. 70–83, 1941.

[106] J. Kennedy and R. C. Eberhart, "Particle swarm optimization," in *IEEE International Conference on Neural Networks*, 1995.

[107] J. A. Nelder and R. Mead, "A simplex method for function minimization," *The Computer Journal*, vol. 7, pp. 308–313, 1965.

[108] Y. Mukaigawa, R. Raskar, and Y. Yagi, "Analysis of scattering light transport in translucent media," *IPSJ Transactions on Computer Vision and Applications*, vol. 3, pp. 122–133, 2011.

[109] S. Ikehata, D. Wipf, Y. Matsushita, and K. Aizawa, "Robust Photometric Stereo using Sparse Regression," in *Proceedings of IEEE Conference on Computer Vision and Pattern Recognition (CVPR)*, 2012.

[110] L. Wu, A. Ganesh, B. Shi, Y. Matsushita, Y. Wang, and Y. Ma, "Robust Photometric Stereo via Low-Rank Matrix Completion and Recovery," in *Proceedings of Asian Conference on Computer Vision (ACCV)*, 2010.

[111] K. D. Moore and P. Peers, "An empirical study on the effects of translucency on photometric stereo," *The Visual Computer*, vol. 29, no. 6-8, pp. 817–824, 2013.

[112] B. Dong, K. Moore, W. Zhang, and P. Peers, "Scattering Parameters and Surface Normals from Homogeneous Translucent Materials using Photometric Stereo," in *Proceedings of IEEE Conference on Computer Vision and Pattern Recognition (CVPR)*, 2014.

[113] A. Munoz, J. I. Echevarria, F. J. Seron, and D. Gutierrez, "Convolution-based simulation of homogeneous subsurface scattering," *Computer Graphics Forum*, vol. 30, no. 8, pp. 2279–2287, 2011.

[114] E. d'Eon and G. Irving, "A quantized-diffusion model for rendering translucent materials," *ACM Transactions on Graphics (TOG)*, vol. 30, 2011.

[115] T. H. Kim, B. Ahn, and K. M. Lee, "Dynamic scene deblurring," in *Proceedings of International Conference on Computer Vision (ICCV)*, pp. 3160–3167, IEEE, 2013.

[116] T. H. Kim and K. M. Lee, "Segmentation-free dynamic scene deblurring," in *Proceedings of IEEE Conference on Computer Vision and Pattern Recognition (CVPR)*, pp. 2766–2773, 2014.

[117] N. Wiener, *Extrapolation, Interpolation, and Smoothing of Stationary Time Series:With Engineering Applications*. MIT Press, 1 ed., 1949.

[118] W. H. Richardson, "Bayesian-based iterative method of image restoration," *Journal of the Optical Soceity of America (JOSA)*, vol. 62, pp. 55–59, 1972.

[119] S. Cho, J. Wang, and S. Lee, "Handling outliers in non-blind image deconvolution," in *Proceedings of International Conference on Computer Vision (ICCV)*, 2011.

[120] W. Dong, L. Zhang, and G. Shi, "Centralized sparse representation for image restoration," in *Proceedings of International Conference on Computer Vision (ICCV)*, 2011.

[121] A. Levin, Y. Weiss, F. Durand, and W. T. Freeman, "Efficient marginal likelihood optimization in blind deconvolution," in *Proceedings of IEEE Conference on Computer Vision and Pattern Recognition (CVPR)*, 2011.

[122] D. Krishnan, T. Tay, and R. Fergus, "Blind deconvolution using a normalized sparsity measure," in *Proceedings of IEEE Conference on Computer Vision and Pattern Recognition (CVPR)*, 2011.

[123] J. Gu, T. Kobayashi, M. Gupta, and S. K. Nayar, "Multiplexed illumination for scene recovery in the presence of global illumination," in *Proceedings of International Conference on Computer Vision (ICCV)*, 2011.

[124] A. Agrawal, R. Raskar, and R. Chellappa, "What is the range of surface reconstructions from a gradient field?," in *Proceedings of European Conference on Computer Vision (ECCV)*, 2006.

[125] "Lytro." `https://www.lytro.com/`.

[126] A. Velten, D. Wu, A. Jarabo, B. Masia, C. Barsi, C. Joshi, E. Lawson, M. Bawendi, D. Gutierrez, and R. Raskar, "Femto-photography: Capturing and visualizing the propagation of light," *ACM Transactions on Graph. (ToG)*, vol. 32, pp. 44:1–44:8, July 2013.

[127] L. Gao, J. Liang, C. Li, and L. V. Wang, "Single-shot compressed ultrafast photography at one hundred billion frames per second," *Nature*, vol. 16, no. 7529, pp. 74 – 77, 2014.